Metamaterial Optics for Precision Cosmic Microwave Background Observation

by

Kevin P. Coughlin

A dissertation submitted in partial fulfillment
of the requirements for the degree of
Doctor of Philosophy
(Physics)
in the University of Michigan
2018

Doctoral Committee:

Associate Professor Jeffery McMahon, Chair
Professor Katherine Freese
Professor Dragan Huterer
Associate Professor Chris Miller
Professor Gregory Tarle

Kevin Patrick Coughlin

kpcoughl@umich.edu

ORCID iD: 0000-0002-3283-5403

Dedication

For Kayla

Acknowledgements

I would like to acknowledge lots of things.

I would like to thank my advisor Jeff McMahon. He helped guide me through my research and schooling, providing help and encouragement as needed.

I would also like to thank the rest of my dissertation committee, Professors Greg Tarle, Dragan Huterer, Chris Miller and Katherine Freese, for their help and suggestions for my dissertation.

I want to thank the rest of the members of the McMahon Lab: Charles Munson and Rahul Datta, previous graduate students who helped get me up to speed with the technology development of the lab; Fletcher Boone, a technician whose help with fabrication allowed me to focus on other problems; Taylor Baildon, Joey Golec, Grace Chesmore, and Carlos Sierra, the current graduate students in whose competent hands I leave the work yet to be done; and Dr. Sara Simon, our postdoc who helped whenever I needed it, whether for presentations or technical problems.

I want to thank NASA for the support (financial and technical) over the last several years, specifically Dr. Edward Wollack and Prof. Dave Chuss, whose microwave expertise contributed significantly to my work.

I want to thank the ACT Collaboration for their support and work, especially Jon Ward and Matthew Hasselfield, whose work on the rotation system for the HWP was necessary for my work to matter.

I would also like to thank the many people in my life whose love and support have gotten me this far, especially my father Peter and my wife Kayla.

Preface

Over the last five years, I have been part of the ACTPol and Advanced ACT collaborations. The objective of these collaborations is to build sensitive instruments for observations of the Cosmic Microwave Background, and deploy them on the Atacama Cosmology Telescope. The science goals including refinements of ΛCDM cosmology, cataloging galaxy clusters, and detecting primordial gravitational waves. These represent many of the most pressing questions of Cosmology.

The majority of my work has been the development and production of the optical elements needed to enable these measurements. This includes antireflection coating on lenses, which have led to the measurement the CMB power spectrum, lensing spectrum, and SZ effects, and development of half-wave plates that could revolutionize measurements of large angular scale polarization and the gravitational wave signature of inflation.

These coatings, made of metamaterial silicon, are the best in the field. They reduce reflection to well under a percent, have negligible loss, can cover large lenses (over 30 cm), are robust to thermal cycling, and are tunable to a very large range of frequencies (20 GHz to 2 THz). My work on them will continue having an impact on the field into the next decade.

While the use of half-wave plates is not new to the field, my work is a significant departure from the norm. As opposed to settling for found material, I used my experience from the coatings to create something new: a metamaterial half-wave plate. The tunability of this optical component has opened up new regions of parameter space to be explored, enabling broad bandwidth, low emission half-wave plates to be implemented on ACT.

The half-wave plates significantly reduce the effect of $1/f$ noise in our system. This noise dominates over the CMB signal at angular scales larger than approximately half a degree. Unfortunately, the gravitational wave signal lives around the two degree angular scale. With the half-wave plates deployed, we hope to be able to make a detection of this signal. The significance of this detection would be massive. Not only would it provide further evidence of inflation, but it would be the first quantum gravity effect detected. As of writing this, no detection of gravitational waves has been made, but the analysis of the data is on going.

Table of Contents

List of Figures

List of Appendices

Abstract

The Cosmic Microwave Background (CMB) is the oldest light in the Universe. As such it provides deep insight into both early and late Universe physics, including the sum of the neutrino masses and possible signatures of inflation. To better characterize the temperature and polarization anisotropies of the CMB, new instruments need to be designed.

The Atacama Cosmology Telescope (ACT) is a six meter telescope built to observe the CMB. This thesis describes contributions to new broadband receivers called ACTPol and Advanced ACTPol. The receiver has three independent cameras with feedhorn coupled, polarization sensitive superconducting bolometer detectors. The first two detector arrays for ACTPol are sensitive to 150 GHz. The other detector arrays are dichroic, sensitive to two frequency bands: the low frequency (20/40 GHz), mid frequency (90/150 GHz), and high frequency (150/220 GHz). I have further developed the three layer metamaterial antireflection (AR) coating technology used to realize the necessary bandwidth for the current dichroic detectors for the ACTPol and Advanced ACTPol instruments. In this thesis I describe work to push the boundaries of that technology beyond the current needs, and develop broader bandwidth, five layer AR coatings which could effectively cover 50-350 GHz, and higher frequency coatings which could work up to 2 THz.

I also applied the metamaterial design and fabrication techniques to a different optical element for CMB observation: half-wave plates (HWPs). I began with a simple single frequency HWP for the ACTPol instrument, then went to a broadband, three stack HWP for the ACTPol and Advanced ACTPol dichroic bands. These HWPs represent a novel use of metamaterial technology, with significant benefits over traditional found material HWPs.

With these optical elements, the ACT collaboration has published a number of scientific papers. We have reported new measurements of the temperature and polarization power spectra of the CMB. We have used the Sunayev-Zeldovich effect to measure the masses of galaxy clusters. We have detected the effects of gravitational lensing on the CMB, and compared this lensing mass profile to optical lensing measurements.

This thesis is organized as follows. Chapter 1 gives an overview of Cosmology, including its history and current goals. Chapter 2 is a detailed description of the Atacama Cosmology

Telescope and its various instrumentation. In Chapter 3 I discuss my work on the antireflection coatings. Chapter 4 is about my work on half-wave plates. Chapter 5 concludes with a discussion of the science my work has enabled and the future of the work presented in this thesis and CMB observations in general.

Chapter 1

Cosmology Overview

1.1 Introduction

Cosmology is the study of the Universe as a whole; its origin, history, components, and, ultimately, fate. Humans have been theorizing about the nature of the Universe since time immemorial, but cosmology in the scientific sense is a relatively new field. At the start of the start of the 20th century, leaps in theoretical physics and observational astronomy lead us to the Big Bang model, completely changing the way we understood the Universe. More recent developments (Inflation, Dark Matter and Dark Energy) have lead to the current standard model of cosmology, ΛCDM. Current and future experiments aim to test and refine this theory. In this chapter I present this history and outstanding questions in cosmology.

1.2 Towards the Big Bang

The development of the Theory of General Relativity by Einstein in 1916 [14] brought our understanding of gravity to its current state. In 1922, Alexander Friedmann applied this theory to a homogeneous, isotropic universe and derived the Friedmann Equations for an expanding universe [15]. Georges Lematre first proposed that this expanding universe started with a Big Bang [16], in contrast to most others at the time that believed in a steady state universe [17]. In the decades following the proposal of this Big Bang Cosmology, a preponderance of supporting evidence would accumulate.

At the turn of the century, astronomers were still mapping our own galaxy. Parallax measurements were the first made in the mid 19th century [18], giving us the first step along the distance ladder. In 1908, Henrietta Swan Leavitt showed that the the pulsation rate of Cepheid variable stars was correlated with their absolute luminosity [19]. Thus, measuring

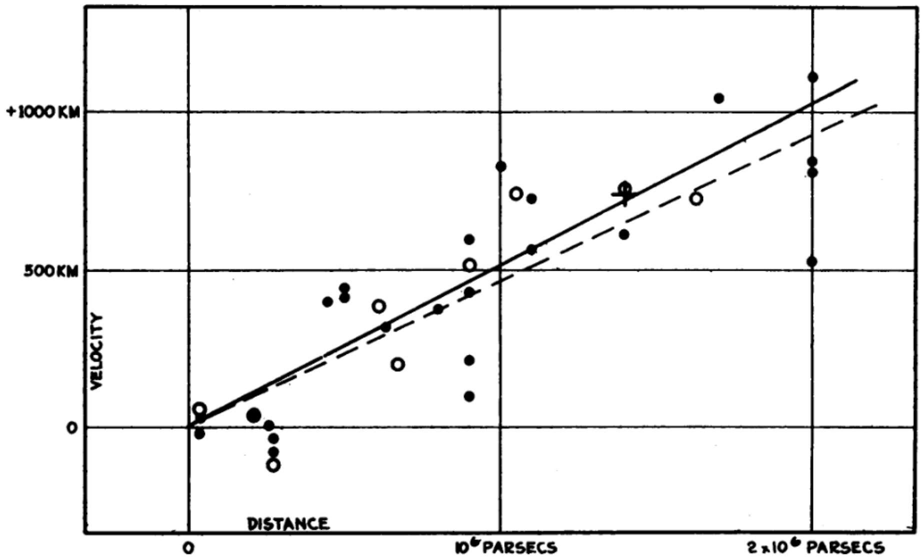

Figure 1.1: Hubble's original plot of the relation between recessional velocity and distance (measured by cepheid variables) of other galaxies. Plot taken from [1]

the apparent luminosity and the pulsation rate, one can establish the distance to a star, adding a second rung on the distance ladder. This allowed astronomers to measure distances far beyond that which parallax could reach.

Edwin Hubble first used this method to measure stars in several "nebulae" [1,20], which turned out to have distances much greater than the established size of the Milky Way. These nebulae Hubble measured were, to state what is now obvious, other galaxies. Using redshift data provided by Vesto Slipher [21], Hubble then showed that the farther away the galaxies were, the faster they were receding. His original plot is shown in Figure 1.1. This so-called Hubble Flow seemed to point very directly to a Big Bang, but the skeptics were not yet satisfied.

In the 1948, Alpher, Bethe and Gamow published the seminal paper on Big Bang Nucleosynthesis [22], arguing that if the Big Bang occurred, then that could explain the relative abundance of light elements in the Universe. This theory, though not perfect, did match the existing measurements of hydrogen and helium isotopes in the Universe, further tipping the scales toward the Big Bang. Figure 1.2 shows the nuclear fusion paths for the light elements, as well as a plot of their relative abundances.

The third pillar of experimental evidence leading to the acceptance of the Big Bang model was the serendipitous discovery of the Cosmic Microwave Background (CMB), the afterglow of the Big Bang, discussed in detail in Section 1.3. Over time, the CMB has proven to be one of the best sources of cosmological evidence, shedding light on the origin, history, and

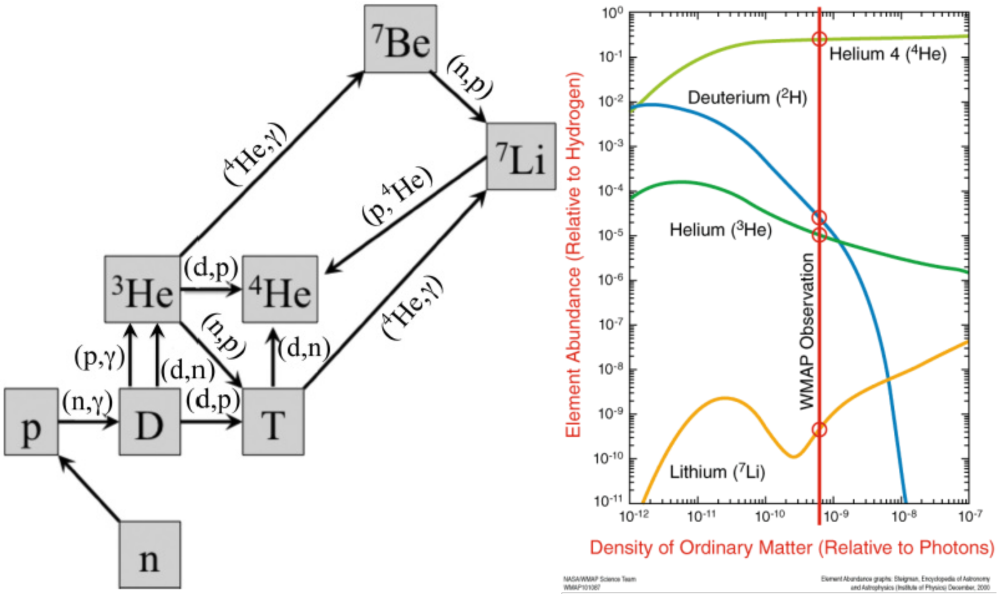

Figure 1.2: (Left) Diagram of nuclear processes occurring during Big Bang Nucleosythesis. (Right) Relative abundances of light elements formed during BBN plotted against relative density of baryonic matter vs photons. As can be seen, all of the elements observed are consistent with a particular matter-to-photon density, further constraining our knowledge of the early Universe. The plot was taken from NASA WMAP Science Team.

geometry of the Universe. The CMB is still a very active field and is the subject of this thesis.

1.3 The Cosmic Microwave Background

1.3.1 Origin and Discovery

The CMB is the leftover afterglow of the Big Bang. It was emitted when the Universe was only 380,000 years old. Before that time, the Universe was filled with a hot, dense plasma which was tightly coupled to radiation. As the Universe expanded and cooled, the plasma recombined into gas, and the mean free path of photons grew to the size of the Universe. Since this surface of last scattering, the CMB photons have been free streaming largely unperturbed.

The CMB was first conjectured to exist in 1948 by Alpher and Herman [23] as a consequence of the Big Bang. It was discovered by Penzias and Wilson in 1964. While using a horn antenna for satellite communication work, they found a noise source they couldn't eliminate from their system. After discussing the problem with a colleague, they were put in contact with Robert Dicke at Princeton, who had been working on developing an experiment to measure the signal. This was the final nail in the coffin for the steady state model, which had no mechanism for producing this radiation. Penzias and Wilson won the Nobel Prize in 1974 for their discovery.

1.3.2 Uniformity and Inflation

The CMB is uniform in temperature across the sky to one part in 10^5. This means that photons from opposite sides of the Universe are in thermal equilibrium despite not being in causal contact. This so-called Horizon Problem was solved with the introduction of the theory of inflation, by Alan Guth in 1980 [24]. The theory of inflation postulated that a class of scalar fields could drive exponential expansion of the Universe. This was originally proposed as a solution to the magnetic monopole problem, saying if there was monopole production in the early Universe, the particles would have been diluted down to immeasurably low number density. This exponential growth in the early universe also solved the horizon problem, allowing thermal contact between super horizon modes before inflation, then expanding them out of contact.

Additionally, inflation solved the flatness problem of the universe. The geometry of the universe is measured to be flat within a tight experimental error. We don't have a known reason for the Universe to be perfectly flat, and any deviation from flatness rapidly increases as the Universe expands. With inflation, the Universe gets driven to so close to flat that the curvature of the current Universe will be immeasurably small.

Most theories of inflation predict that the process of exponential growth in the Universe would cause primordial gravitational waves (PGW) to form (for example [25,26]. While most theories predict some level of these perturbations, they do vary as to what their amplitude would be. These PGW would leave a signature on the CMB polarization. As of writing this thesis, no such signal has been detected. A true detection of this signal could shed light on the details of inflation.

1.3.3 Temperature Spectrum

The CMB was predicted to have a near-perfect blackbody spectrum [23]. In 1990, the FIRAS instrument on board the COBE satellite mission preliminarily measured the CMB to be consistent with a perfect blackbody, with a temperature of 2.735 ± 0.06 K [27]. Further analysis of this data drastically increased the precision [2]. The measured spectrum from [2] is shown in Figure 1.3. This measurement proved so precise that, to date, no new experiment has outdone FIRAS.

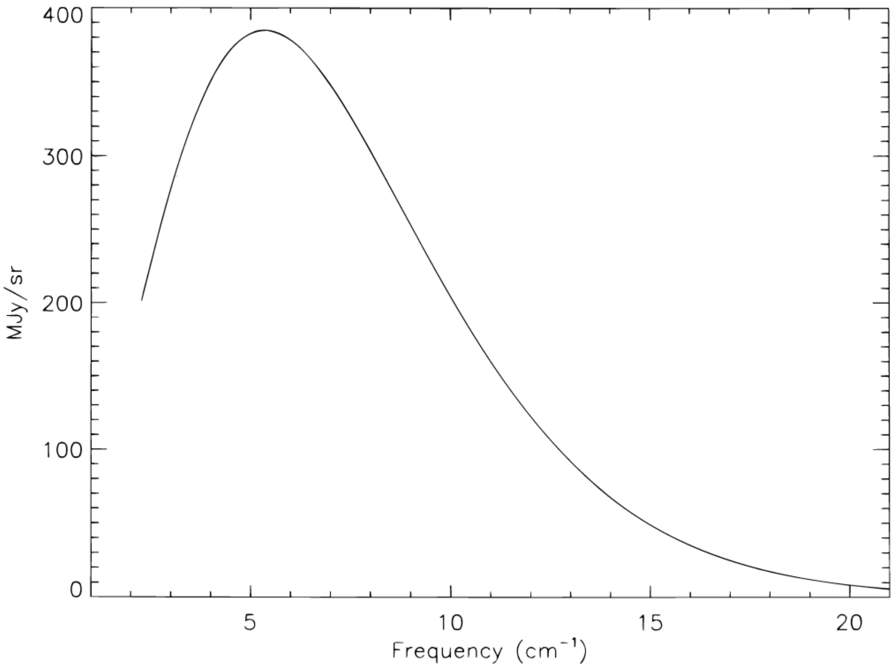

Figure 1.3: Temperature spectrum of the CMB. The error bars are not show as the error of the measurement is significantly smaller than the thickness of the line. The data is excellently matched to a blackbody radiation spectrum at 2.728 ± 0.004 K. Plot taken from [2]

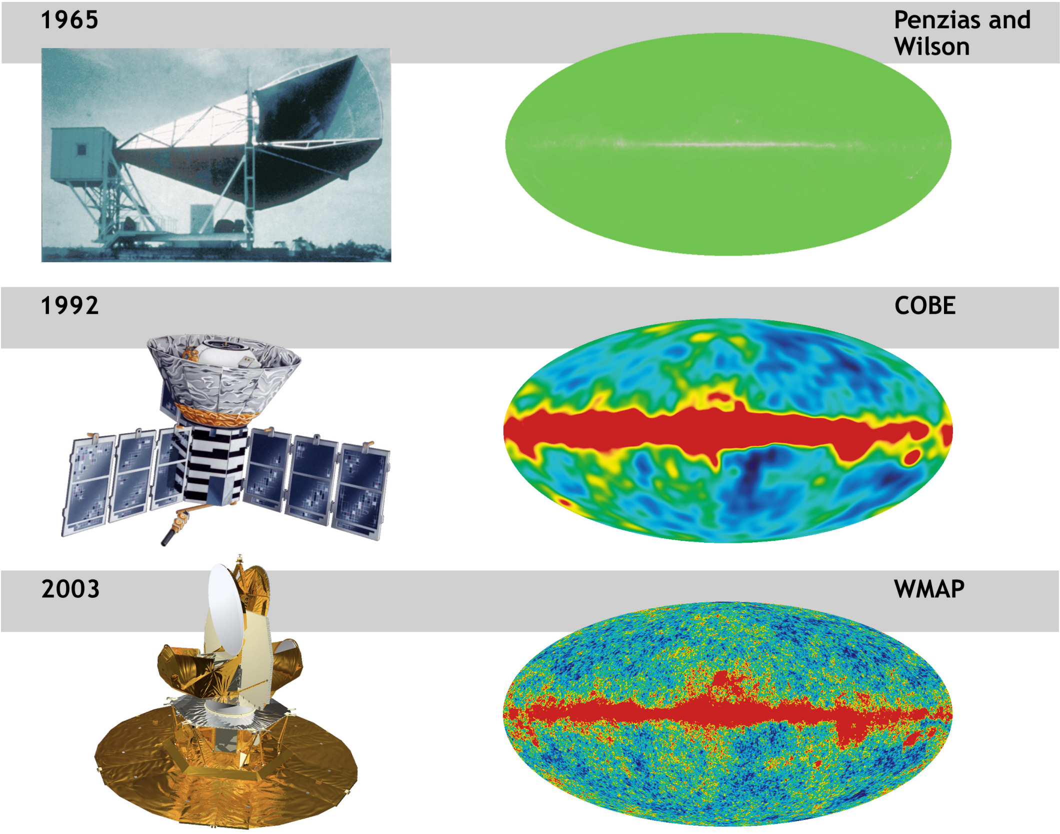

Figure 1.4: Three iteration of all sky CMB maps from the first measurement of Penzias and Wilson through to the map made by the WMAP experiment. As time has progressed, our sensitivity to small angular scales has grown.

1.3.4 Temperature Anisotropies

While the CMB is largely uniform, there are small temperature differences in different patches of the sky. The temperature anisotropies are on the order of tens of μK. These fluctuations amount to a scalar field on the surface of a sphere, and thus can be decomposed into spherical harmonics.

$$\frac{\delta T(\theta\phi)}{T} = \sum_{\ell,m} a_{\ell m} Y_{\ell m}(\theta,\phi), \tag{1.1}$$

From the $a_{\ell m}$ values, one constructs an angular power spectrum

$$C_\ell = \frac{1}{2\ell+1}\sum_{m=-\ell}^{\ell} |a_{\ell m}|^2. \tag{1.2}$$

This measured angular power spectrum is used to compare to theoretical predictions from

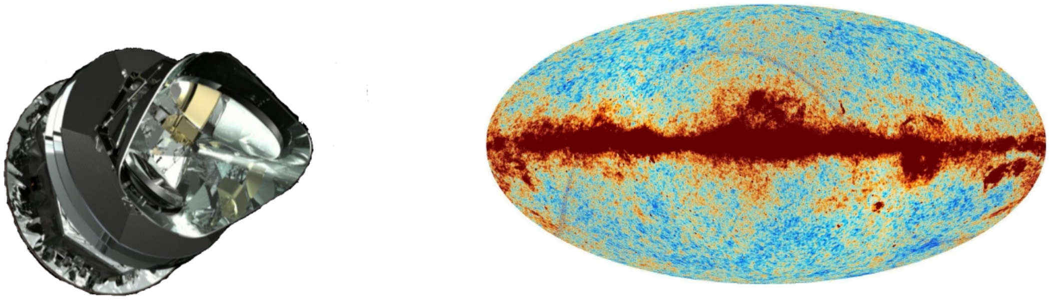

Figure 1.5: The Planck Satellite and the all sky map of the CMB.

the standard model of cosmology. Figures 1.4 and 1.5 show all sky maps of the CMB and the instruments they were measured with. Recent angular power spectrum measurements by the Planck mission are shown in Figure 1.6.

The causes of these temperature anisotropies fall into two categories: primary and secondary. Primary anisotropies come from before the decoupling of photons and the primordial plasma. In effect these are a snapshot of how the Universe looked at surface of last scattering. The overdensities are seen as cold spots, underdensities as hot spots. These density fluctuations were seeded by quantum fluctuations, blown up to macroscopic scales by inflation.

Between inflation and recombination, the fluctuations interacted with the primordial plasma. Gravity led to further collapse the overdensities while photon pressure worked to homogenize the plasma. The conflict between these two factors created acoustic oscillations in the primordial plasma. These sound waves traveled a characteristic distance before recombination based on the composition of the primordial plasma. The location of the peaks in the CMB power spectrum show the length scale of these sound waves.

Secondary anisotropies in the CMB come from physics after the nominal surface of last scattering. As the photons pass by massive galaxies and galaxy clusters, a number of effects can change their energy and path. Large scale structure can gravitationally deflect the CMB along the projected gravitational gradient. The hot gas of the intercluster medium causes scattering. Evolving gravitational potentials can cause net energy shifts. All of these effects are relatively small in comparison to the primary anisotropies. Looking for these signals can give information about the structure of the more recent Universe.

These temperature anisotropies were first measured by the DMR instrument on board the COBE satellite, published in 1992. They found a temperature rms of $30 \pm 5 \mu$K variations at 10° beam size [28].

The first peak in the power spectrum was first measured in its entirety by the MAT/Toco experiment [29] in 1999, followed shortly by the BOOMERanG [30] and MAXIMA [31]

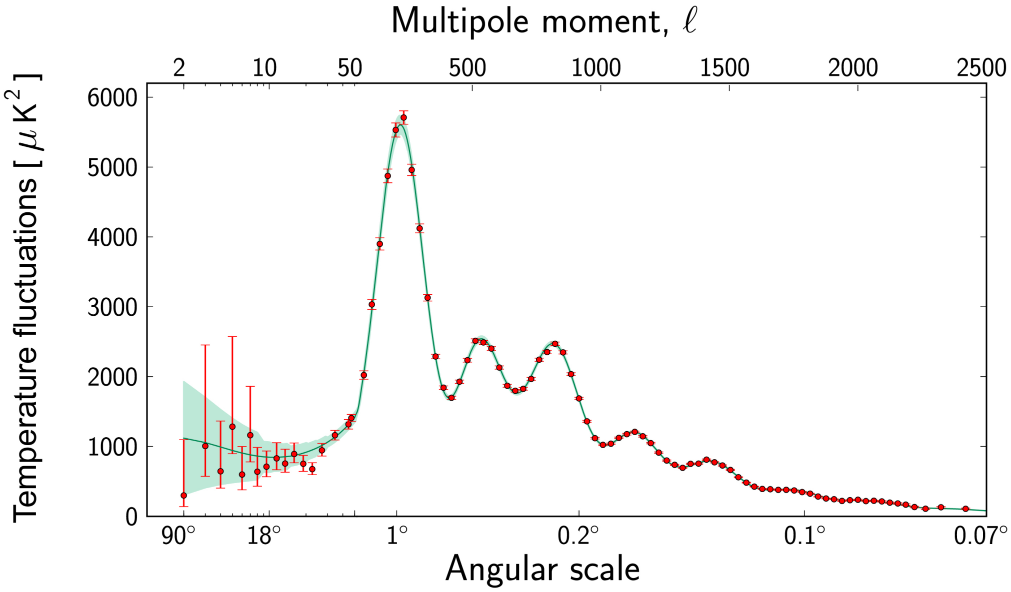

Figure 1.6: Temperature anisotropy power spectrum as measured by the Planck satellite mission.

experiments in 2000. They determined the first peak in the angular power spectrum was located at $\ell = 197 \pm 6$. This matched the predicted location based on theoretical work on primary anisotropies. BOOMERanG found $0.88 < \Omega_{m+\Lambda} < 1.12$ at 95% confidence, strongly supporting a flat universe within the ΛCDM cosmological paradigm.

After BOOMERanG and MAXIMA, more experiments continued the work, mapping the CMB to increasingly fine resolution. WMAP, a satalite launched in 2001, took data for nine years, measuring out to $\ell \approx 1200$, cleanly resolving the first three peaks in the power spectrum [32]. Large ground-based telescopes (ACT [33],SPT [34]) have measured out to $\ell \approx 5000$ for patches of the sky, detecting the damping tail. The Planck satellite measured the whole sky down out to $\ell \approx 2500$ [35], significantly tightening constraints on cosmological parameters [36].

Currently, the precision of observations of the temperature power spectrum are approaching the cosmic variance limit (sample variance is proportional to number of modes) at increasingly small angular scales. Once the cosmic variance limit is hit, there will be no more information for this power spectrum to give, although that doesn't mean CMB science is done.

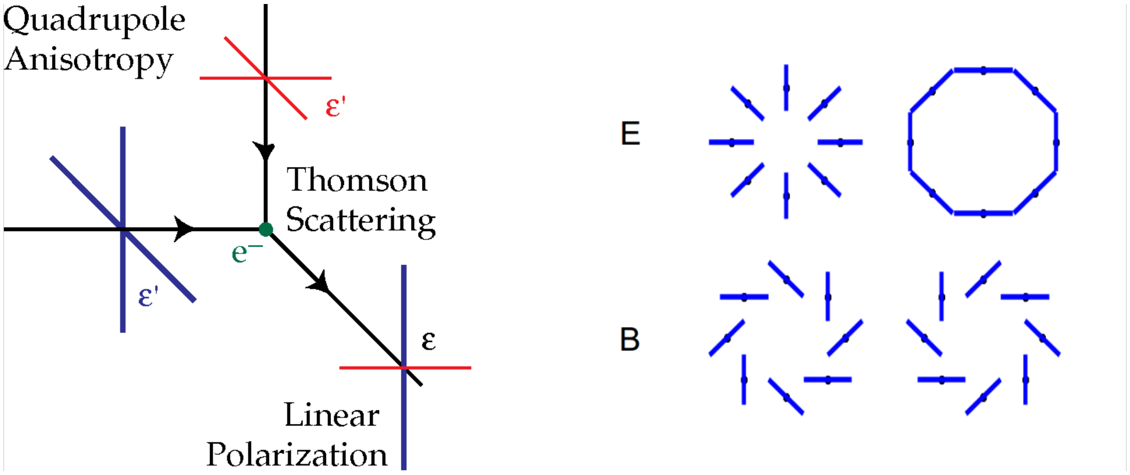

Figure 1.7: (Left) Schematic diagram of how a quadrupole temperature pattern causes polarization via Thompson Scattering. Figure from [3]. (Right) Pure E- and B- mode polarization patterns. E-modes have an even parity (i.e. they are symmetric under reflection). B-modes have odd parity (i.e. they are antisymmetric under reflection).

1.3.5 Polarization

The CMB is weakly polarized at the μK scale. The polarization is created by quadrupole temperature anisotropies scattering off electrons (Thompson scattering). This polarization occurs at the surface of last scattering and during reionization. Prior to recombination, the mean free path of photons was short, meaning that they would be rescattered repeatedly until they were effectively homogenized. Only as recombination is proceeding does scattering impart a net polarization to the photons. During the epoch of reionization, the free electrons can once again impart a net polarization to the CMB at angular scales near the size of the horizon at the time [37].

In Thompson scattering, when a photon hits an electron, the electron will oscillate with the electric field of the photon. This causes the electron to act as a dipole antenna, oscillating at the same frequency as the incident photon. The radiation produced by the electron is of the same frequency as the incident radiation, and polarized in the $\hat{\theta}$ orientation (assuming the electron is oscillating in the $\hat{z}$ direction). With a quadrupole temperature anisotropy, this causes the scattered radiation to have a net polarization. This is shown schematically in Figure 1.7.

While quadrupoles are the only cause of polarization at any point on the sky, there are various sources of the quadrupole which cause distinct patterns across the sky. These patterns can be decomposed in a way similar to that of temperature into two mathematically (and physically) convenient basis vectors, E-modes and B-modes [38, 39]. The nomenclature is

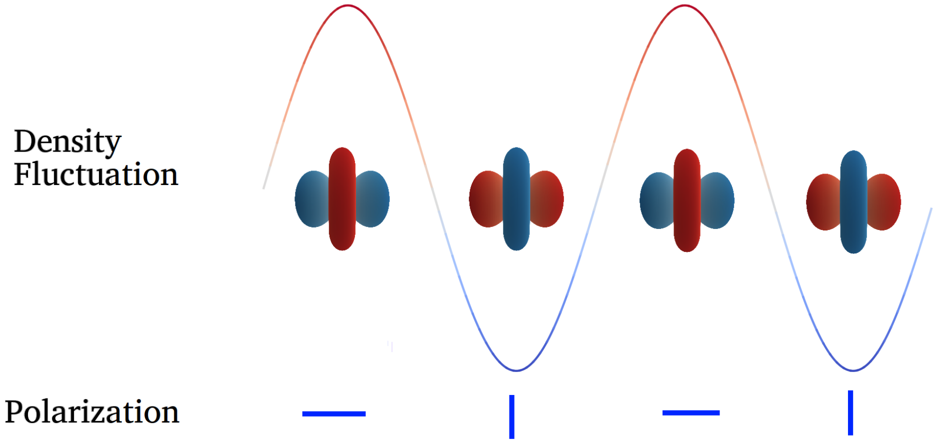

Figure 1.8: Scalar energy density fluctuations cause azimuthally symmetric quadrupole. The projection of these quadrupole onto the celestial sphere always cause E-mode polarization.Figure inspired by [3].

taken from electrostatics, where electric (E) fields have no curl, and magnetic (B) fields have no divergence. They are mathematically convenient as they form a complete, orthogonal basis set, with E-modes having even pairity, and B-modes having odd-parity. They are physically convenient as they have different physical sources. The canonical E- and B-modes are shown in Figure 1.7.

The difference in parity of the modes comes from the symmetry of the quadrupole that form them, i.e. whether the local quadrupole has scalar ($m = 0$), vector ($m = 1$), or tensor ($m = 2$) symmetry.

Scalar modes are caused by energy density fluctuations. The quadrupole created by these fluctuations are oriented along the mode propagation vector, giving them azimuthal symmetry (effectively the $m = 0$, $\ell = 2$ spherical harmonic.) This symmetry is what keeps them from forming B-modes. This is depicted in Figure 1.8

Vector modes can be caused by voricies in the primordial plasma. Circulating ions impart an asymmetric Doppler shift to scattered photons, causing an apparent quadrupole. This effect is predicted to be very small since these modes are rapidly damped, and thus can be ignored.

Tensor modes are caused by propagating primordial gravitational waves (PGWs). As these wave move through the plasma, they create quadrupoles by compressing and rarefying space. These quadrupoles are oriented normal to the propagation vector, so there is no azimuthal symmetry to the quadrupoles. Depending on the polarization of the PGW and the projection of the quadrupoles onto the surface of last scattering, this can impart either E-modes or B-modes. This is shown in Figure 1.9. In inflatoinary models, these PGWs are sourced from fluctuatoins in the metric tensor, blow up to large scales by inflation. There has also been some theoretical work done recently suggesting rolling spectator axions would also create tensor modes in the early Universe [40].

While PGWs are the only source of B-modes at the surface of last scattering, there is an additional source of B-modes in the late Universe. Gravitational lensing by galaxy clusters can leak E-mode signal into the B-mode channel. Fortunately, it is possible to distinguish the signals. The lensing B-modes peak at an angular scale around 0.2° on the sky. The PGW signal peaks around 2°. The axion signal If there is an excess in the power spectrum at those large angular scales, that would be a firm detection of PGW. This is shown in Figure 1.10

The strength of these PGWs is not known *a priori*. It is an input parameter in the standard model of cosmology, ΛCDM, parameterized as the ratio of the tensor and scalar perturbation strengths, labeled as r. While ΛCDM does not calculate or assume any value for r, different theories of inflation predict different values for this ratio. Therefore a detection, or even a stronger upper limit, will aid our understanding of Inflation physics, leading to a better understanding of our Universe and provide a fundamental test for inflation.

With the temperature map and the two polarization maps, there are six power spectra that can be computed. The EE, TE, and BB spectra are shown in Figure 1.10. The TB and EB spectra are not show, as they are expected to be zero due to the opposite parity of the B modes from the temperature and E-modes. There are, however, some late Universe effects that can generate non-zero correlation between the B-mode maps and the other two [41]. Measurement of these power spectra can thus be a useful probe of gravitational lensing and Dark energy.

1.3.6 Foregrounds

One major issue around CMB observation is the presence of foreground contamination for both temperature and polarization measurements. Figure 1.11 shows the emission spectra of various sources of these foregrounds. Polarized dust emission dominates at higher frequency, and synchrotron radiation dominates at lower frequency. In order to properly handle these foregrounds, it is important that CMB observations are made in multiple bands. Doing this allows the total signal spectrum to be measured, which can in effect be fit as the sum of the foregrounds and the CMB.

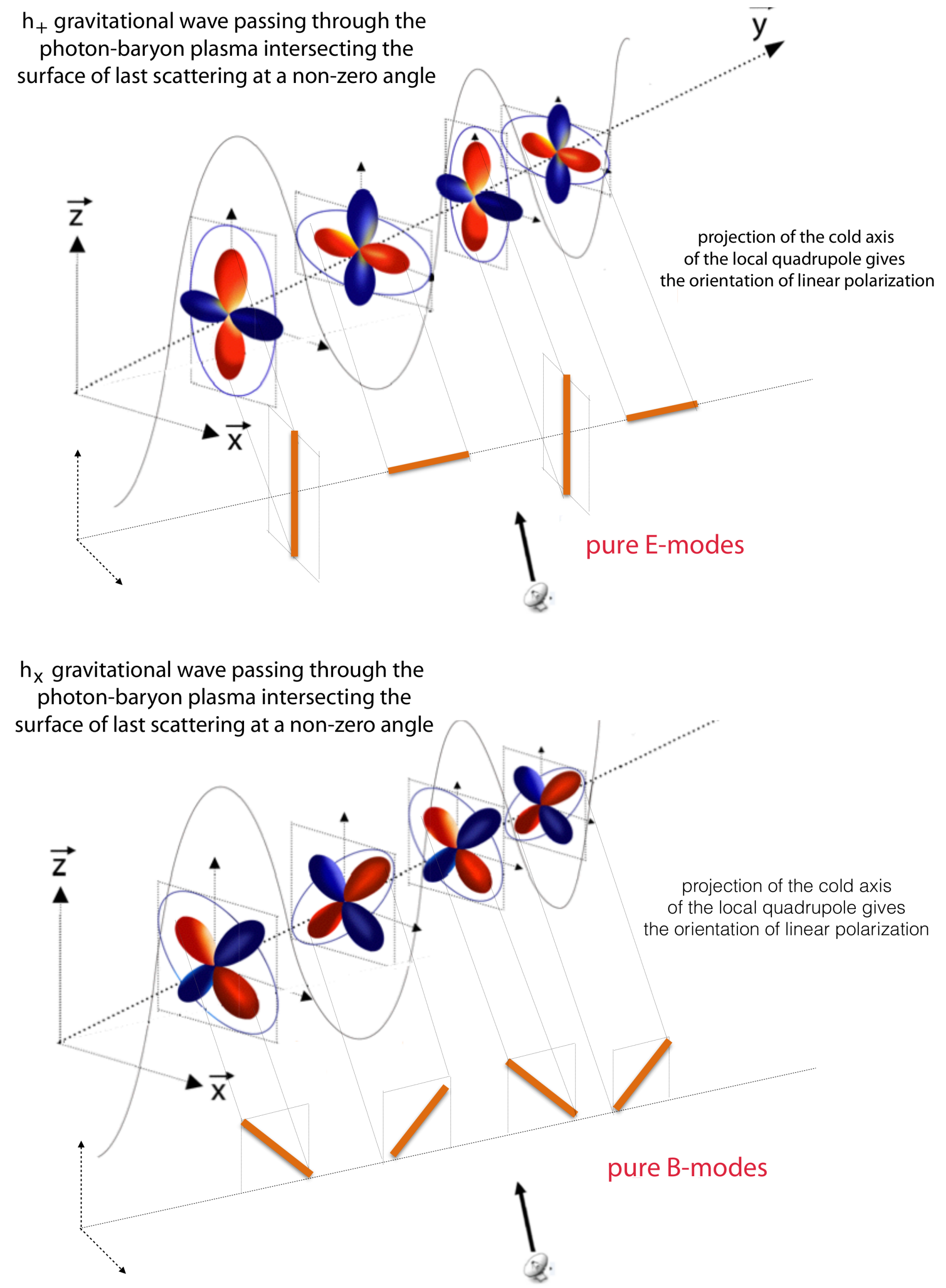

Figure 1.9: Gravitational waves propagating through the primordial plasma create both E- and B- modes. Whether it shows up as an E-mode, B-mode, or doesn't show up has to do with what the polarization of the wave is, and how is gets projected onto a sphere. If the wave was traveling along the surface of the celestial sphere, all of the temperature quadrupoles would be normal to the sky, and thus would not cause any polarization to reach us. This Figure was taken from [4]

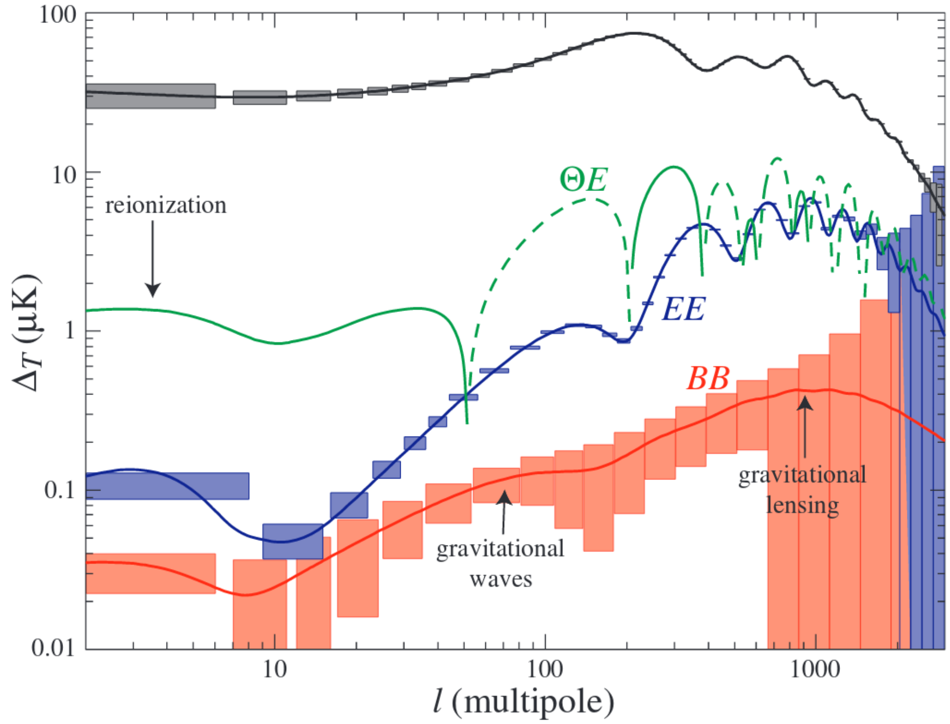

Figure 1.10: Auto spectra of temperature, E- and B-modes, and cross spectrum of TE. The PGW signal in the BB spectrum peaks at $\ell < 100$, while the lensing BB signal peaks around $\ell \approx 1000$. The different shapes of these contributions should allow the detection of the PGW signal. The Figure is adapted from [5]

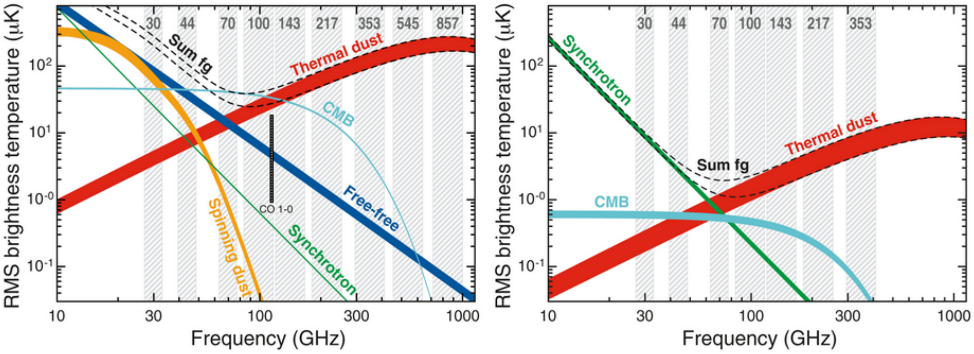

Figure 1.11: Temperature (right) and polarization (left) foreground and CMB spectra. These foregrounds have their own unique spectrum, so by measuring the total signal in several frequency bands, we can separate out the foreground from the CMB. Low frequency measurements are used to isolate the synchrotron foreground, and higher frequency bands are used to isolate the thermal dust emission. Plots are taken from the Planck Collaboration [6].

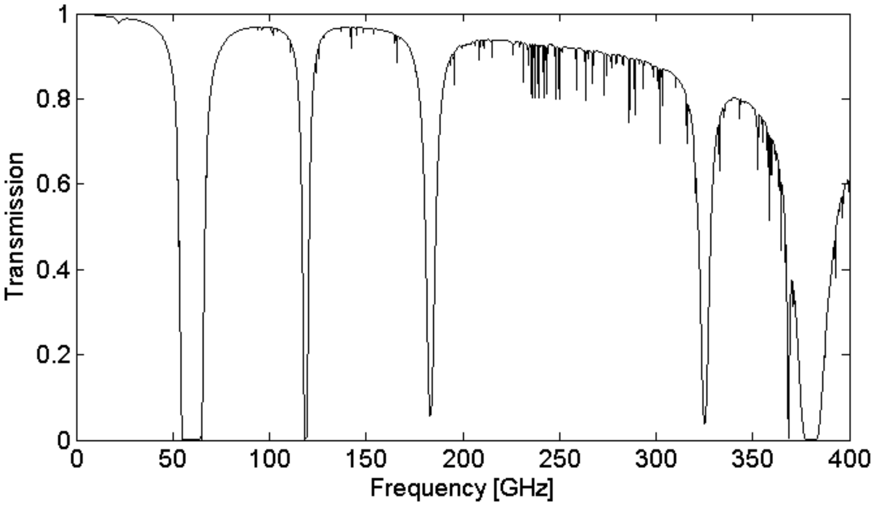

Figure 1.12: Atmospheric transmission spectrum for 1 mm of precipitable water vapor at a 60° elevation angle. As can be seen, even with relatively little water in the air and at a relatively steep elevation, there is very significant absorption in at several frequencies. To maximize the signal, ground based CMB observatories measure the frequencies in between these absorption bands. Additionally, this plot shows where the high frequency cut off starts turning on the the sub millimeter, meaning that we cannot measure that high of frequencies (over $\sim 400GHz$) from the ground. Figure from [7], calculated using [8]

1.3.7 Atmosphere

One major constraint in ground based observations is atmospheric transmission. Even in the driest places on Earth, there is significant water in the atmosphere which has several strong absorption lines in the millimeter and submillimeter. An example of atmospheric transmission in shown in Figure 1.12. Additionally, the turbulence of the atmosphere introduces noise to our data. There are several ways to deal with this atmospheric noise. One way is by getting above the atmosphere, either with balloon or space based telescopes. This is expensive and limits the size of the primary collector. Some ground based telescopes have implemented modulation schemes, such as by using a continuously rotating half-wave plate [42]. Chapter 4 of this thesis discusses half-wave plates in detail.

1.4 This Thesis

My work here at Michigan was to develop enabling technologies for CMB observations. Specifically, I designed, fabricated and tested antireflection (AR) coatings and half-wave plates (HWPs) for the Atacama Cosmology Telescope (ACT). The first set of lenses and half-wave plates were intended for the ACT Polarimeter Experiment (ACTpol), while the later sets were designed for the Advanced ACT Polarimeter Experiment (AdvACT). These instruments are the two latest incarnations of cameras for ACT.

Much of the work presented in this thesis is directed at detecting the primordial gravitational wave signature in the polarization of the CMB. Measurement of this signal would have profond impacts on Physics. It would be the first detection of a quantum gravitational effect. It could additionally shed light on the nature of cosmic inflation. To make this measurement, we need an exceptionally sensitive camera.

The AR coatings I have worked on are truly the best in the field, increasing the transmission of our instrument, increasing its sensitivity. The AR coatings are discussed in detail in Chapter 3. The HWPs will mitigate significant noise in the measurements of large scale polarization modes. The design, fabrication, and testing of HWPs is discussed in detail in Chapter 4. Recent results from the ACT collaboration are discussed in Chapter 5.

Chapter 2

Atacama Cosmology Telescope

2.1 Overview

The vast majority of my work was devoted to instrumentation for the Atacama Cosmology Telescope (ACT). In this chapter, I will discuss ACT in detail. Understanding the instrument in its entirety helped me understand where my work fits in, and what was needed from each element I fabricated.

2.2 Site

ACT is a six meter microwave telescope in the Atacama Desert in Chile. Located just south of the Tropic of Capricorn, ACT has access to $\sim 70\%$ of the sky [43]. The telescope is at an altitude of 5190 m, above a significant fraction of the atmosphere. This site on Cerro Toco is one of the best sites in the world for observing in the millimeter and submillimeter, home to not only ACT but also ALMA, CLASS, POLARBEAR and the future Simons Observatory. The location of the site is shown in Figure 2.1

2.3 Observations

For the CMB, some science goals prefer a *deep* survey strategy, where we continuously observe a small patch and get the noise down (eg small angular scale CMB observation). Other science goals are better optimized with a *wide* survey strategy, were we accept more noise over a larger field (eg cluster science). Formerly, for ACTPol, a mixed strategy was used, observing some small patches deeply and some large patches shallowly. Now, with the AdvACT instrument, the system has sufficient sensitivity that we have moved to just large

Figure 2.1: Location and satellite image of ACT. It is in a mountainous region in Chile near the boarder with Bolivia. The satellite image shows ACT as seen from above, as well as our two nearest neighbors, POLARBEAR and CLASS. Images taken from Google Maps.

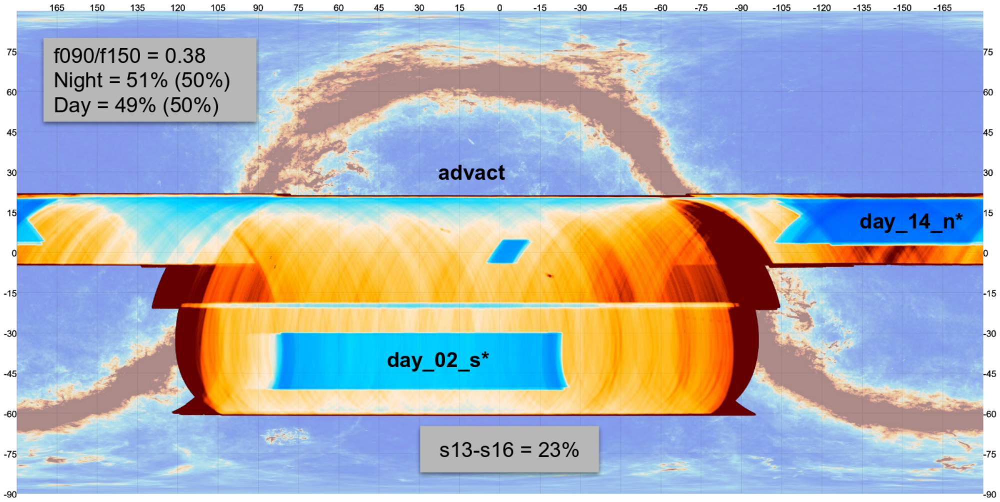

Figure 2.2: Equirectangular projection of the Advanced ACT observation areas overlayed on the Planck all sky dust map. The red and yellow shows night observations, the blue sections are the day time observation fields. As can be seen, we work to avoid observations too close to the Galaxy, as the dust of the Galactic plane will make CMB observations impossible.

fields. The coverage map for the 2016 AdvACT season is shown in Figure 2.2.

In radio and millimeter astronomy, the time streams are analyzed together and used to create an overall map of the sky. This process differs significantly from optical astronomy, which usually stitches together individual images of the sky. In CMB mapping, features of various scale show up as particular Fourier components of the time stream. E.g. with the telescope scanning at 1 degree per second, a 2 Hz signal in the time stream corresponds to a half degree feature.

The telescope beam is measured by scanning over a point source, usually Saturn, Uranus, or Tau A (the Crab Nebula Pulsar). These sources are bright enough they effectively drown out the CMB signal, but don't over saturate our detectors. This allows for a precise measurement of the telescopes point spread function.

While observing, the telescope scans the sky at a constant elevation (angle relative to the ground). This scan strategy keeps the effective thickness of the atmosphere in the telescope line of sight constant. While scanning, only Fourier modes along the scan direction are resolvable. By scanning a patch of sky while rising (patch is is the Eastern sky) and setting (patch is in the Western sky), a patch will be scanned at two different angles, which allows for recovering the full two dimensional map of the patch. This is referred to as cross linking. Additionally, the polarization of a point on the sky will appear at a different angle on our focal plane, which allows us to better control for systematics such as differential gain of the detectors.

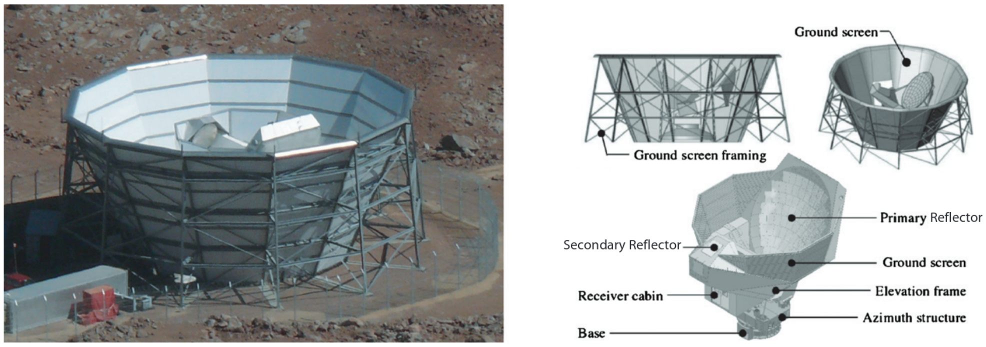

Figure 2.3: (Left) Picture of ACT in its ground screen. (Right) Diagrams of the telescope. There is a large stationary ground screen built around the telescope as well as a comoving groundscreen build on the telescope between the primary and secondary mirrors. These structures help mitigate ground pick up for the telescope.

Another consideration in our observations is the difference between night and day observations. Unlike optical telescopes, millimeter radiation can still be detected during the day. One major difference between day and night observation is the heat of the Sun will cause the panels in the mirrors to deform slightly, smearing our beams and lowering our angular resolution. There are two fronts to the work going into analysis of the daytime data. One is an attempt to track the mirror deformations and deal with them in the model, trying to recover the small angular scale resolution. The second thrust involves accepting the deformations and trying to make maps with the smeared beam, sacrificing the small angular scales.

2.4 Telescope Design

ACT was constructed in 2007. It uses an off-axis Gregorian design, leaving the whole aperture unobstructed. It was designed to have arcminute resolution for CMB observation. The 6 m parabolic primary mirror is made of 71 aluminum panels. The 2 m elliptical secondary mirror is made of 11 panels. It has a 5.2 m focal length and a 3° field of view, allowing for fast scanning. Figure 2.4 shows a ray trace of the mirrors and location of the receiver. ACT has a stationary ground screen (shown in Figure 2.3) , as well as a comoving ground screen, to help mitigate ground pick-up. Just in front of the Gregorian focus, there is a cryostat (receiver) where the filters, reimaging optics, and detector arrays are housed. The cryostat is mounted in a climate controlled cabin under the telescope, along with the control and readout electronics.

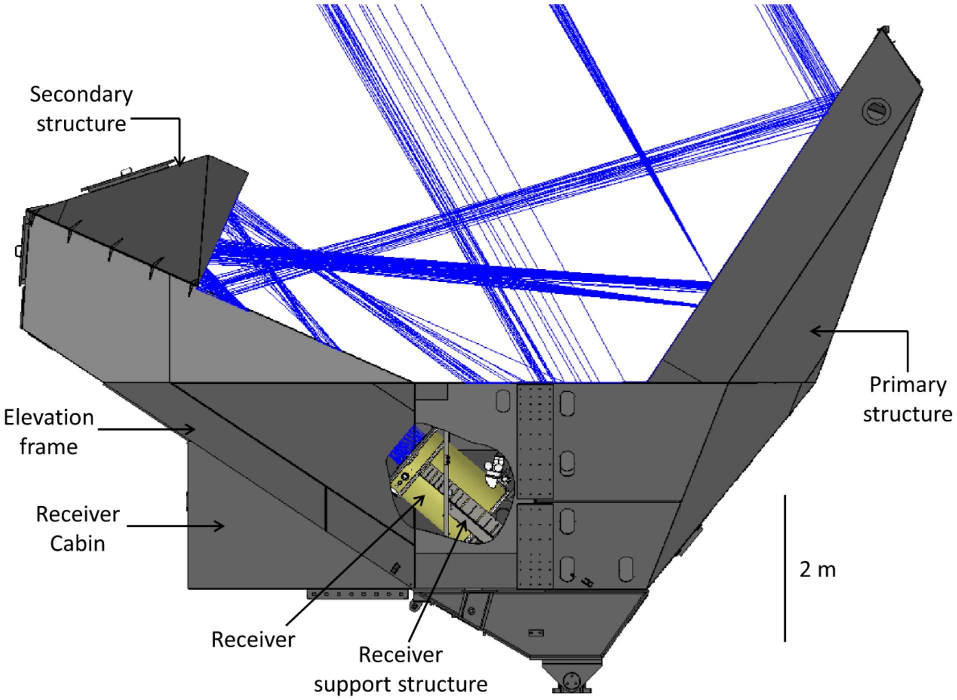

Figure 2.4: Ray trace model for ACT.

2.5 Cryogenics and Optics

ACT uses superconducting detectors that must be kept near 100 mK to work, so the cameras on ACT are housed in a cryostat. The cryostat, shown in Figure 2.5, is a 1.5 m long, 1.1 m diameter cylinder. The remote location of the site made the use of non-recycled cryogenics prohibitively expensive, so the cooling is done with a closed cycle. The pulse tubes cool 40 K and 4 K stages. The ^{3}He-^{4}He dilution refrigerator cools the detectors down to 100 mK. Cooling from ambient temperature takes approximately two weeks. The windows to the cryostat are 6.4 mm thick ultra-high molecular weight polyethylene, with quarter-wave expanded Teflon antireflection coatings. They allow for the transmission of most of the light while supporting the pressure differential of the cryostat.

The cryostat houses three independent cameras, called optics tubes, allowing for a rolling upgrade process. We have installed a new detector array every year for the last 5 years, increasing the sensitivity of the telescope. Additionally, the new detector arrays have added new frequency bands, which will allow for better foreground removal. The detector arrays are described in detail in the following section.

The first elements after the primary and secondary are the half-wave plates (HWPs), which modulate the incident polarization. These are mounted on an air bearing rotation

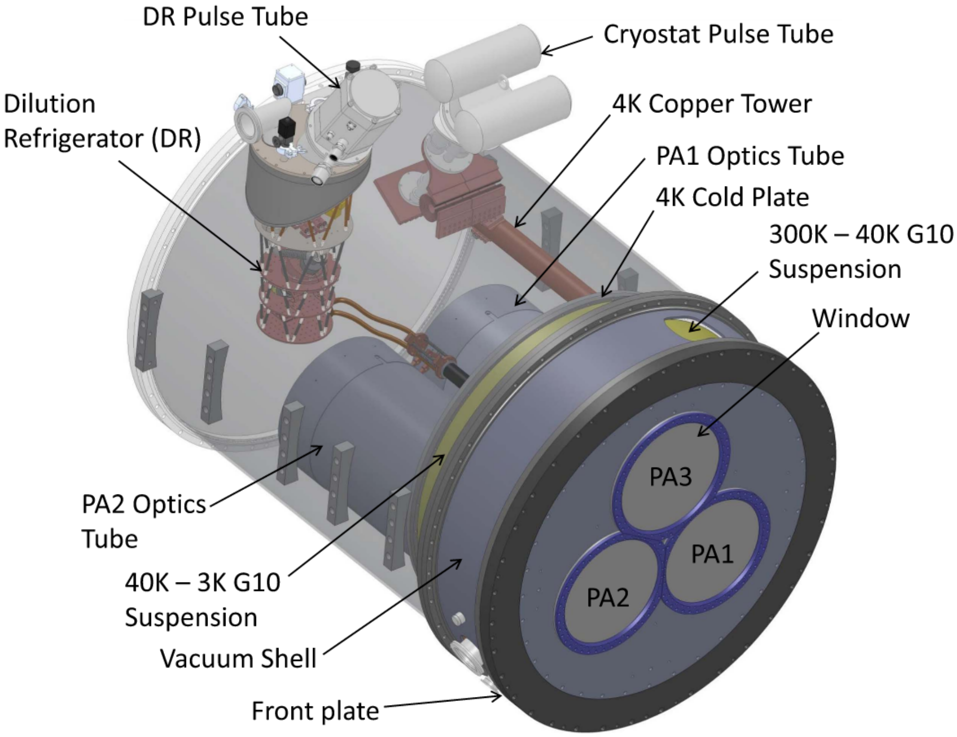

Figure 2.5: CAD model of the ACTPol and AdvACT cryostat with two optics tubes. The third optics tube is removed from view for clarity.

system less than an inch in front of the windows. The HWPs were not in the original design of the system, and thus there was no room for them in the cryostat.

Three reflective IR filters, immediately behind the window, reflect out most of the higher frequency radiation to reduce thermal loading on our system. After them is a stack of low-pass capacitive mesh filters. These further reduce the out-of-band radiation loading on our system. Beyond the filters, a silicon lens images the light at a cold Lyot stop. After the stop, two more silicon lenses reimage the light onto our focal plane. This reimaging system achieves a wide field of view while helping mitigate side lobes and diffraction issues. A schematic of two optics tubes is shown in Figure 2.6.

2.6 Detector Arrays

After the final lens in the optics chain, a feedhorn array is used to couple light from free space onto our pixels. The light is transfered from the feedhorn to the pixel via an orthomode transducer (OMT, seen in Figure 2.8). The signal is then carried by a microstrip line to the detectors (shown in Figure 2.8). For the single frequency arrays for ACTPol, each pixel has two detectors, one for each polarization. For the Advanced ACTPol arrays, each pixel has four detectors, reading two polarizations and two frequency bands simultaneously.

The ACTPol feedhorns, shown in (a) and (b) in Figure 2.7, have corrugated side walls. This gives them high efficiency, symmetric beams, and low cross polarizations. For Advanced ACTPol, we moved to spline profile feedhorns (shown in (c) and (d) in Figure 2.7). The spline profile feeds have a smaller footprint, which was needed to account for the smaller, denser pixels.

The detectors that ACTPol and AdvACT uses are superconducting, transition edge sensor (TES) bolometers. Each detector is kept near its superconducting transition temperature. The phase transition to superconductor is a first order transition, with a very steep resistance vs temperature function, so a small increase in temperature corresponds to a large change in resistance. The signal is carried from the OMT to a lossy transmission line, which deposits its energy on a superconducting island, only weakly thermally connected to the rest of the focal plane. As the island heats up, the resistance of the superconductor increases. This decreases the current going through the system (via a bias line). This change in current is inductively coupled to a superconducting quantum interference device (SQUID), which is then read out. The arrays of detectors for ACTPol single frequency and the AdvACT HF array are shown in Figure 2.8. The whole array package is shown in Figure 2.9.

The detector bands were designed to avoid the water absorption lines in the atmosphere (seen in Figure 1.12). The atmosphere has good transmission below 50 GHz, bands centered

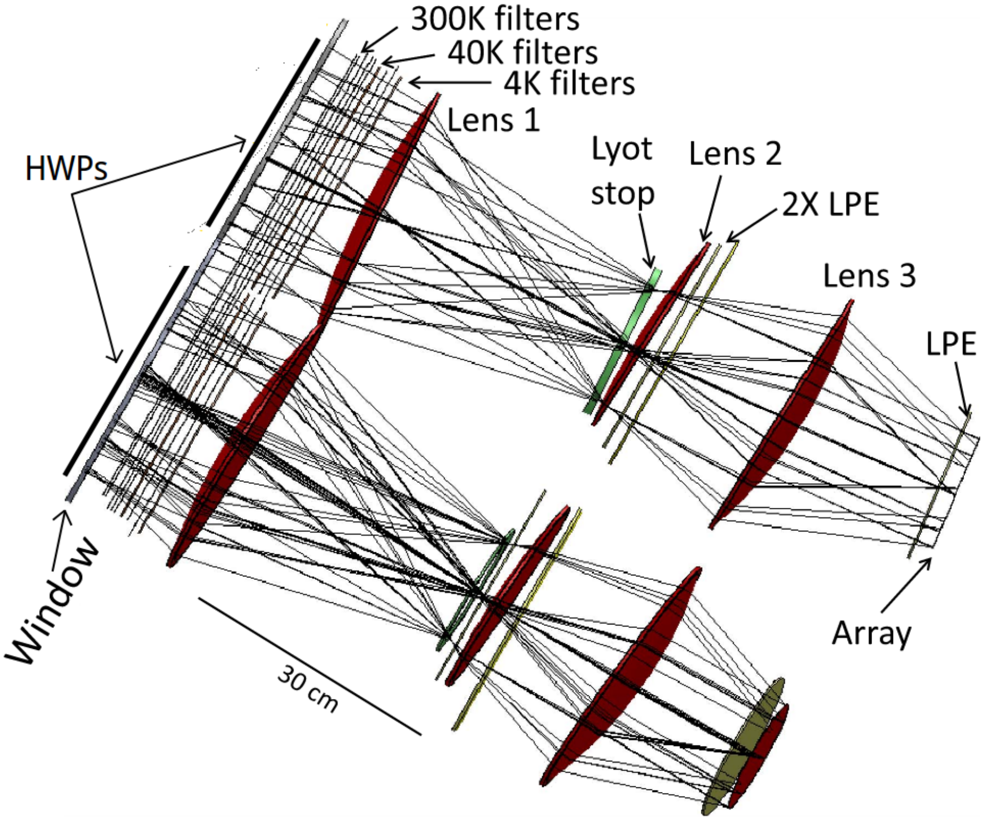

Figure 2.6: Schematic diagram of the ACTPol optics tubes. Light comes in from the top left, passing first through the half-wave plates which are just outside the cryostat. Then the light passes through the window into the cryostat, through a series of IR blocking filters. The first lens creates an image plane at the Lyot stop. Then the light passes through an additional lens, then low-pass filters, then the final lens before being imaged onto the focal plane feedhorn array.

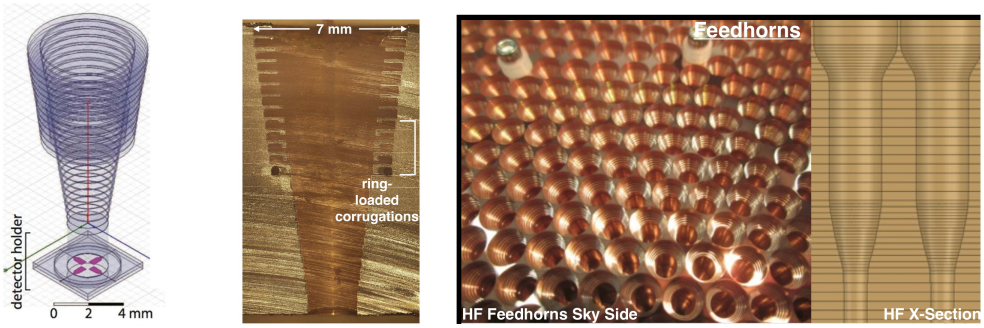

(a) (b) (c) (d)

Figure 2.7: (a) CAD model of corrugated ACTPol feedhorn. (b) Cross section image of one of the ACTPol corrugated feedhorns for the MF array. (c) Copper plated spline profile feedhorn array. (d) Model for AdvACT spline profile feedhorn. (a) and (b) from [9]. (c) and (d) from Mike Neimack.

around 90 GHz and 150 GHz, and from about 200 GHz out to 320 GHz. The middle frequency arrays for Advanced ACTPol are set to be sensitive in the 90 and 150 GHz bands. The high frequency array is set at 150 and 220 GHz. The low frequency array is set at 20 and 40 GHz.

For the ACTPol instrument, the detectors were fabricated on three inch wafers. The focal plane for each optics tube was comprised of three hexagonal wafers and three semihexagonal wafers. For the 150 GHz single frequency arrays, this totaled 512 pixels for 1024 detectors. For the 90/150 GHz array, there were 255 pixels with 1020 detectors. For the AdvACT instrument, fabrication moved to six inch wafers. This meant the focal plane could now be filled by a single hexagonal wafer, simplifying fabrication and integration. Advances in the pixel design also allowed for smaller pixels and more efficient wiring. The HF array has 503 illuminated pixels. The LF array will have 44 illuminated pixels.

2.7 Data Readout

The detectors use changes in resistance to detect incident radiation. To read this change in resistance, we use SQUID amplifiers, which are very low-noise amplifiers inductively coupled to the detectors. The readout system makes use of multiplexing (reading out several detectors along a single transmission line) to simplify wiring and reduce the load on the cryogenics. This is achieved by using SQUID switches, connecting and disconnecting each pixel to the transmission line in rapid succession (time-domain multiplexing). For ACT, we readout 32 detectors per transmission line. This time-domain multiplexing architecture has the

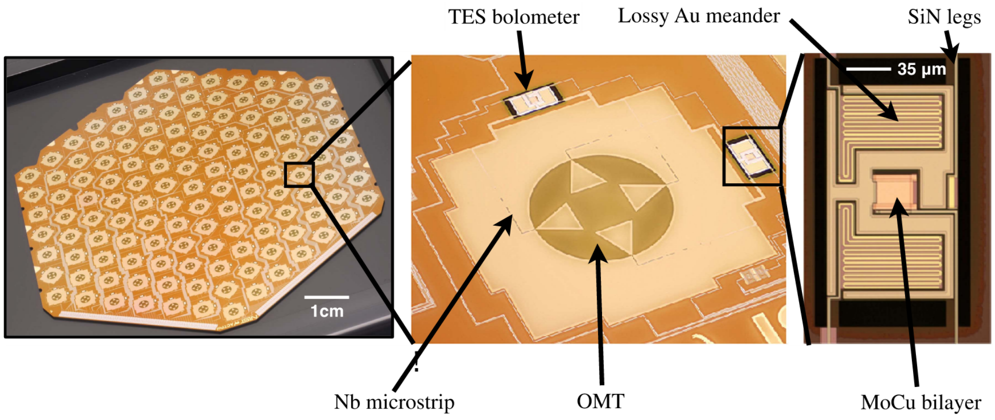

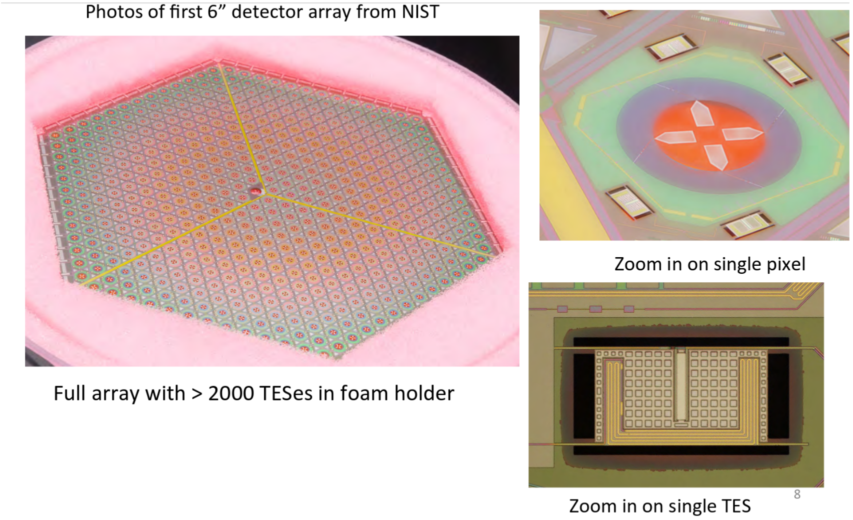

Figure 2.8: (Top Left) ACTPol 150 GHz detector array. (Top Center) Close up view of a single 150 GHz detector. (Top Right) Bolometer). (Bottom Left) First AdvACT detector array fabricated by NIST. (Bottom Upper Right) Close up of new pixel. (Bottom Lower Right) Bolometer.

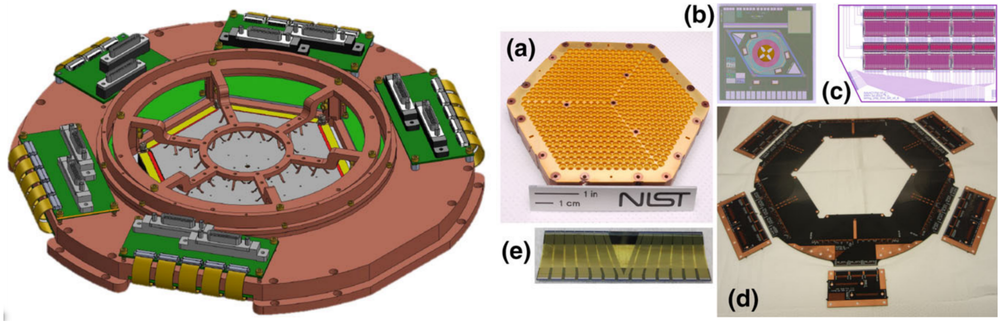

Figure 2.9: (Left) CAD model of the AdvACT HF array package. (a) Gold plated feedhorn array for the AdvACT HF array. (b) Single HF test pixel. (c) SQuID array on multiplex chip. (d) Readout chips for the HF array. (e) Flexible circuitry for HF array readout. Figure from [10]

advantage over frequency-domain multiplexing as each TES is effectively in a separate circuit, and can be biased individually.

The detector data is readout at around 15 kHz, which is then resampled down to 400 Hz. The data is stored as so-call time-ordered data (TOD) objects. Each TOD is a 10 minute chunk of data, containing data from all of the detectors, as well as telescope housekeeping data.

2.8 Conclusion

In the following chapters, I describe my specific contributions to the instrument. This includes the antireflection coatings for the silicon reimaging optics, and my work on the HWPs. I conclude with a discussin o the science which has been carried out with this instrument.

Chapter 3

Antireflection Coatings

3.1 Introduction

ACT and other millimeter telescopes use silicon lenses for reimaging optics. Silicon is a great material to use for the optics for several reasons. Its high index allows for very fast optical designs. Its low dielectric loss minimizes any light being abosorbed by the lenses. Its high thermal conductivity keeps the whole lens at uniform temperature.

One of silicons benefits does come with a side effect though. The high index of silicon means that if a surface is uncoated, there would be a $\approx 30\%$ loss from reflection. After three lenses (six surfaces), this would leave almost no light left for the detectors. Luckily, there are methods for mitigating reflections off each surface. This is generally referred to as antireflection (AR) coating.

Reflection is caused in effect by a difference in the index of refractions on each side of an interface. At normal incidence at an interface of dielectrics with indicies n_1 and n_3, the reflection is given by

$$R = \frac{(n_3 - n_1)^2}{(n_3 + n_1)^2} \tag{3.1}$$

An AR coating is an additional layer of dielectric, with an index between the two outer dielectrics, is inserted at the surface. With three layer, there are now two interfaces. The total reflection has to account for reflections off of each interface. For the case of a single layer AR coating, with the middle layer having index n_2 and thickness d, the reflection works out to

$$R = \frac{n_2^2(n_1 - n_3)^2 + (n_2^2 - n_3^2)(n_2^2 - n_1^2) * \sin^2(n_2 d\omega/c)}{n_2^2(n_1 + n_3)^2 + (n_2^2 - n_3^2)(n_2^2 - n_1^2) * \sin^2(n_2 d\omega/c)} \tag{3.2}$$

By carefully choosing an index and a thickness of the layer, the reflection at a single frequency can be effectively set to zero. If the thickness is

$$d = \frac{\pi c}{2 n_2 \omega} = \frac{\lambda}{4 n_2} \tag{3.3}$$

and the middle layer index is

$$n_2 = \sqrt{n_3 * n_1} \tag{3.4}$$

then we can see that equation goes to zero at wavelength λ. This specific single layer coating is referred to as a quarter-wave coating, as the thickness of the layer is a quarter of the wavelength in the medium. This can be understood physically as destructively interfering the reflection of the first interface with the reflection off the second interface. If the thickness is a quarter-wave, then the path length difference between these two reflections is a half-wave, causing destructive interference.

With a single layer you can effectively cancel out reflection at a single frequency. By adding more layers, there are more free parameters that can be tuned, so multiple frequencies can have their reflections effectively mitigated, creating a broadband AR coating. For my work, I have created one-, three-, and five- layer AR coatings for various applications. These coatings were all fabricated using silicon metamaterials.

3.2 Metamaterials

AR coatings have ideal performance only if both the thickness and the index of a material can be fully tuned. The thickness needs to be on the order of the wavelength of interest, and the index needs to be somewhere in between those of the incident and transmission media. A problem inherent to most AR coatings is that they are made out of real materials, and thus only discrete values of the index of refraction are available, as this is an intrinsic property of a dielectric.

Most AR coatings at millimeter wavelengths are made of plastics. They are a varied class of material that have a reasonable range of indicies of refraction, and are relatively easy to manufacture. One of the primary difficulties of using plastics for AR coating on silicon lenses is the risk of delamination. The lenses are typically used at 4 K, but the AR coatings are usually applied at elevated temperatures. This thermal cycling causes problem, as the various plastics have different coefficients of thermal expansion than the silicon of the lenses. This leads to strains during thermal cycling, which causes delamination. Plastics are also generally lossy materials at the frequency of the CMB observation, and tend to have a low thermal conductivity, which can lead to absorption and thermal gradients across the coating.

Metamaterial is a general term that indicates some global property is distinct from that of the underlying material. Simulated dielectrics are metamaterials which are a combination of two materials (often vacuum and a simple dielectric), with a dielectric constant somewhere between those of the underlying material. The key to these materials is that, at the frequency they operate at, the interlacing feature size of the different materials is significantly smaller than the wavelength of light.

These sort of simulated dielectrics are found in nature. The eyes of moths have a nanostructure of small bumps on the order of 200 nm. This structure was first theorized by Bernhard in 1967 as a way of minimizing reflection, and was later experimentally confirmed.

There has been extensive work to understand the properties of these structures from a theoretical perspective, starting in the quasi-static (pitch $\ll \lambda$) regime and expanding to finite wavelength. For my purposes though, I stick to an empirical model following [44] to approximate the behavior as a function of the relative fill fraction of the two materials.

3.3 Previous Work from McMahon Lab

The AR coatings made in our lab are made of stepped pyramids of silicon. We fabricate these coatings with a custom three-axis dicing saw in our lab (shown in Figure 3.1) built by a previous graduate student [45]. They are made by dicing a set of evenly spaced, nested grooves with blades of decreasing thickness. The silicon is then rotated 90 degrees, and the process is repeated. This leaves behind the stepped pillar geometry, such as that shown in Figure 3.2.

When I came into the lab, they had already fabricated a set of three lenses with a two-layer AR coatings for the ACTPol instrument, and were working on their first set of three-layer AR coated lenses when I jumped in.

3.4 Design Overview

To start the design process, I wrote an analytic modeling code. The code has two main components. The underlying package I wrote solves Fresnel's Equations [46] and calculates the reflection and transmission at any frequency for an arbitrary multilayer geometry. This code is copied in the first appendix of this thesis. The other component I wrote was a Monte Carlo code to explore parameter space and find the combination of indicies and thicknesses for each layer to minimize the reflections for the set of frequencies I chose. These indicies and

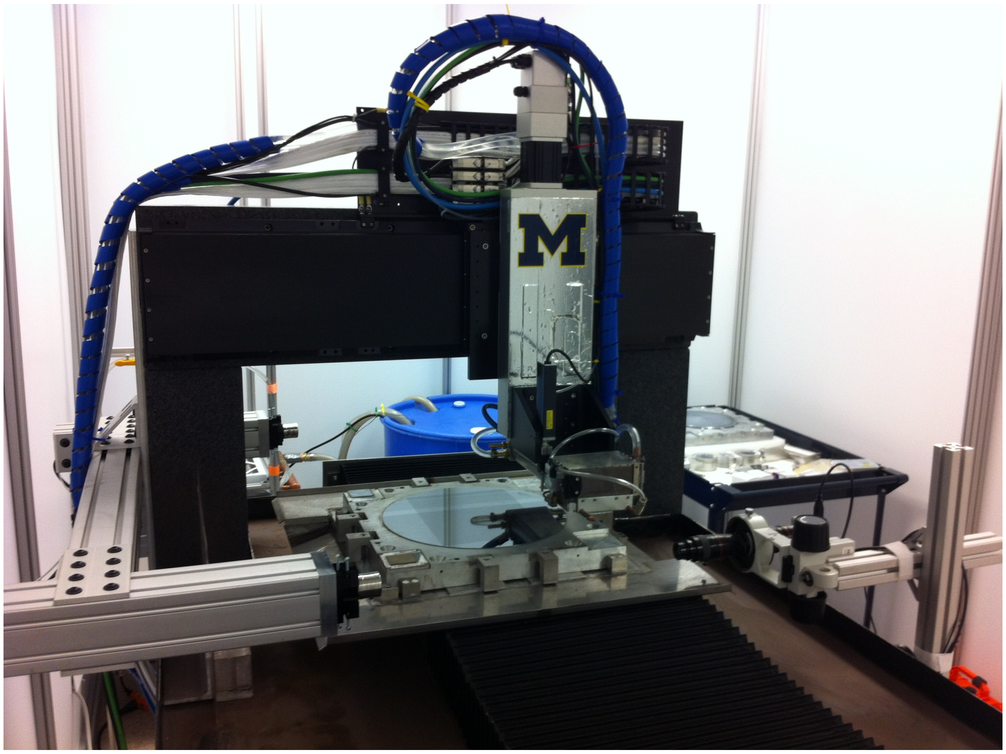

Figure 3.1: Image of the custom dicing saw used to fabrication silicon metamaterials. The silicon to be cut is mounted on the x axis, and the saw is mounted in the y-z plane. Each cut, the saw moves along the y axis, with the z changing to follow the shape of the silicon. After each cut, the silicon is the moved by the pitch of the cuts in x, and the process is repeated. After the set of grooves is completed, the silicon is rotated, and the cutting begins again.

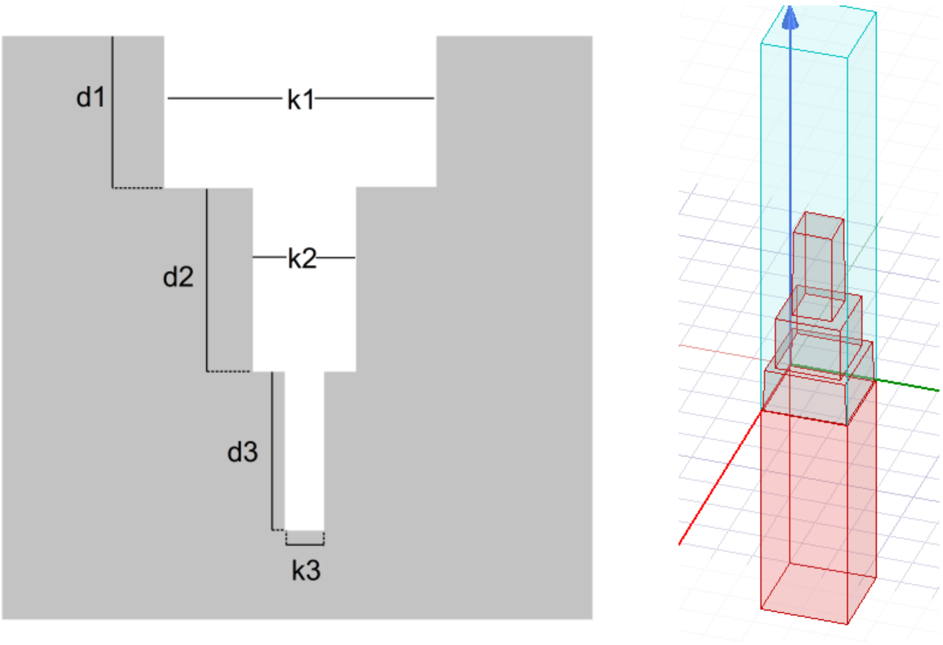

Figure 3.2: Left: Generic geometry for three layer AR coatings. The kerfs and depths, along with the spacing between cuts (or pitch) can all be optimized to cover the frequency band of interest. Right: HFSS model for a three layer coating. The red is silicon, the blue is vacuum. The boundary conditions simulate a continuous array of such pillars, which is an excellent approximation for our purposes. The scattering parameters (transmission and reflection) are measured at the ports at the top and bottom of the cell.

thicknesses make the implicit assumption that the layer each behave as normal dielectrics, but that is not quite the case.

We operate our metamaterials near the so-called breakdown frequency. In this regime, the simulated dielectrics aren't well described by the analytic model. To overcome this, we use Ansys High Frequency Structure Simulator (HFSS) to do numeric modeling. This is a commercial finite element analysis (FEA) software that allow us to model our metamaterial structure. We us HFSS CAD to design a unit cell of our structure. Continuous boundaries are used to simulate our unit cell as an infinite array. Ports above and below the cell inject the frequencies of interest through the structure and read out the transmission and reflection. A model of a three layer structure is shown in Figure 3.2.

The initial inputs for thickness and fill fraction come from the analytic Monte Carlo combined with the index to fill fraction model in [44]. The initial pitch (spacing between cuts) is chosen to be about a fourth of the central wavelength. Once I have the initial numeric model, I use HFSS's in-built optimization function to to vary the pitch, kerfs (cut widths), and depths of the cuts to minimize reflection, under constraints placed by our fabrication system (e.g. total cut depth).

After getting the final design, we do a tolerance analysis, checking how much our performance degrades given particular error. The main source of error is depth variation due to unevenness of our silicon surface. This can be on the order of 10 um. In practice, the depth error is all absorbed by the top layer of the AR coating. This is fortunate as the top layer has the greatest tolerance to depth errors. This is primarily due to the fact that as it has the lowest index of refraction, thus same physical thickness error corresponds to a smaller change in phase thickness than in the other layers. Additional error can come from the kerf of the cut changing as the blade wears.

3.5 Fabrication Overview

For coating, a lens is mounted on a aluminum plate for cutting. Metal tabs press down on the flange of the lens to hold it tightly in place. This plate can then be mounted on the saw in one of four orientations (in 90° increments). This allows us to cut in orthogonal directions. It also allows us to cut very curved surfaces.

When cutting a lens, a contact metrology probe is used to measure a coarse grid of points on the surface. The surface data, along with the defined surface parameters, are used to fit the center and the angle of the mounted lens. A periodically remeasured calibration transfers the model from measurement probe coordinates into saw blade coordinates. From the fit and the saw calibration, files are generated which specify the position and depth of each groove.

Before beginning each cut, each blade is run through a ceramic block. This works to clean the blade, which means cleaner cuts. We measure the blade profile on a spare piece of silicon and check that the kerf (cut width) is within acceptable parameters. Then we do a final z calibration by going to a point in a CAM file and bringing the saw down until it just scratches the surface. The length of the scratch is sharply proportional to the depth of the scratch such that measuring the length to a tenth of a millimeter gives the depth to within a micron for sufficiently shallow (less than 30 μm deep) cuts. We use this final calibration to shift the CAM files up or down. This step is necessary as the radius of our saw blades are not micron accurate, and evolve over time.

A single set of cuts covers either the full surface of a lens (for low-curvature lenses) or the first half of the surface (for high-curvature lenses). If the total height difference between the edge of the lens and the center of the lens is greater than 17 mm, then the spindle will hit the center of the lens as the saw cuts the second half of the lens. To avoid this problem, only the first half of a lens is cut, then it is rotated 180° and cut again.

3.6 Measurement Overview

To ensure the quality of the AR coatings our lab fabricates (and verify our models), we measure the reflection off of the coated (or uncoated) surfaces using our home-brew reflection measurement setup, or reflectometer. On one side of the setup, a swept frequency source would direct power at the sample surface at about 10 degree angle of incident. On the other side, the power was collected and deposited onto a power diode. The source is square-wave modulated at 100 Hz, and read out with a lock-in amplifier. The calibration was done using an aluminum mirror, with near perfect reflection. The power reflected from the sample was divided by this calibration to get fractional reflected power.

When I first came into the lab, the source and diode just used feed horns to control the beams. This lead to most of the power of the source not making it back into the power diode. The low signal meant longer integration times and lower SNR. While in the lab I helped upgrade the reflectometer to include collimating mirrors. These were off-axis parabolic mirrors which collimated the beam, significantly boosting the signal. In addition to boosting the signal, this collimation of the beam serves to clean the signal. Using just the feed horns and an uncollimated beam, the diode would measure a range of optical paths with different angle of incidence, leading to a smearing effect. Collimating the beam, as well as inserting a stop before the second mirror, dramatically cleans up the beam, providing a much sharper spectrum.

An additional problem with the earlier iteration of the reflectometer was in the source itself. Our source consists of a local oscillator, which can operate from 8 to 14 GHz, and a one of two chains of multipliers to go to the frequency range of interest. The multiplier chains nominally produced 9x or 12x harmonics of the local oscillator, but in fact produce effectively every harmonic and try to filter out all but the 9x or 12x. These original sources did not do a sufficient job filtering, so there was harmonic leakage from other frequencies into our power detector. This was partially fixed by getting a higher quality 9x and 18x multiplier chains (we still use the inferior 12x). Overall these improvements drastically improved our measurement precision.

3.6.1 Silicon Measurements

One interesting project I did with the new reflectometer set up was to measure the optical properties of silicon. Using all three of our bands in the upgraded setup, I measured the reflections off of an uncoated piece of silicon just over four millimeters thick. The data are plotted in Figure 3.3. By fitting this data to an analytic model, I was able to constrain the real and imaginary parts of the index of refraction, assessing the quality of the silicon. Figure 3.4 shows a contour plot for the real and imaginary parts of the index of refraction using the data from Figure 3.3. Our system didn't detect any signature of dielectric loss, but placed an upper limit of the loss tangent at $tan(\delta) < 1 * 10^{-3}$, which is sufficiently low for our purposes.

I learned the hard way it is always important to do our own quality checks of the silicon before fabrication. One piece of silicon was giving odd reflection data when uncoated. Not worrying too much about it, I moved on to fabrication. Later, when the coated silicon data was still giving strange data, I tried modeling it with a large loss tangent, and then found the data to match. This piece of silicon had such a high loss that it was unusable.

3.7 Projects

While the overviews above show the general idea of our system, each project I worked on had adjustments and constraints that needed to be addressed on an individual basis.

3.7.1 Advanced ACTPol Lenses

The Advanced ACTPol instrument will have four dichroic detector arrays: two 90/150 GHz mid frequency (MF), one 150/220 GHz high frequency (HF), and one 24/38 GHz low frequency (LF). Each of the reimaging optics uses three plano-convex silicon lenses approximately 30 cm in diameter. All of these lenses have or will have three layer AR coatings

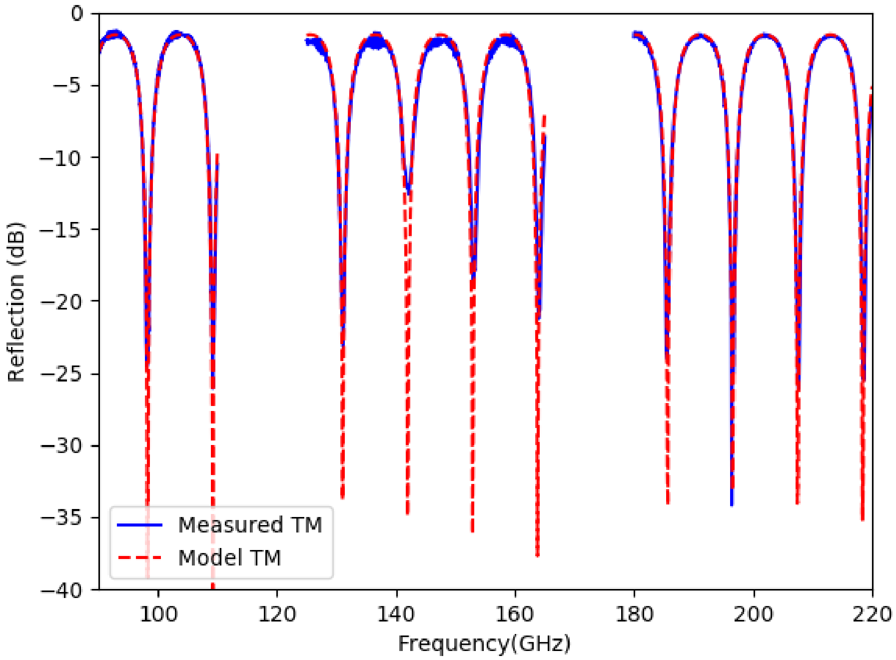

Figure 3.3: Reflection measurement off an uncoated silicon plate 4.02 mm thick. The measurement uses all three of our bands, and behaves as predicted. The measurement noise is sufficiently low that we can effectively measure the loss tangent of the silicon.

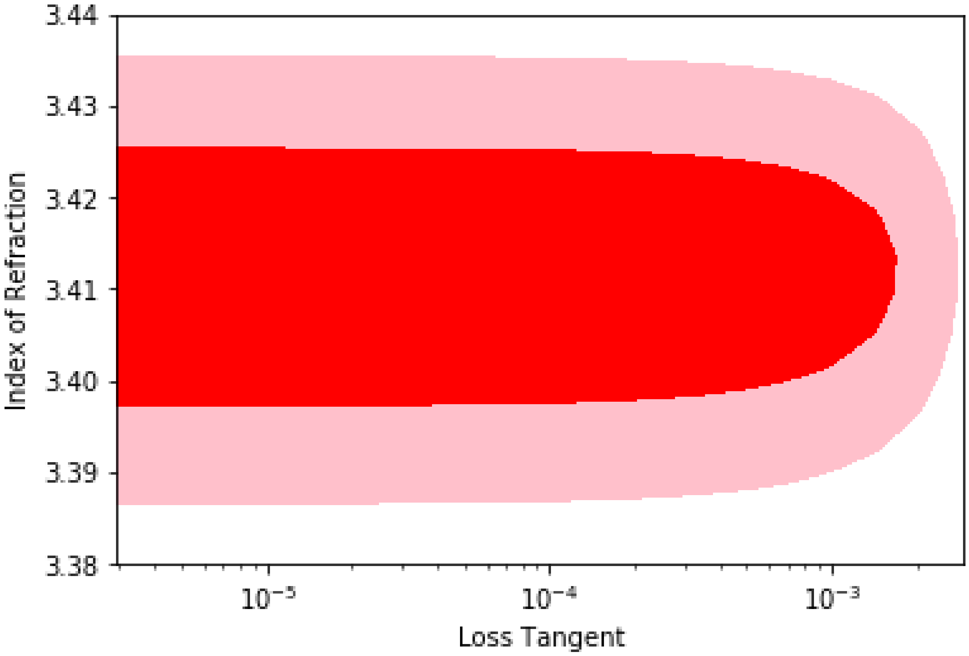

Figure 3.4: Using the reflection data of the uncoated silicon, I ran a code to fit the index of refraction and the loss tangent of the silicon. Shown are the one and two sigma contours for the loss tangent and the index of refraction. As can be seen, the index is well constrained, but the loss tangent can be anywhere from 10^{-3} to zero. The loss tangent is less than $1 * 10^{-3}$ at one sigma.

Antireflection Coating Parameters			
Pitch μm	Layer	Kerf μm	Depth μm
ACT Mid Frequency 90/150 GHz			
450	1	230	500
	2	165	310
	3	25	257
ACT High Frequency 150/220 GHz			
295	1	160	305
	2	80	185
	3	20	152
ACT Low Frequency 20/40 GHz			
1375	1	735	1520
	2	310	1000
	3	70	750
PIPER 200 GHz			
294	1	75	201
THz Coating 1.4 THz			
50	1	12	28
5-Layer 50-350 GHz			
246	1	179	440
	2	132	295
	3	82	221
	4	43	162
	5	20	154

Table 3.1: AR coating design parameters. The high and low frequency designs are roughly scaled versions of the MF design, but some changes were made to fully optimize the bands.

fabricated by our lab. At the time of writing this, I have completed the coatings on all but the LF lenses.

MF Lenses

When I came into the lab, the design work on the MF AR coating was finished, and the fabrication was underway. The coating had been designed by a previous graduate student [4], and fabrication had just begun on the first lens. The design parameters are given in Table 3.1.

One problem with the fabrication was in cutting the top layer. The cut was 230 μm wide and 500 μm deep. This was the largest cut the saw had done, and it appeared to be taking a toll on the gantry. Even when the cutting was slowed down, the cutting process was putting significant stress on the saw stages, leading to drifts in the absolute positioning of the z-stage. When testing before and after the dressing cuts, I found that the blade would shift upwards several tens of microns. Then as I let the system settle, it would drift back down. This level of error was beyond our tolerance.

Our solution was, instead of using a 230 μm blade, to take multiple passes using a thinner blade. Originally we tried using a 160 μm blade, with two overlapping cuts. This was found to be highly problematic. The second cut put an asymmetric force on the blade as it cut. This ended up leading to significant warping of the blade, and severe degradation of our cut profile, reducing the coatings performance.

The second (and currently employed) solution was to make two cuts with a significantly thinner blade (60 μm), which would define the edges of the kerf, leaving a spine down the center. A thick blade (180 μm) is then used to clear out the central spine. In this process, there is no asymmetric forces on any of the blades, mitigating any warping. These processes were learned while the cutting of the first set of MF lenses was occurring, leading to a somewhat degraded performance. These lessons served me well though in future fabrication and development.

Later, the lab fabricated a second set of identical lenses for the second MF array of AdvACT. With no new development to do, the cutting went very smoothly. There was fewer than one broken pillar per 100,000. Note the excellent performance (averaging 0.3% reflection across the band) and excellent agreement with our numerical simulation. The transverse magnetic and transverse electric modes measured off the flat side of Lens 3 are shown in Figure 3.5.

HF Lenses

While working on the fabrication of the first set of MF lenses, I began working on designing the HF lenses. The designs for the MF couldn't just be scaled down in size, since the thinnest cut would have been thinner than we could have made it using the current saw setup. I went through the process described above, with minimal variation. The final design is given in Table 3.1.

The fabrication for the HF lenses was straightforward. As the thickest cut was 160 μm thick, and not as deep as the MF, there was no need to do any complicated cutting process. We just used the correct thickness blades and cut each groove in one pass, from thickest to thinnest.

Once again the yield was near-perfect, with very few pillars broken during fabrication. I used the reflectometer to measure the reflection off of the flat side of Lens 3. The data are show in Figure 3.6. As can be seen there is excellent performance and excellent agreement with the model. Despite the tighter tolerances of the HF design, we achieved the desired performance.

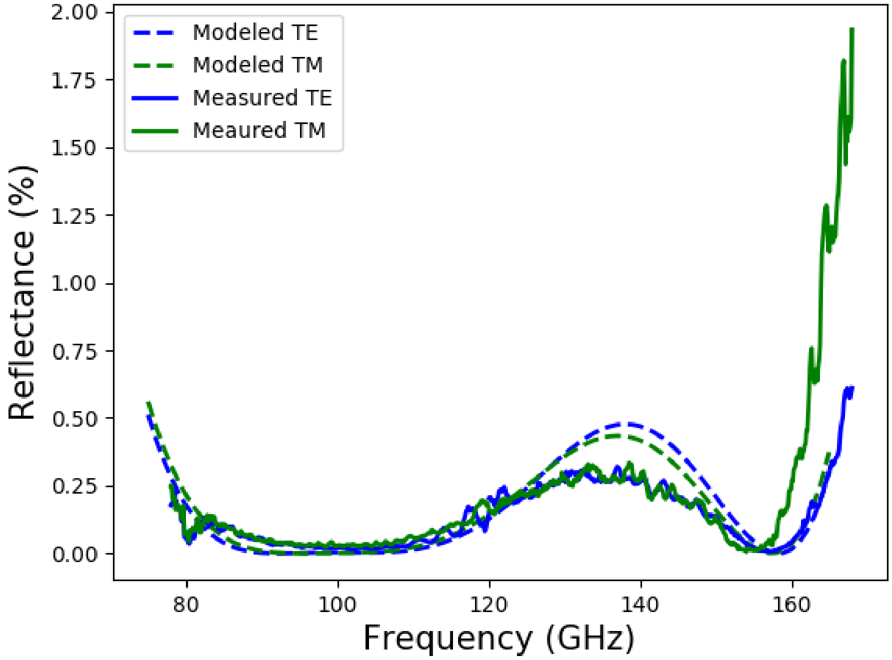

Figure 3.5: Reflection measurement from the flat side of the Advanced ACTPol MF Lens 3. Shown are both the measured and modeled transverse electric (TE) and transverse magnetic (TM) modes. For the measurement, two sources are used: one below 120 GHz and one above. No additional calibration was needed to get them to line up that well. Our measurement system is simply well calibrated and stable.

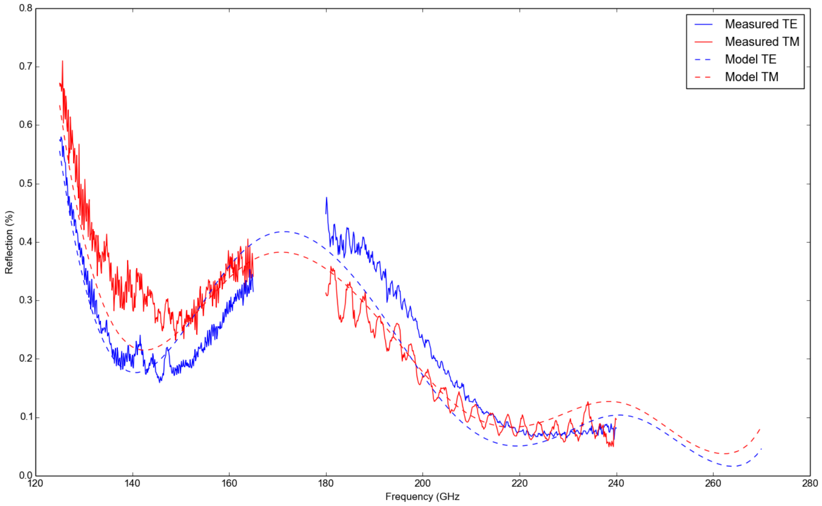

Figure 3.6: Reflection measurement from the flat side of the Advanced ACTPol HF Lens 2. Again two sources were used to cover a larger swath of frequency range, although we don't have the capability to measure up to as high a frequency as the coating operates.

LF Lenses

I have additionally finished the design work on the final set of lenses for Advanced ACTPol, the LF array lenses. The AR coating for these lenses is optimized for 20-40 GHz. The design is shown in Table 3.1. The modeled performance is shown in Figure 3.7. The design itself is nearly just a scaled up version of the MF design, with a few tweaks. The design process was identical to the others, but the fabrication work will pose some significant challenges that need to be worked out before we can start full scale production.

By scaling the coatings to cover such low frequencies, the feature size grew significantly. The previous deepest cut of 1.1 mm for the MF was more than tripled in the design. The cuts are wider and deeper than anything we've done before, and will require many passes for each layer. To keep strain of the saw at a minimum, we only cut 500 μm deep for any pass. This means three passes are required to get to the full depth of the top layer. Getting to the bottom of the second layer will take an additional two passes, as will the bottom layer. The top layer is so wide it will take seven cuts across to get the kerf right. The second layer will take three cuts across. The bottom cut will luckily just be one pass wide. The cutting process is shown in Figure 3.8. All told, this will take 29 passes, as opposed to 5 for the MF and just 3 for the HF. As this is mostly an extension of work we have previously done, I don't foresee any significant problems to crop up in the process development, but

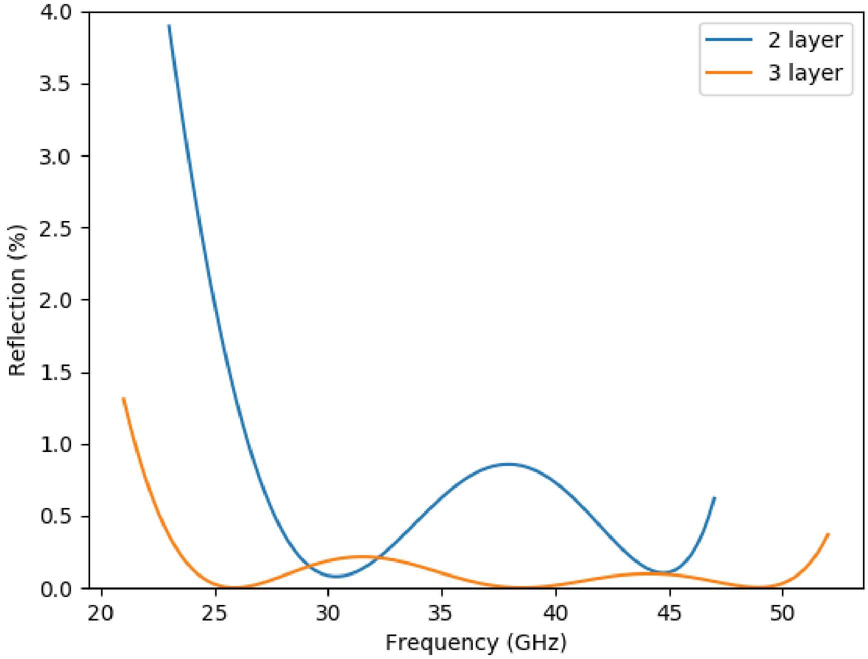

Figure 3.7: Modeled reflection from two- and three-layer AR coatings for the Advanced ACTPol LF array. As can be seen, going to a three-layer coating dramatically broadens the frequency bandwidth. In order to properly cover the LF bands, we need the three layer coating. This coating has not yet been fabricated or deployed.

the unknown unknowns are often the most difficult to deal with.

There is a bright side to this array though; the tolerances will be greatly increased. This may help meet production schedule as we may need less work between each set of cuts to check blade radius, as even 10 μm blade wear won't degrade the performance in a significant way.

3.7.2 PIPER

An additional capability I worked on was getting our saw to cut concave lenses. While the ACT lenses are all plano-convex, it is not uncommon for other reimaging optics to include concave-convex lenses. As such, it was of interest to tweak our system to be able to handle this. The work involved a few measurements to calculate the maximum concavity of the lenses. After that, it took a bit of work to get the fit code working properly.

This work was then tested out on silicon lenses for PIPER, a NASA balloon-based CMB telescope. The detectors for this experiment are single frequency detectors centered at 200

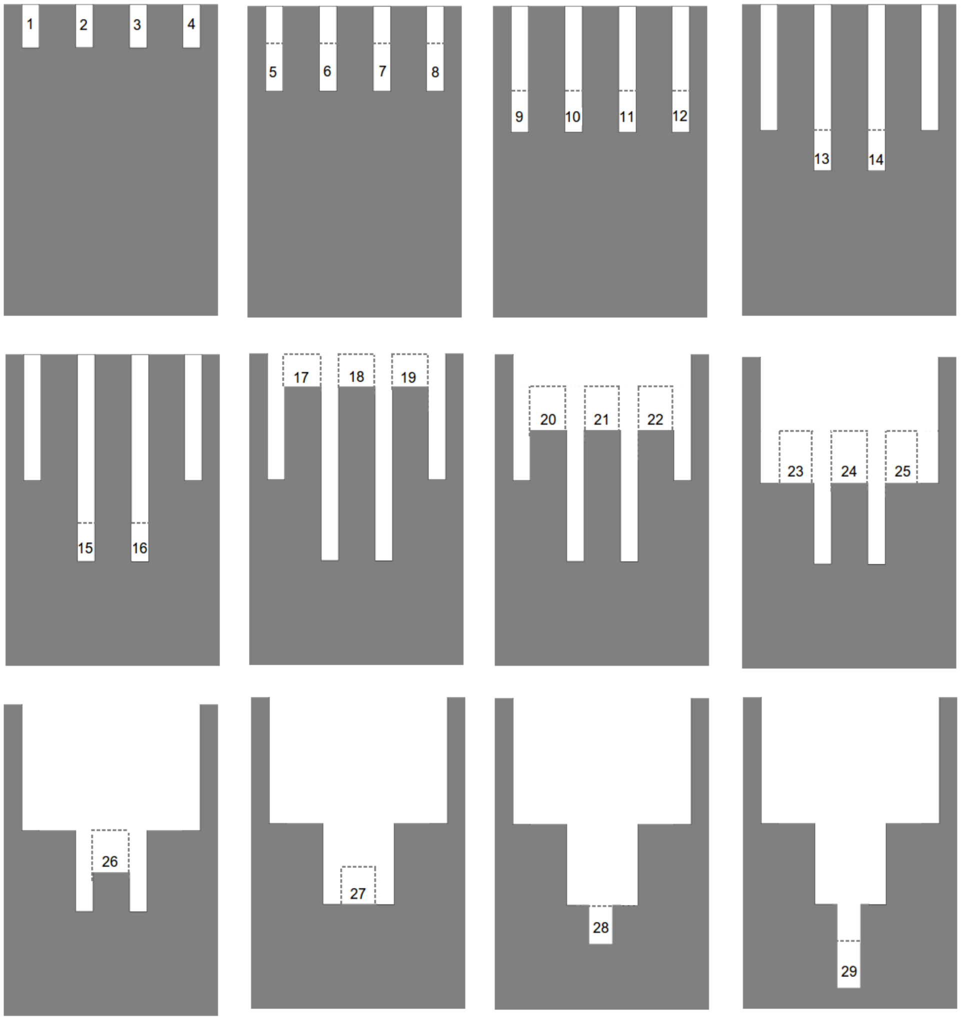

Figure 3.8: Cartoon of the cutting technique for the LF AR coatings, with the cuts numbered. The gray is the silicon. The massive size of the features means we will need to take 29 passes with the saw to clear out all of the silicon without putting too much strain on the spindle. Starting with non overlapping cuts, then going to the clearing cuts ensures that the cutting force is applied symmetrically across the blades, which helps keep the cut profile stable.

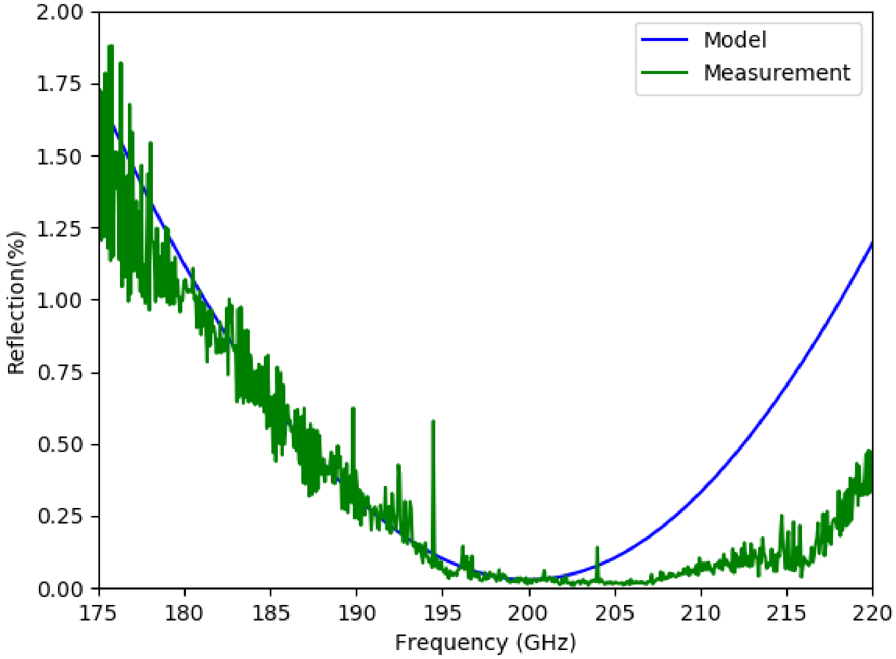

Figure 3.9: Reflection measurement from the PIPER lens single layer AR coating fabricated in lab. The measured reflection does not quite match the modeled performance at higher frequencies. This may be due to the difficulty in measuring a slightly concave surface.

GHz for the test flight. I designed and cut a single layer AR coating for two lenses. The performance of these coatings was measured in lab, and is shown in Figure 3.9.

3.7.3 Five Layer AR Coating

To push the bandwidth limits of what our system was capable of, I designed, fabricated and tested a five-layer AR coating. Again I followed my previous design scheme of analytic modeling with a Monte Carlo, then porting that over to a numeric model. In the design work, several significant constraints affected the design. First, this was a side project and was just being carried out with the saw blades we had on hand. This limited our possible cut widths to a finite set. This obstacle could easily be overcome by ordering different blades.

The second major constraint was a permanent issue inherent to the fabrication technique. While using dicing blades, an important number to keep in check is the blade-width-to-blade-exposure ratio. The blade exposure is effectively the total depth the saw blade can reach. If this ratio gets above 50 (e.g. 1 mm exposure for a 20 μm blade) then the cutting process becomes unstable and the risk of breaking the blade goes up significantly. This tightly constrains what our possible five-layer geometries could be.

As we add more layers, the total thickness of the optimal coating increases. Additionally, as we add more layers, the optimal index for the bottom layer gets closer to that of pure silicon, which means a thinner blade. These two factors conspire against making a high quality five-layer coating. The design used the thinnest blade we had (20 μm) as deep as it could possibly cut (1000 μm).

There is an additional problem at hand. As more layers are added, the difference in index between two subsequent layers is smaller. This then means that the kerfs of two nested cuts are closer in width. If they get too close, then we lose definition between the layers, and they just slope together. This means we don't get a hard reflection off each surface, so the interference doesn't work as well.

To address the problem of the layers blending together, I decided to slightly change the geometry. For our previous cuts, we had centered each nested cut in the previous cut, making symmetric stepped pyramids. To get better definition of each layer, I moved to cutting asymmetrically. Effectively all of the cuts would share one side wall. This helped mitigate edge effects of the kerfs, allowing subsequent nested cuts to be closer in width without as much blending together.

One additional change in procedure was needed to help with getting good cut profiles. With the thin blade, for reasons unknown, the top of the cut profile deteriorated. About 50 um from the top, a wedge would be taken out of the cut. This originally caused a problem between the 20 and 40 μm layers. This was solved by reversing the order of those two cuts. As mentioned above, the cuts generally proceeded thickest to thinnest. This is the generally preferred method as it ensures symmetric cutting forces on the blade. By reversing the order of these two blades, though, the 40 um blade cut out the bad part of the 20 μm cut, eliminating the problem. This process does then put an asymmetric force on the 40 um blade as it cuts, causing extra wear on the blade, but I found that using a new 40 μm blade each cut meant that the blade help up reasonably well to the process, maintaining a satisfactory profile.

During the cutting process, it turned out the blade diameter was a few tens of microns less than specified, so 40 um in depth was taken out of the bottom layer while cutting in order to avoid the blade hub brushing the top pillars. There was also a minor issue with misalignment of one clearing pass, which meant the silicon wasn't cut properly. A second pass fixed the problem (See Figure 3.10). Other than that, the cutting was a success. The yield was significantly worse than for our other coatings, as the final pillar was 100 um wide, but only one pillar broke per thousand. I have modeled the difference of one in six pillars broken and found it to be within tolerance. The measured reflection is plotted in Figure

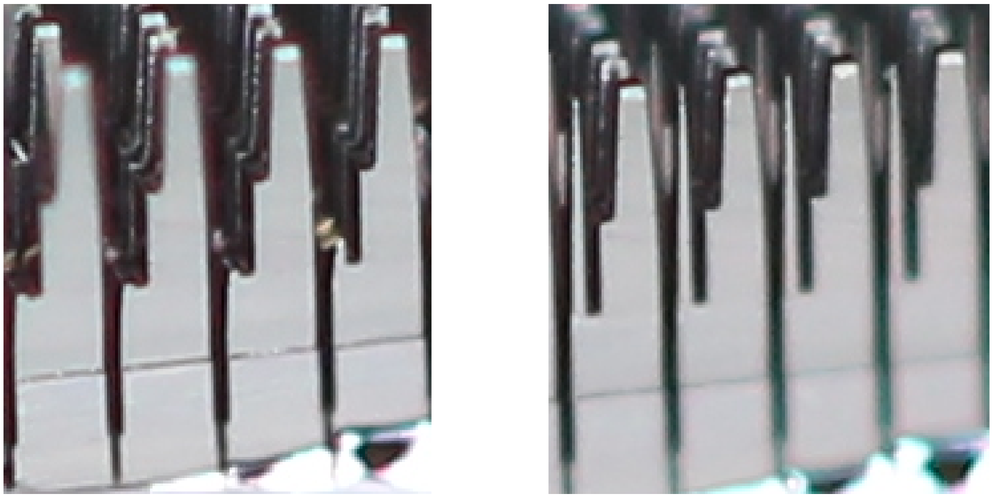

Figure 3.10: Pictures of the 5-layer AR coating I fabricated. On the left, there was a minor misalignment of one of the clearing cuts, leaving behind a spine. Shifting the cut by 30 μm cleared the spine more efficiently, as seen on the right.

3.11. Again it shows excellent agreement with the theory.

While this clearly demonstrates our ability to create a five-layer coating, I do not believe it is useful. While the pitch and kerfs of the cuts could be tuned better, our system is still strictly limited to the total depth that we've assumed here. Going instead to a four-layer, with the same depth limitation, actually allows the layers to be more finely tuned and achieves a similar performance with fewer layers. A comparison between four- and five-layer coatings is shown in Figure 3.11. I believe we should limit our fabrication to a max of four layers. Even then, the three-layer should usually suffice.

3.7.4 THz Coating

Pushing the limits of how high a frequency our system can get to, I designed a THz coating. The design used a 12 μm blade, the absolute thinnest blade available for our system. The model is shown in Figure 3.12. This coating was cut into both sides of a one-inch float-zone silicon wafer. No new process development was needed for this fabrication, although the tolerances were very tight. A micron in variation of the depth can lead to tens of GHz shift in the optimal band. As our system has tolerance of a few microns, this effectively smeared out our performance somewhat.

We don't have a measurement system capable of going to THz in our lab, so I sent the sample out to NASA Goddard, where it was measured using their FTS measurement system. The data taken is shown in Figure 3.13.

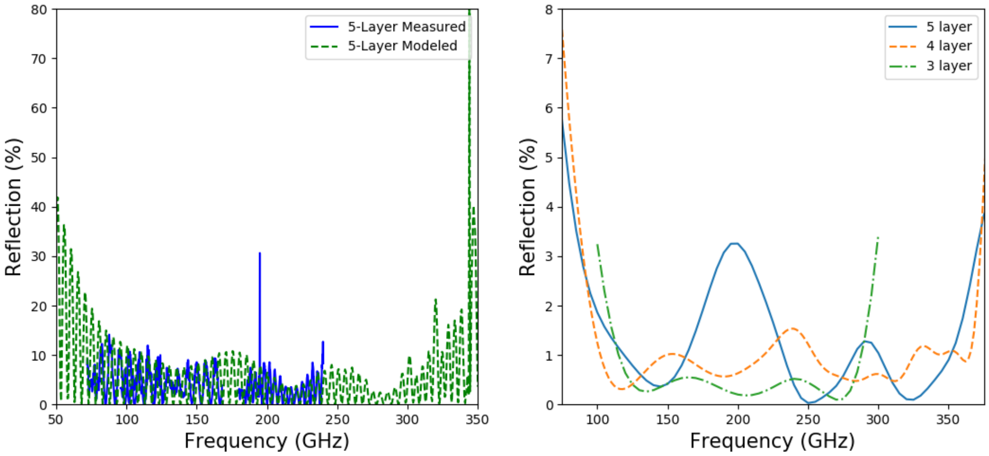

Figure 3.11: (Left) Comparison of measured and modeled reflection from a two-sided five-layer AR coating. The model is matched very well by the measured performance, though the performance is not of the highest quality. (Right) Comparison of modeled four- and five-layer coatings. Factoring in the limitations of our system, primarily the limit on depth-to-kerf, the five-layer does not significantly outperform the four-layer. Based on this I suggest that we don't fabricate any more five-layer AR coatings in the future.

3.8 System Limitations

Putting this together, I have effectively explored the operational phase space of our AR coating system. The THz coating could be pushed to a slightly higher frequency, around 2.5 THz. But we cannot make a two-layer coating that at that high of a frequency. With 12 μm blade for the bottom layer, the second layer would need to be approximately double the width. This will increase the size of the pitch as a function of number of layers. An approximate bandwidth-to-max-frequency plot is shown in Figure 3.14.

For future coatings, one should carry out a multidimensional analysis, where adding more layers might improve bandwidth but degrade performance. While ACT uses dichroic detectors, where a three layer AR coating is sufficient, other experiments have gone to trichoric (such as SPT 3G [47]) or broadband phase arrays [48], which might benefit from going to a four layer. As stated above, I don't think there will be a practical reason for ever going to a five-layer coating. The benefits do not generally outweigh the costs.

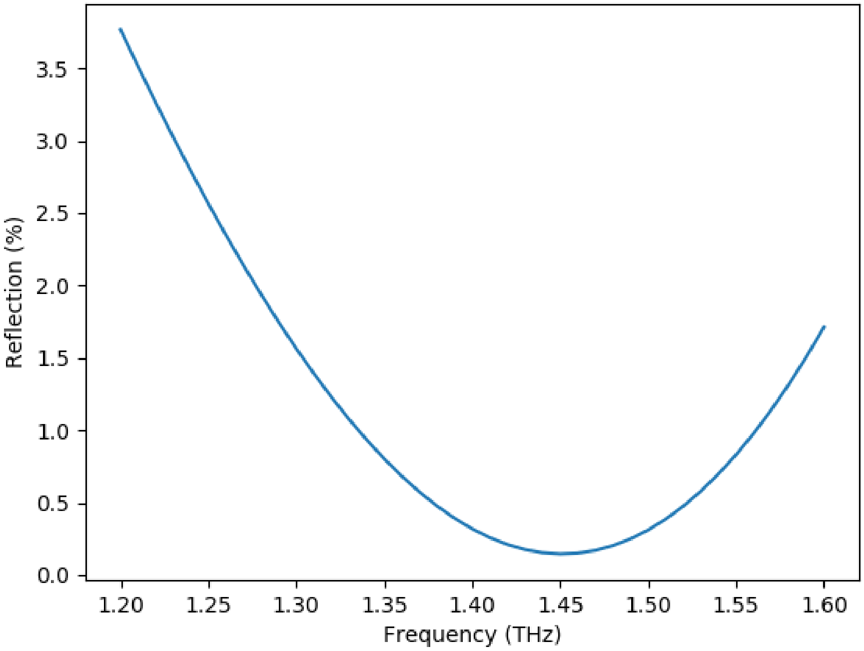

Figure 3.12: Modeled reflection performance of THz coating. This modeling is done via HFSS. The minimum reflection is around 0.3%. This is somewhat high for an AR coating, and it is caused by the tolerance of the fabrication system. This model is the nominal depth plus the estimated rms depth error of our system (2 μm). This slightly degrades the performance expected from the coating.

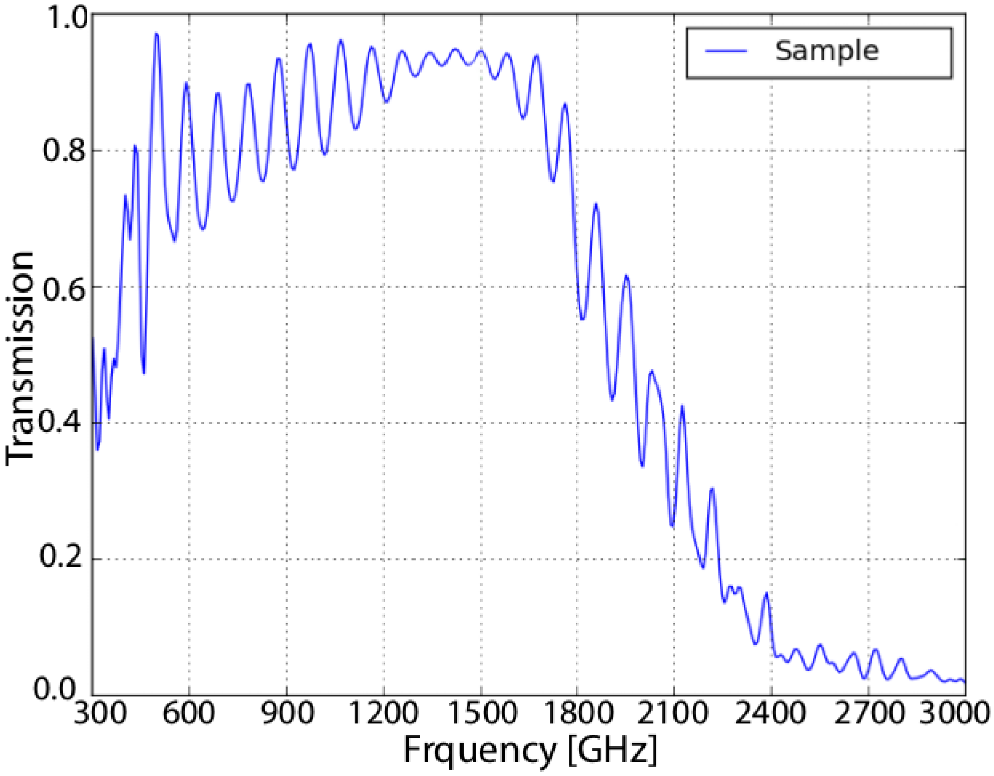

Figure 3.13: FTS transmission spectrum of two sided single-layer AR coated silicon wafer. The transmission peaks near 1.43 THz, near where the coating was optimized for. This data was taken at NASA Goddard using a mercury arc lamp source and 125 μm mylar beam splitter FTS.

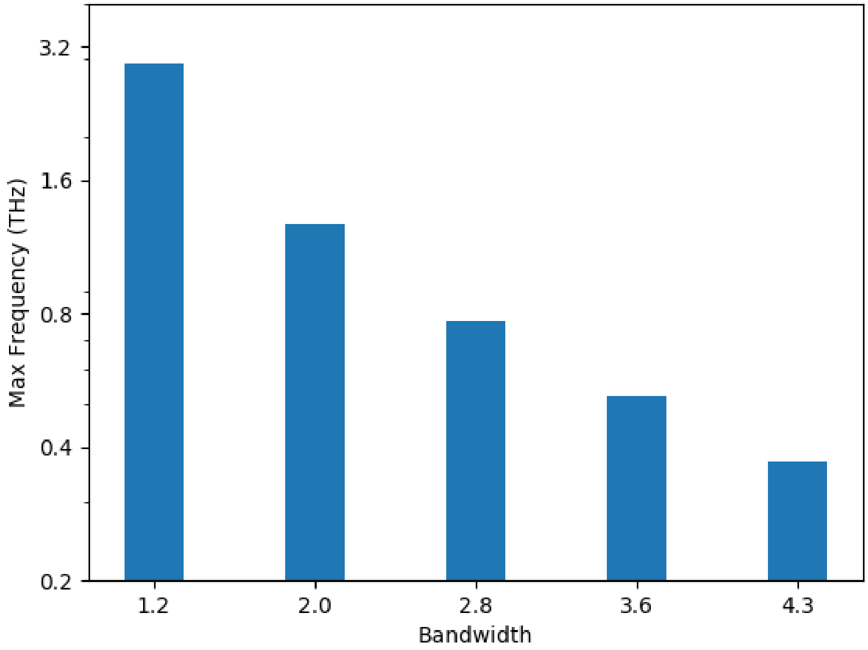

Figure 3.14: Plot showing maximum bandwidth against maximum frequency for AR coatings using our technology. The five bars represent 1-5 layer coatings. A single layer coating (1.2 bandwidth) can operate up into the THz frequency, but the five layer (bandwidth of 4.3) can only go up to about 500 GHz. This is limited by the saw blades we use for fabrication. The absolute thinnest blade that can be fitted to our saw is 12 μm thick. That sets the upper limit in frequency on single layer coatings. For multilayer coatings, the limit is set both by the available blades and the ability to distinguish between subsequent layers. For example, for a two layer, the second layer blade will be around 30 μm wide at minimum. This necessitates the pitch of the cuts to nearly double, which is why the maximum frequency nearly halves.

Chapter 4

Half-Wave Plates

Potential discovery of Primordial Gravitational Waves (PGW) is an exciting science goal of CMB observations. The PGW may leave a very weak (1 part in 10^7 or less) imprint on the large angular scale B-mode polarization power spectrum. The detection of this signal would be an enormous step forward for our understanding of the early Universe, and perhaps the first indication of quantum gravitational effects. Measuring these large angular scales requires control of $1/f$ noise. In an attempt to recover those modes, I developed ambient temperature continuously rotating half-wave plates (HWPs). This technology has the potential to transform observations of the CMB, and I deployed these HWPs on ACTPol to demonstrate their performance and the extend the ACTPol capabilities to include large angular scale measurements.

4.1 $1/f$ Noise

$1/f$ noise, also called low-frequency or pink noise, is the general the of noise that gets larger at longer time scales, corresponding to lower frequencies. This noise shows up everywhere, from electronics to biological systems. This can be seen in the power spectrum of our data time stream. At high frequency, our time streams reach the so-called white noise floor. At low frequency we start to see an upturn in the noise. This intersection point where the dominant noise source changes is called our $1/f$ knee. For our instrument, this is approximately at 3 Hz. Given our scan speed of 1.5° per second, this puts our $1/f$ dominated region above 0.5 degree. Unfortunately, the B-mode PGW signal peaks at 2 degrees, well into the $1/f$ dominated region.

There are many sources of this sort of noise, present in electronics and environmental factors. The general idea is that as more time elapses between two measurements, the more drift occurs, thus an increase in noise at low frequency. For the CMB observations, the

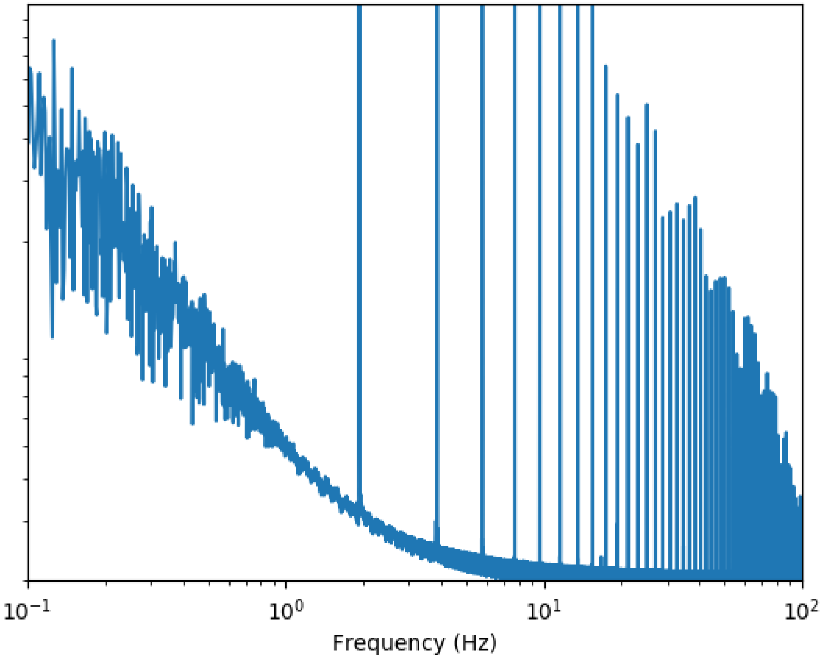

Figure 4.1: Log-log plot of noise spectrum of our data. This is averaged over all detectors for a single TOD. The spikes in the data come from the the harmonics of the HWP rotation frequency, the first coming in at just under 2 Hz. The deviation from white noise is clearly seen, starting around 3 Hz.

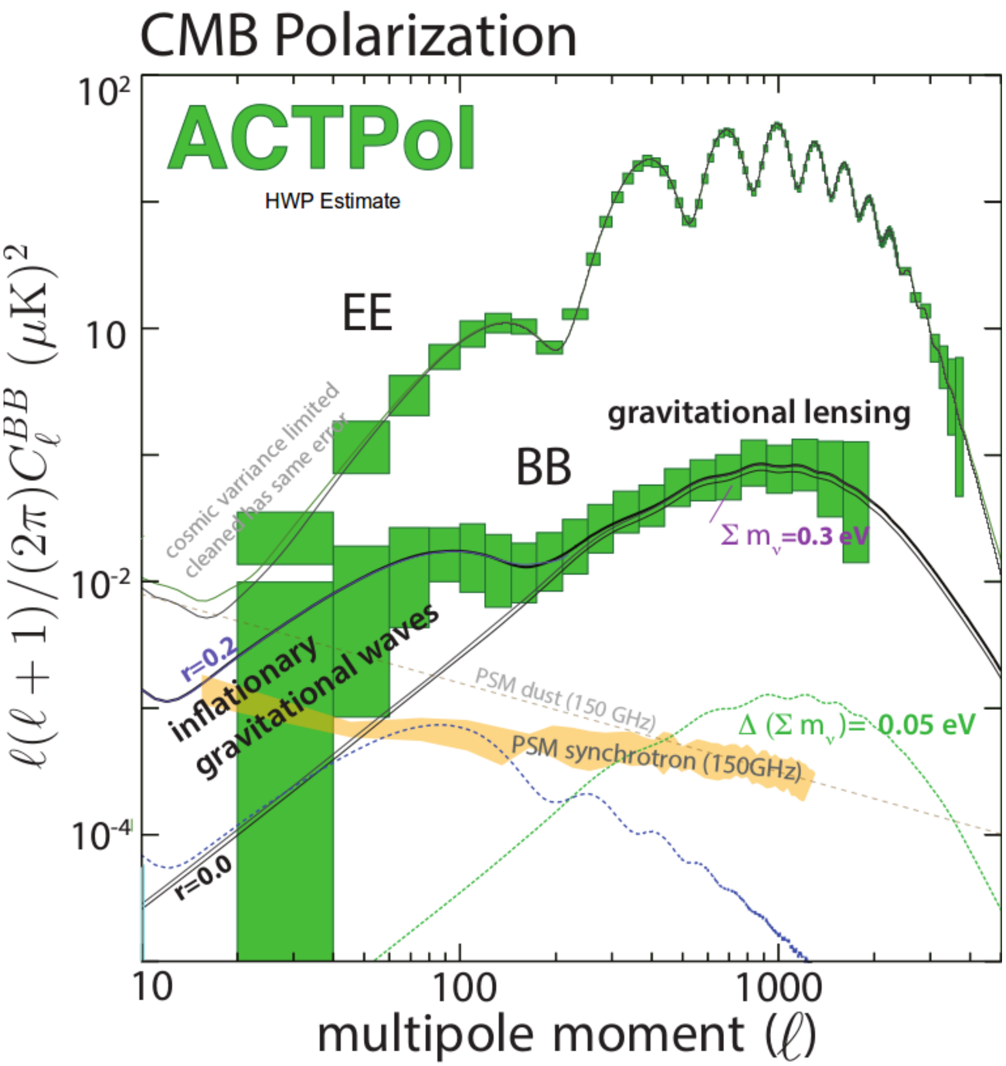

Figure 4.2: CMB EE and BB polarization power spectra. The green bins show the errors expected from ACTPol without $1/f$ noise present in the system, and assuming $r = 0.2$.

larges contributions are from two atmospheric effects. First, the atmosphere is patchy. As we slew the telescope, we are looking through different columns of air, with different density and temperature profiles. Second, the atmosphere is turbulent. Even if we didn't move the telescope, the air column we look through would be changing on relevant timescales. Eliminating, or at least mitigating, this source of noise would dramatically improve ACT's large angular scale measurements. Figure 4.2 shows a projection of ACTPol's polarization power spectra with $r = 0.2$ and no $1/f$ noise. In this case, the primordial gravitational wave signal would be easily identified.

There are several methods for dealing with this noise. Satellite and balloon experiments send a telescope above all or most of the atmosphere, eliminating the atmosphere as a noise source, dramatically reducing the $1/f$ noise. These experiments are significantly more expensive, limiting the primary aperture of the telescopes and sacrificing science from small angular scales. The method which we purse here is to modulate the incident polarization, shifting the large angular scale signal to a higher frequency, above the $1/f$ knee. There are various methods for accomplishing this modulation. The method I pursued for the Advanced ACTPol instrument was using a warm, continuously rotating HWP.

4.2 HWP Overview

HWPs are plates of birefringent (orthogonal axes have different indicies of refraction) material cut to a particular thickness, such that the optical path length difference of the two polarizations is equal to a half-wave length at a particular frequency. This serves to flip incident polarization about the so-called fast axis on the plate. By rotating a HWP in front of our optics, this effectively induces a modulation of the polarized signal.

A common way of modeling a HWP is using what are called Muller Matrices. In this formalism, each optical element is represented by a matrix, which operates on a vector of Stokes Parameters. Stokes Parameters represent the full polarization state of light with four parameters, given as

$$I = |E_x|^2 + |E_y|^2 \tag{4.1}$$

$$Q = |E_x|^2 - |E_y|^2 \tag{4.2}$$

$$U = 2 * Re(E_x \cdot E_y^*) \tag{4.3}$$

$$V = -2 * Im(E_x \cdot E_y^*) \tag{4.4}$$

I is the intensity, and Q and U quantify the linear polarization. V quantifies the circular polarization. Pure Q, U and V polarizations are shown in Figure 4.3.

For 100% polarized light($Q^2 + U^2 + V^2 = I^2$), it can be convenient to think of the polarization state as a point on the surface of the Poincare sphere, where each axis is one of the Stokes polarization parameters. This sphere is depicted in Figure 4.4. Changing the polarization state (such as passing through a retarder) can be visualized as moves across the surface of the sphere.

For working with Muller Calculus, we define the Stokes vector S as

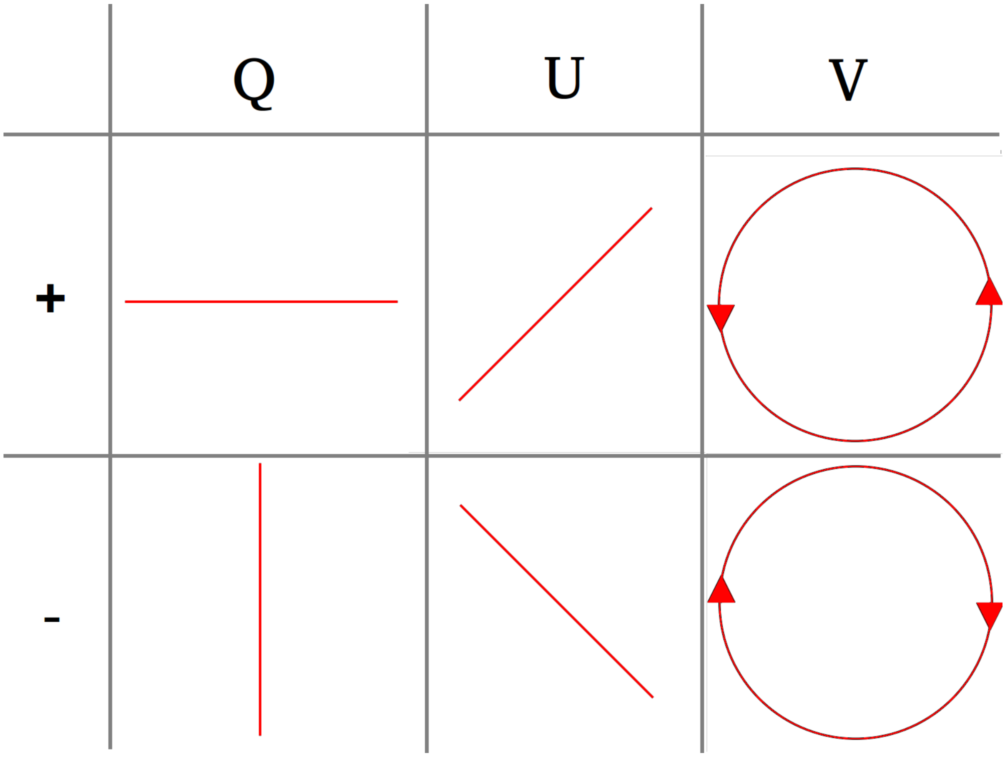

Figure 4.3: This shows the orientation of the electric field for fully polarized light in each of the Stokes Parameters. Stokes Q and U define the linear polarization of light, and Stokes V gives the ellipticity and handedness of the polarization. Polarized light can have a combination of these parameters satisfying $Q^2 + U^2 + V^2 \leq I^2$, with the inequality as equal for fully polarized light.

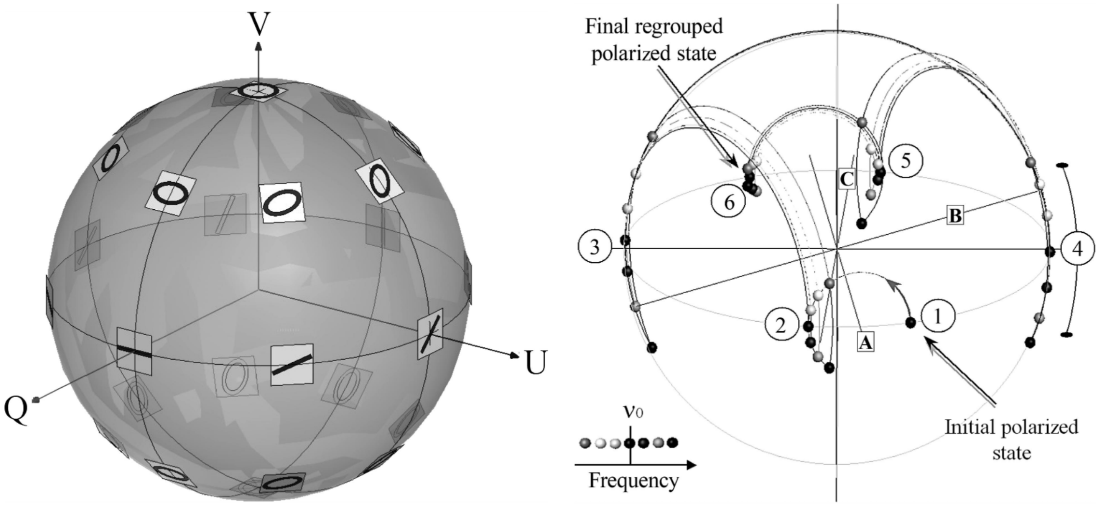

Figure 4.4: Left: Poincare sphere, where the polarization of pure polarized light can be described by any point on the surface. Right: A stack of several HWPs at rotated angles can be used to create a broadband HWP. This plot shows that by making a series of moves across the surface of the Poincare sphere, several frequencies can be regrouped on the opposite side of the surface. This Figure was taken from [11].

$$S = \begin{bmatrix} I \\ Q \\ U \\ V \end{bmatrix} \tag{4.5}$$

The Muller Matrix for a retarder (including HWPs) is

$$\Gamma = \begin{bmatrix} 1 & 0 & 0 & 0 \\ 0 & 1 & 0 & 0 \\ 0 & 0 & \cos(\Delta\delta) & -\sin(\Delta\delta) \\ 0 & 0 & \sin(\Delta\delta) & \cos(\Delta\delta) \end{bmatrix} \tag{4.6}$$

Assuming no dispersion (index of refraction constant in frequency), the phase delay of a retarder is given by

$$\Delta\delta = \frac{2\pi d(n_e - n_o)}{\lambda} \tag{4.7}$$

where n_e and n_o are the indicies for the extraordinary and ordinary axes respectively, λ is the wavelength of light, and d is the thickness of the plate. For a half-wave plate, $\Delta\delta = \pi$.

To model the polarization modulation (and broadband HWPs later), we also need a

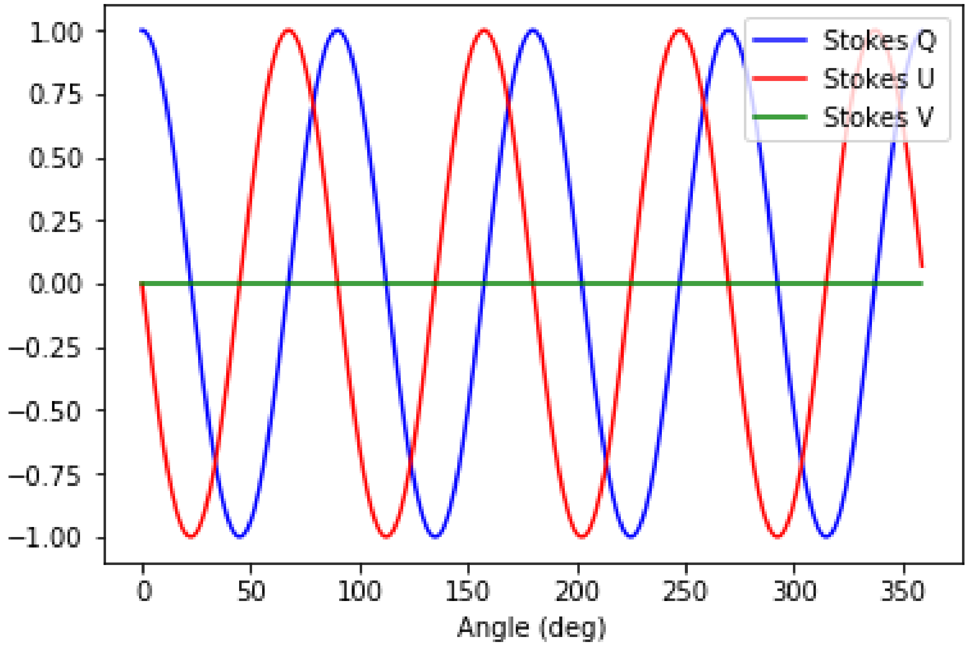

Figure 4.5: The plot above shows the output Stokes Q, U and V (Input of $Q = 1$, $V = U = 0$), as the HWP is rotated from 0° to 360°. The Q and U output vary at four times the HWP rotation frequency ($4f$). The factor of four comes from two distinct contributions. One, as seen in Figure 4.3, polarization is not a true vector, but a pseudovector. It has an orientation, not a direction, so rotating 180° is the same as not rotating it. This gives one factor of two. The other factor of two comes from the HWP rotating the polarization as 2χ, where χ is the angle between the HWP fast axis and the polarization angle. These two factors give us the factor of 4.

rotation matrix, given by

$$R(\phi) = \begin{bmatrix} 1 & 0 & 0 & 0 \\ 0 & \cos(2\phi) & -\sin(2\phi) & 0 \\ 0 & \sin(2\phi) & \cos(2\phi) & 0 \\ 0 & 0 & 0 & 1 \end{bmatrix} \tag{4.8}$$

The rotation matrix just rotates Q and U by 2ϕ, while leaving I and V alone, as one would expect. To model polarization modulation, we take the product

$$S_{out} = R(-\phi) * \Gamma(\Delta\delta) R(\phi) * S_{in} \tag{4.9}$$

as ϕ rotates through a full rotation. Figure 4.5 shows the modulation of Stokes Q, U and V for a HWP at its nominal frequency (in this case at 120 GHz).

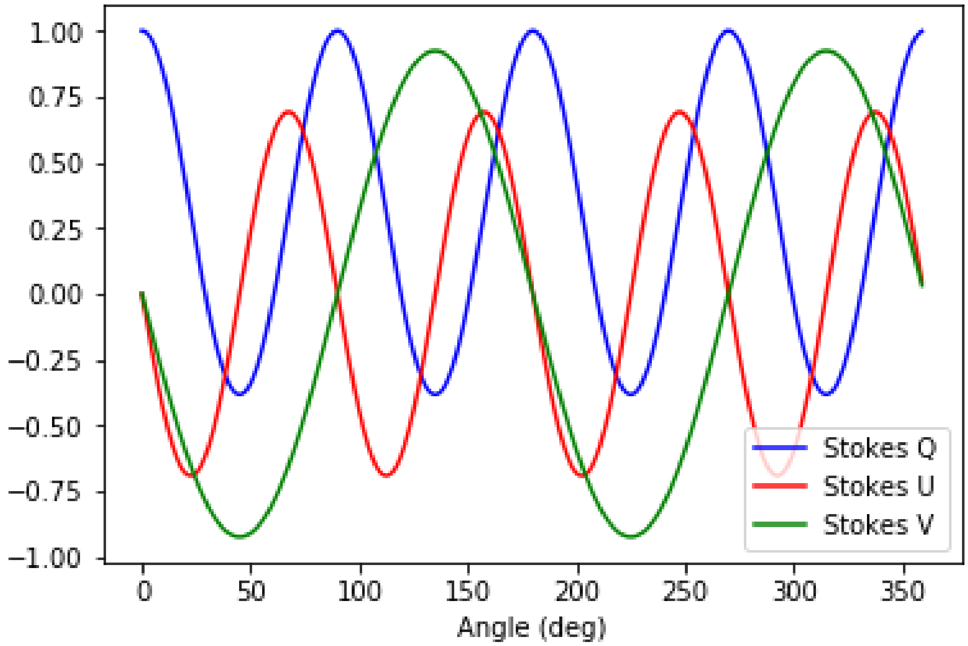

Figure 4.6: Output Stokes Q, U and V (Input of $Q = 1$, $V = U = 0$), as the HWP is rotated from 0° to 360° for a frequency away from the nominal HWP frequency. Note the significantly reduced modulation for Q and U, and a significant increase in V. In fact, this HWP acts as nearly a quarter-wave plate at this frequency. It is interesting to note that Stokes V is modulated at $2f$ while Q and U are modulated at $4f$ for a Q polarized input.

As can be seen from the definition, the phase delay is dependent upon the frequency. As we move away from the nominal frequency, the phase delay moves away from 180°. This then means that some linear polarization bleeds into circular polarization. Figure 4.6 shows the modulation of the Stokes Parameters of 70 GHz light going through a 120 GHz HWP. As can be seen, there is a significant component going into V, which is effectively lost for most detectors (including ACT's).

In order to make HWPs broadband, we need to play some clever games. There are two main ways to make this happen. The first is primarily for optical band HWPs; the idea is to take two materials whose indicies have different frequency dependencies, and stack them so their fast axes are crossed. This method is problematic at millimeter wavelengths for a few reasons. The first is it requires at least two suitable materials for HWPs, and in millimeter range we just have sapphire. The second (more pressing) reason is that the thickness of these stacks ends up being many times the wavelength of light. A commercially available broadband HWP for 465-610 nm light is 8 mm thick. Scaling this to mm wavelengths is not feasible.

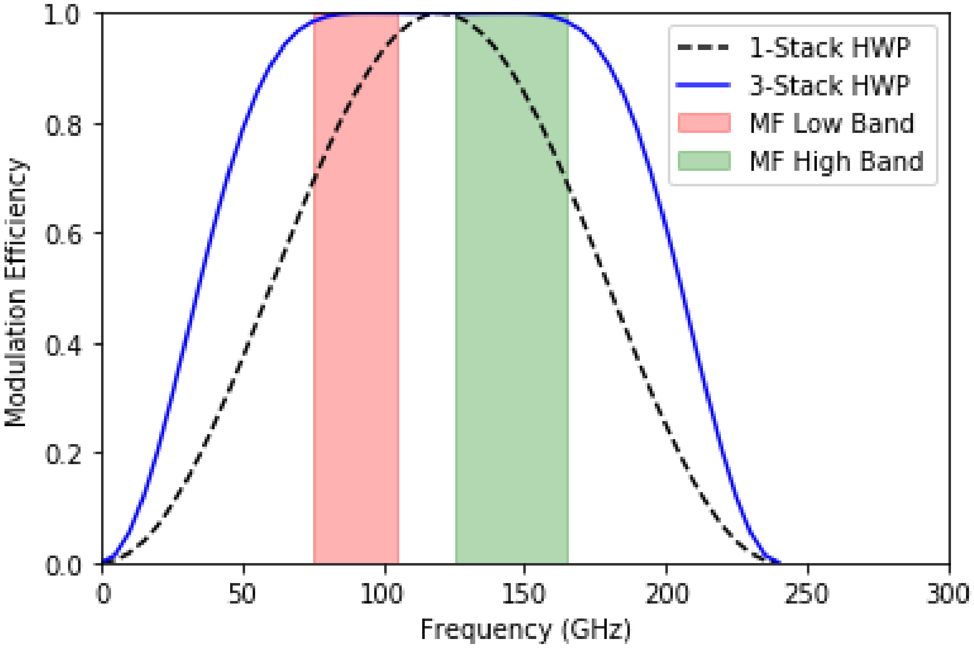

Figure 4.7: Modulation efficiency of a 1-stack and three-stack HWPs as a function of frequency, along with the Advanced ACTPol MF bands. As can be seen, the required bandwidth is too large for a single HWP, but a three stack HWP nicely covers the low and high bands with a modulation efficiency near 100%.

The second approach is to use a Pancharatnam geometry. This method uses a series of HWP of the same material, with their fast axes rotated relative to one another. This has the effect of making a series of moves across the Poincare sphere, allowing several frequencies to be regrouped. This is shown schematically in Figure 4.4

This can be modeled using the above Muller Calculus. Using a rotation angle of 58 degrees [49] for the central HWP, a three-stack HWP can effectively modulate a wider bandwidth. A comparison of a one- and three- stack HWP is shown if Figure 4.7. Clearly, a three stack HWP is sufficient for Advanced ACTPol's dichroic detectors.

By adding more plates to the stack, more frequencies can be regrouped. For our dichroic detectors, we use a three stack geometry (as will POLARBEAR). EBEX had trichroic detectors and used a five-stack geometry. LiteBird will have a tiled focal plane, and has constructed a nine-stack HWP.

While the Pancharatnam geometry is useful, there are a few caveats with its implementation. For one, there is no longer universally defined fast/slow axes. Instead, the effective fast axis varies somewhat as a function of frequency. Figure 4.8 show that the effect can be up to tens of degrees (seen as a phase shift the the Q modulation).

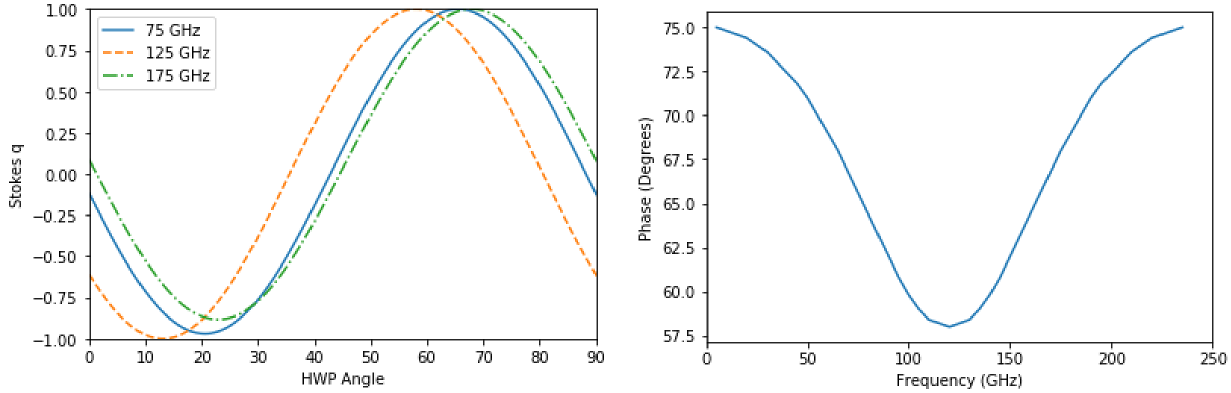

Figure 4.8: Phase shifts at different frequencies from three stack HWP. (Left) Normalized Stokes q parameter as the HWP is rotated from 0° to 90°. (Right) Phase for q parameter as a function of frequency. As can be seen the phase of the q modulation varies significantly as a function of the frequency. This can be somewhat problematic as q is rotated by a slightly different angle at each frequency. This will smear out our signal.

4.3 Birefringent Metamaterials

Several experiments (EBEX [50], ABS [42]) had deployed such technology and demonstrated its utility, or will in the near future (Litebird [51], POLARBEAR [52]). What is different about my HWP is the material. All of these other experiments use alpha-cut sapphire as their birefringent material. The HWPs I fabricated for ACT used metamaterial silicon technology.

In Chapter 3, the AR coatings using silicon metamaterial were always symmetric under 90° rotations. This four-fold symmetry ensures there is no cross polarization leakage (at normal incidence). If, however, we break this symmetry, we induce birefringence. This can be done in a few ways. We can cut with different kerfs in each direction, we can cut with a different pitch in each direction, or we can cut in just one direction.

To define the indicies of the birefringent layer, I first had to run some simulations to test how birefringent these layers would (or could) be. To do this, I made an HFSS model of a single layer of cut silicon surrounded by vacuum. The reflection at normal incicence for orthogonal polarizations for a 3 mm slab is shown in Figure 4.9. Following Equation 3.2, the peak reflection for a single layer surrounded by vacuum is

$$R_{max} = \left(\frac{n_2^2 - 1}{n_2^2 + 1}\right)^2 \tag{4.10}$$

This allows us to easily measure the indicies of refraction for each orientation. By varying the pitch and width of the cuts, I explored the possible phase space of how birefringent

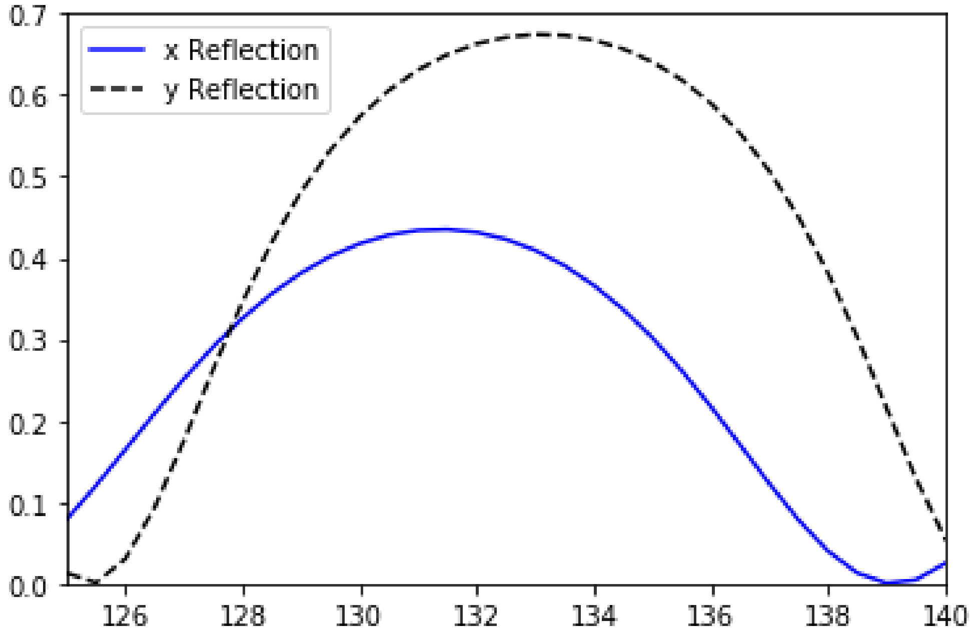

Figure 4.9: HFSS modeled reflection off the x and y axes of birefringent silicon. The change in maximum reflection can be used to measure the change in index. The change in frequency of the maximum frequency is dependent upon the thickness of the silicon layer.

these materials can be. I found that birefringence between $0.6 < n_{slow} - n_{fast} < 1.4$ is consistent with practical fabrication constraints. This method is used to create the half-wave and quarter-wave plate layers in silicon. If, however, cuts are made asymmetrically in both directions, we can create effectively arbitrarily small birefringence. This latter method is used to make birefringent AR coatings for the HWPs. To my knowledge, this is the only demonstration of birefringent AR coating at these wavelengths. This is useful as for birefringent materials, the AR coating index had to be a compromise between the ordinary and extraordinary indicies. No such compromise is needed in my designs.

4.4 Overview of HWPs Developed

4.5 ACTPol 150 GHz HWP

The first HWP I made was for the ACTPol 150 GHz single frequency array. Since this was not a dichroic array, I adopted a simple HWP geometry, without employing the tricks to make broadband HWPs. It served as a proof of principle, testing our new technology.

4.5.1 Design

The HWP was made out of a single plate of silicon. Into each side I cut a quarter-wave plate with a two layer AR coating. A central layer of interstitial silicon provided the mechanical stability.

Mechanical stability is a major constraint for this design. If we fabricated an optimal HWP, it would consist of 100 μm wide strips of silicon suspended in free space. Such a design is impractical, as it would vibrate and degrade in any practial solution. To avoid this problem, I went with a simpler design consisting of: (1) an AR coating, (2) a quarter-wave plate, (3) solid silicon, (4) a second quarter-wave plate aligned with the first, and (5) a second AR coating. The central silicon layer provides structural integrity. Additionally, the thickness of the layer can be tuned to mitigate reflections.

After cutting, a ring of Invar (a nickel-iron alloy with a coefficient of thermal expansion similar to silicon) was glued around the edge of the plate. Invar was chosen so that if later this plate was used in a cryogenic system, there will be minimal thermal expansion mismatch. This ring allowed us to handle the plate without touching the silicon surface. It also provided a clamping surface for deployment on the telescope.

To design the HWP, I had to tune the indicies of each orientation of each AR layer, and the thickness of the two AR layers and the interstitial silicon layer (seven free parameters). This process would fix the birefringence and thickness of the quarter-wave plate layers to predefined values (mentioned above).

This initial design was then ported to HFSS. To completely tune the parameters, a full two-sided HWP model was constructed in HFSS. This differed from the AR coating work where only one side was needed for optimization. This had the benefits of fully modeling the plate, but the drawback of taking twice as long to run. An isometric view of the model is shown in Figure 4.10. HFSS was properly able to calculate the relative phases of the two orthogonal orientations. This phase delay was held near 180° during optimization.

4.5.2 Fabrication

The fabrication of the 150 GHz HWP needed a few process development steps worked out. Previous work mounting flat wafers involved using a wax called WaferGrip to hold the silicon directly onto the mounting plate. This wax is a very lossy material and difficult to fully clean out of the metamaterial structure. After discovering this fact empirically, I designed a vacuum chuck to eliminate this issue.

A picture of the vacuum chuck is shown in Figure 4.11. The series of concentric circles each have a hole drilled to the vacuum port on the chuck. These are threaded holes that can

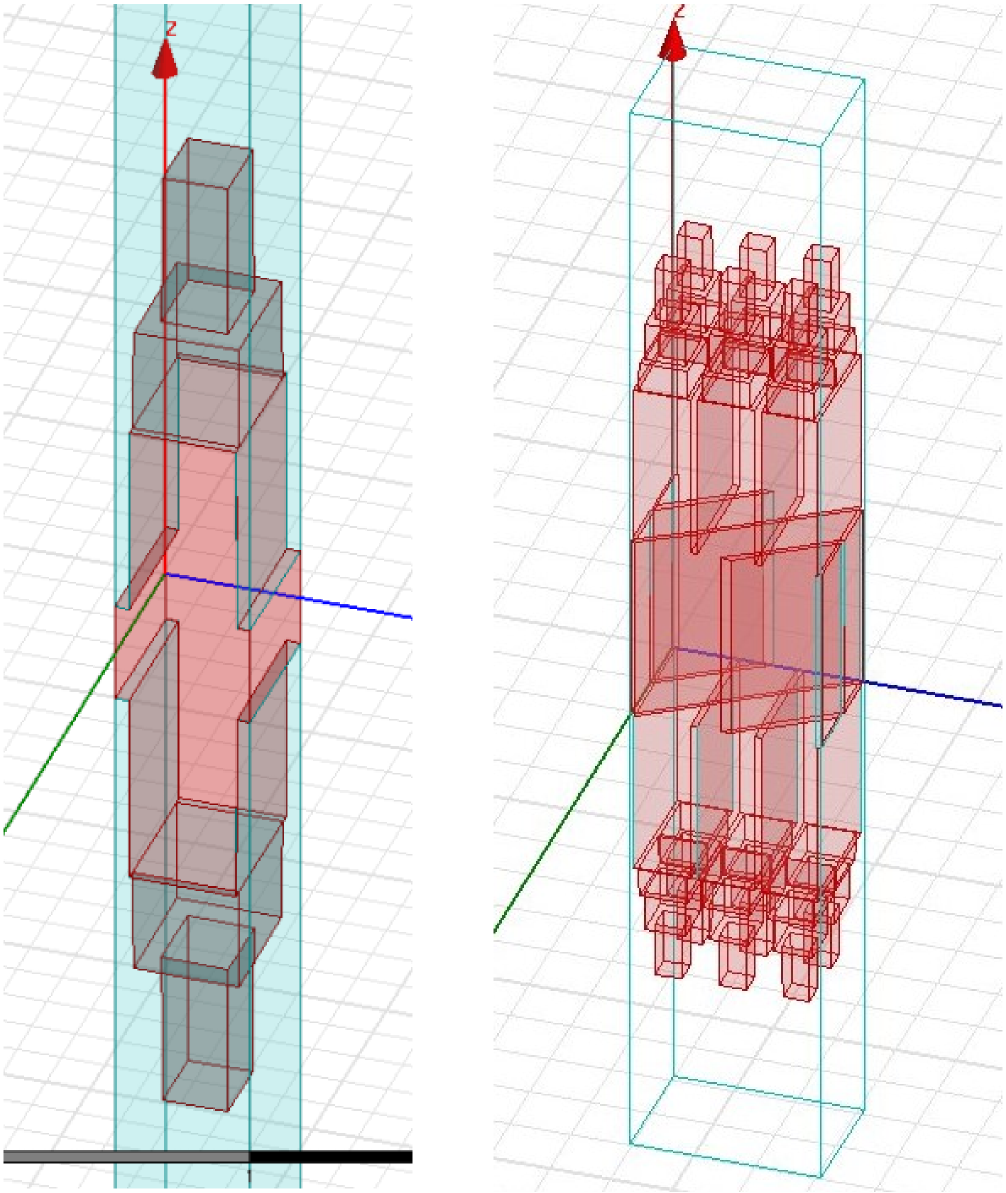

Figure 4.10: Isometric views of HFSS models for the single frequency (left) and broadband (right) HWPs.

be sealed off to allow for varying sizes of wafers, from 2 inches to 13 inches. The vacuum used was a three stage venturi pump, running off our air compressor. This pump was chosen since it had no moving parts and was resistant to water and silicon grit flowing through it, which takes place in our system.

One issue the vacuum chuck caused was a warping of a silicon plate. This HWP wafers are relatively thin (a few mm) with a large diameter (300 mm), making them flexible at the 20 μm level. With the vacuum chuck not being perfectly flat, and applying a strong and not completely uniform force across the wafers, there was significant warping, on the order of tens of microns. The primary mode was effectively a potato chip shape. To counter this effect, I measured the silicon surface, fit the data with the first four Fourier modes, and cut along the fit contours. This reduced the rms error from a few tens of microns to a few microns. A sample fit is shown in Figure 4.12.

An additional problem came when cutting the second side. As the face down side was no longer a smooth wafer, but a cut surface, the vacuum chuck couldn't hold it. To seal the edges, I used melted paraffin wax. Just as with the other wax, this is a lossy material, but it was only applied on the edge, outside of the illuminated area of the HWP, so it would not impair performance.

The cutting itself was effectively the same as for lenses, except for the asymmetry. The yield was likewise nearly perfect with two pillars total being broken (out of over a million pillars). After cutting, I used a large ultrasonic cleaner to get the silicon dust out of the grooves.

4.5.3 Testing

The reflection was measured for orthogonal orientations using the previously described reflectometer. The data was taken was in TM mode set up at 10° angle of incident. The data are shown in Figure 4.13. The reflection is well matched to the HFSS model.

The modulation efficiency of the HWP was measured at NASA Goddard, using their Vector Network Analyzer (VNA) and a quasi-optical setup. VNAs are measurement systems that measure the amplitudes and phases of the scattering- or s-parameters of an electrical network. In this case, the s-parameters measured are the reflection and transmission of our HWP system.

The quasioptical setup used is shown in Figure 4.14. A feed horn is placed at one focus of an off-axis elliptical mirror. The HWP is placed at the second focus. A second elliptical mirror collects the light and directs it at the receiver feed.

For this measurement, the frequency is swept from 140 GHz to 180 GHz. After each

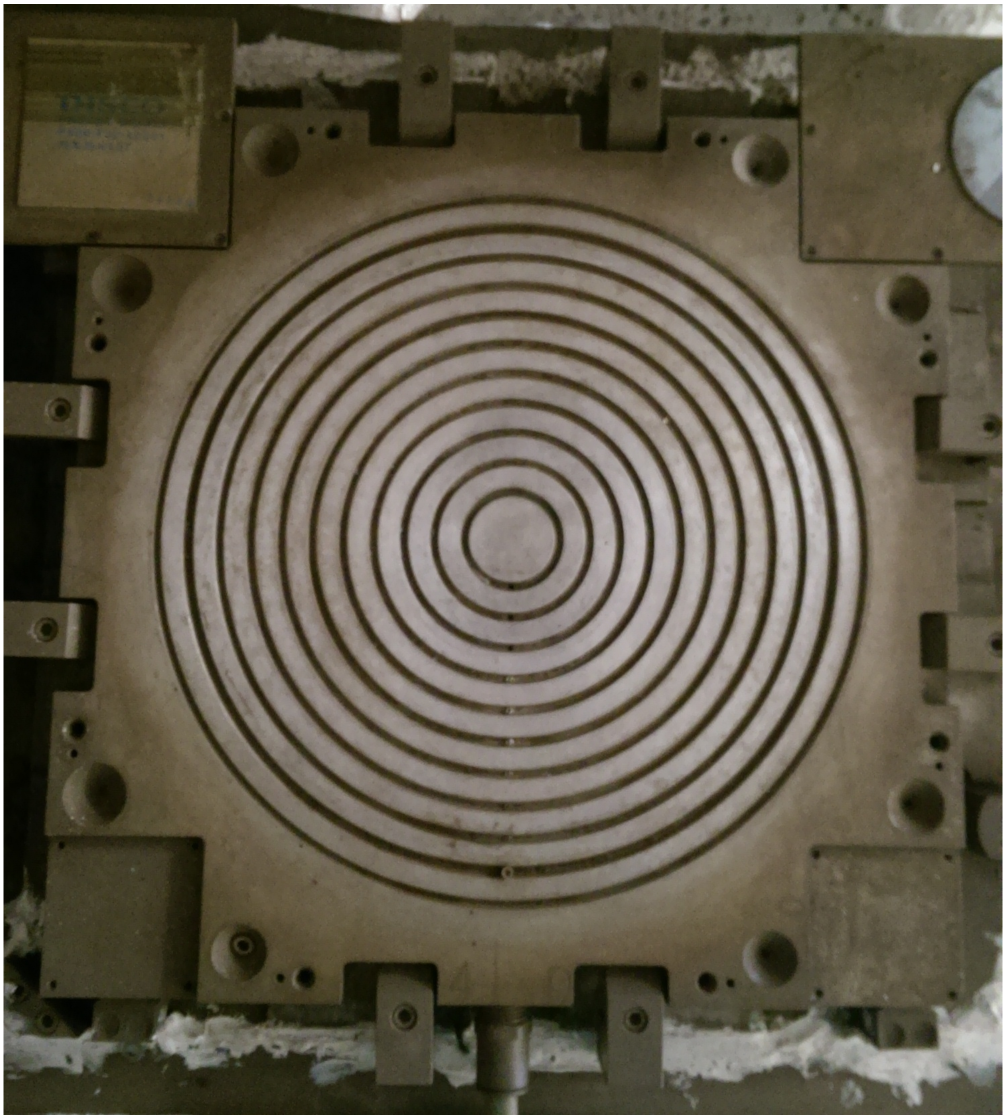

Figure 4.11: Vacuum chuck I designed for HWP fabrication. Vacuum is pulled through the connection at the bottom of the picture. This leads to a hollowed chamber running to the center of the chuck. The concentric rings are cut with a 'V' profile to a maximum depth of 2.8 mm. Each ring can be individually connected to the vacuum chamber, allowing the vacuum chuck to hold plates from 13 in down to 2 in.

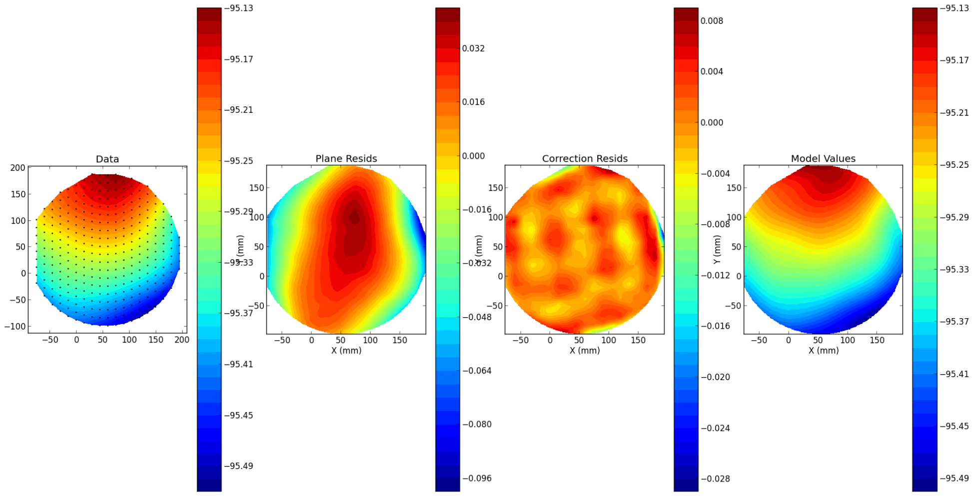

Figure 4.12: Modeling the surface of a silicon wafer for HWP fabrication. From left to right, the raw data, residuals for a plane fit, residuals for the Fourier fit, the model values. As can be seen, fitting a plane to the wafer leaves potato chip shaped residuals on the order of 50 μm. For the tolerances of the HWPs, this was unacceptable. With fitting the first few Fourier modes, the residuals over most of the plate are less than 5 μm, which is within our tolerance. The fit gets bad near the edge, as is common with Fourier fits.

frequency sweep, the HWP is rotated 11.25 degrees, and the measurement is repeated. After the HWP is rotated 180 degrees in total, the receiver horn is rotated. This is accomplished by replacing the straight wave guide connecting the feed to the source with one that is twisted. The twist is nominally 90 degrees, but I measured it to actually be 88 degrees. This has only a minimal impact on the measurement. With the twist in place, the measurement is then repeated. This allows us to completely sample Stokes Q. Normalizing by the total field we get normalized Stokes q (q = Q/I) as

$$q(\phi) = \frac{H(\phi) - fV(\phi)}{H(\phi) + fV(\phi)} \tag{4.11}$$

where H is the horizontal component of the field (horns aligned), V is the vertical component of the field (horns rotated), and f is the relative gain term, given by

$$f = \frac{\sum H(\phi)}{\sum V(\phi)} \tag{4.12}$$

For each frequency, Q and U vary at $4f$ as the HWP is rotated. Figure 4.15 shows how u is modulated at 150 GHz. The amplitude of the $4f$ component is the modulation efficiency. This is calculated for each frequency and is plotted in Figure 4.16. The figure shows that the modulation peaks near 99%, and averages ot 97% between 125 GHz and 165 GHz, and

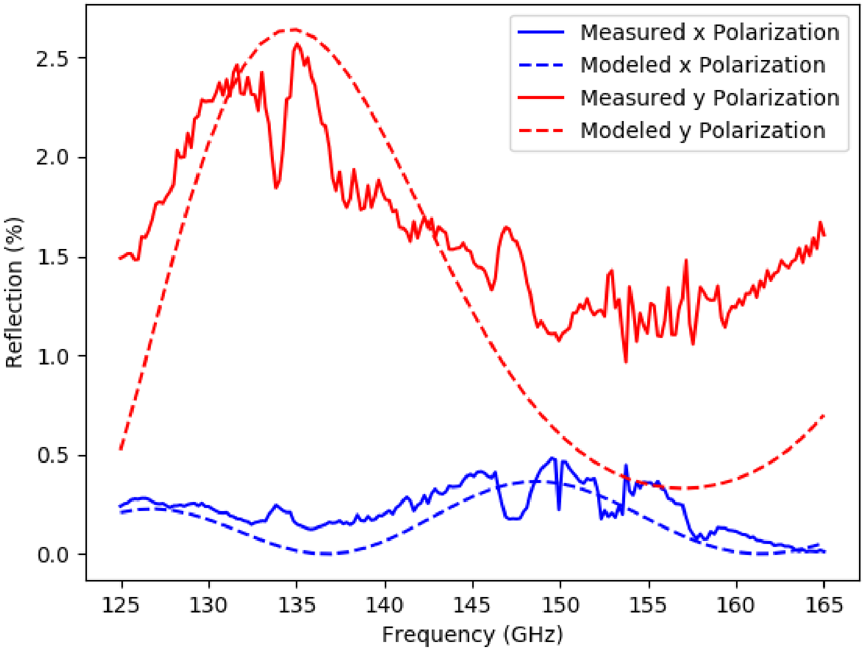

Figure 4.13: Reflection measurement of the x and y polarizations for a 150 GHz single-frequency HWP, measured by our reflectometer in lab. The data were taken at 10° angle of incident, with the radiation set to the TM mode.

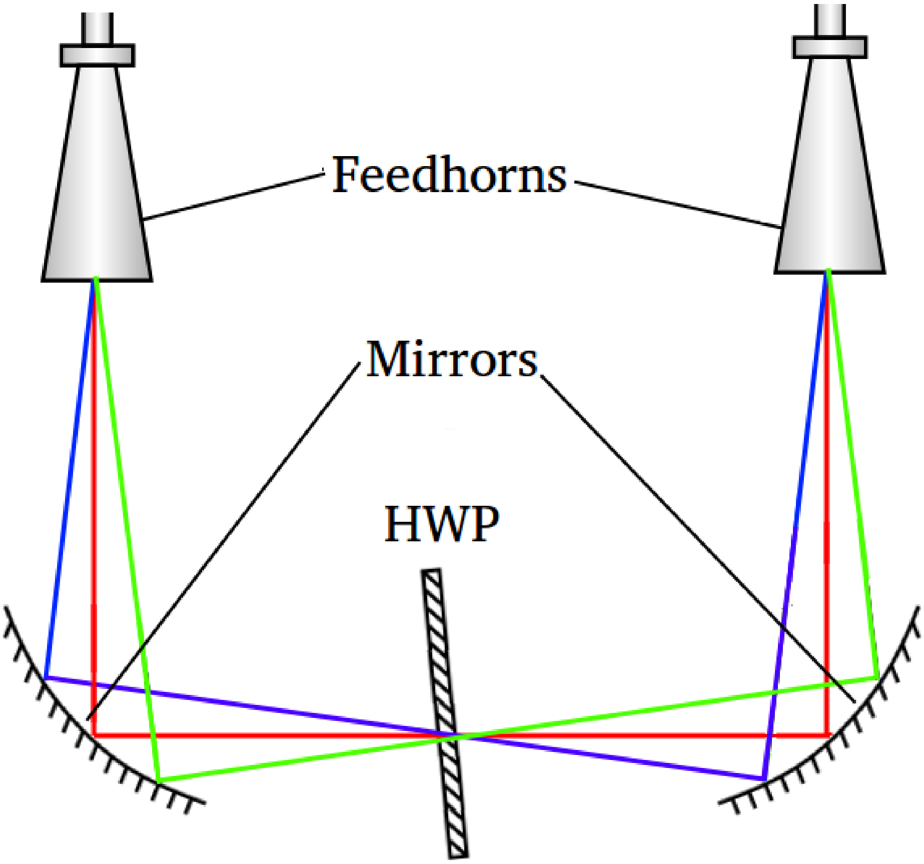

Figure 4.14: Diagram of quasioptical setup used to measure the modulation efficiency of the HWPs. Light is emitted from the horn on the left, and is focused by an elliptical mirror onto the HWP. A second elliptical mirror collects the light and redirects it to the horn on the right. The beam is focused on a small part (2 in) of the center of the HWP. The horns are connected to VNA extender modules to get the VNA to the frequency rang of interest. The HWP is slightly angled (≈ 10°) to effectively dump the reflected beam out of the optical path, cleaning up the transmission data.

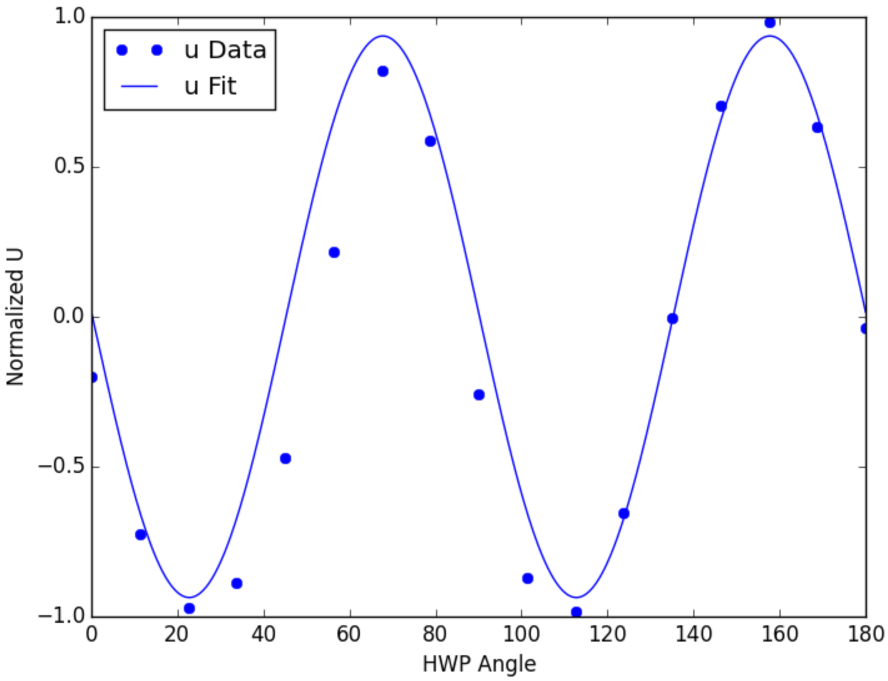

Figure 4.15: Data and fit for the modulation of normalized Stokes U for the single 150 GHz HWP at 150 GHz. The data were taken at NASA Goddard using their VNA setup. The fit is a simple least squares fit for a sine wave, fitting the mean, amplitude and phase. The modulation efficiency is given by the amplitude of the modulation. The modulation efficiency shown here is around 0.95.

is well matched by my numerical model.

4.5.4 Summary

The fabrication of this single frequency HWP was an important proof of principle, but unfortunately the two I fabricated will never be deployed. For the first one I fabricated, I did not check the quality of the silicon before-hand, and found that it was too lossy to be used at ambient temperature. The second one cracked during fabrication, due to the interstitial silicon being too thin. When we tried putting it on the telescope, the crack lead to significant scattering, severely impairing the measurement. For future experiments with a single frequency detectors, this HWP design would be a viable option, although the central silicon layer thickness would need to be increased for additional mechanical strength.

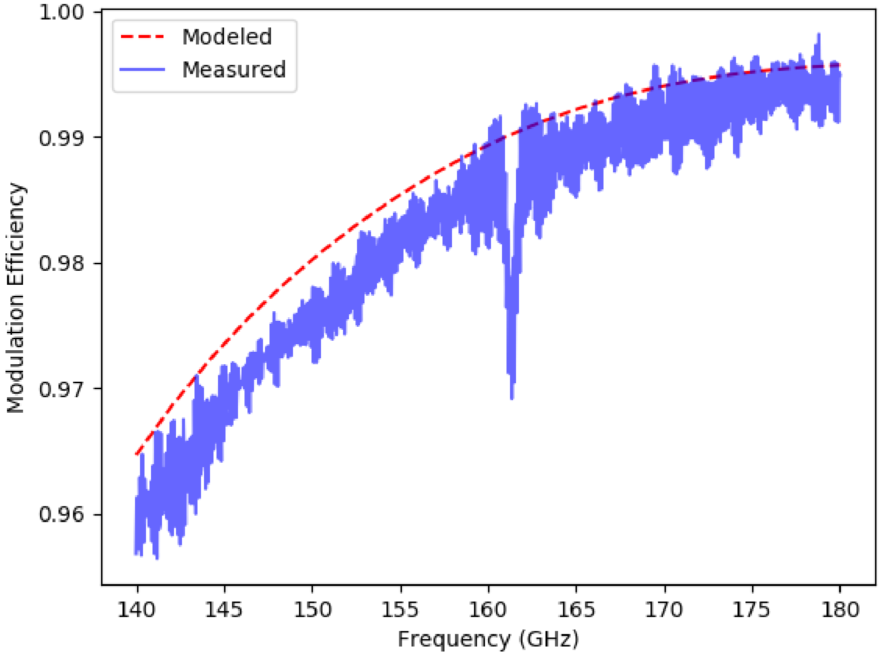

Figure 4.16: Modulation efficiency for the single HWP for ACTPols 150 GHz array. The central frequency of this HWP is shifted higher than originally designed due to the blade cutting a bit thinner (making HWP less birefringent than intended), but would still be sufficient for the actual band. When the thinner blade is accounted for in the model, the model is very well matched with the measurement. The dip at 162 GHz is likely a systematic present in our measurement system.

4.6 Advanced ACTPol Achromatic HWPs

4.6.1 Basic Design

As described in Section 4.5, stacking an odd number of HWPs together in specified geometries, one can make achromatic half-wave plates (AHWPs) that cover a broad range of frequencies. For the Advanced ACTPol dichroic detector arrays, a three-stack AHWP is needed to adequately cover the bands with a sufficiently high modulation efficiency (as shown in Figure 4.7). In order to make this geometry, I had to start with two separate pieces of silicon. I would cut the central, rotated HWP, then bond the two piecies of silicon together, and cut the outer HWP layers. Each orientation would also have a three-layer AR coating on top. I successfully made three such AHWPs, two for the MF detector arrays, and one for the HF array. The design, fabrication, and testing processes all followed the same basic steps as before, but significant work was needed at various steps to account for the increase in complexity.

4.6.2 Achromatic Metamaterial HWP Modeling

In order to model this geometry, a significant upgrade to my analytic modeling code was needed. For previous modeling of the single frequency HWP, the linear polarizations of light were handled completely separately. With AHWPs, the rotated central HWP layer mixes the two polarizations, so they can no longer be treated completely separately.

The modeling computer code mostly follows the same steps from before, but with added steps and features. It again starts with a single output wave, and calculates the input and reflection in relative terms, but now it starts with assuming just x-polarized output, and calculates input (which has components in both polarizations). The process is repeated for a y-polarized output. These two calculations are then combined to calculate the outputs from single component polarized inputs.

In order to properly deal with the reflection off the rotated interface, I needed to approximate the index for the layer at an arbitrary angle. Following the derivation in [53], the effective index for a birefringent material rotated an angle ϕ is calculated as

$$\frac{\sin(\phi)^2}{n_e^2} + \frac{\cos(\phi)^2}{n_o^2} = \frac{1}{n_{effective}^2} \tag{4.13}$$

I also modeled this in HFSS, with measuring the reflection of a birefringent silicon layer as I rotate ϕ for a birefringent silicon model with a pitch of 400 μm and a cut width of 60 μm. Using Equation 3.2 and this data, I can measure the index as a function of angle.

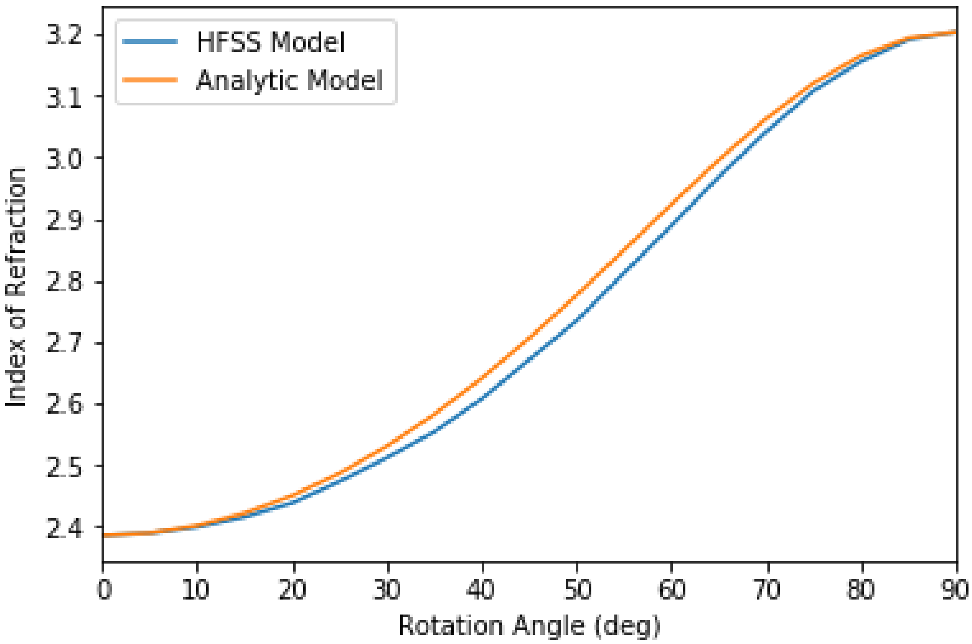

Figure 4.17: Index as a function of rotation angle. This figure shows both the HFSS model of birefringent silicon as well as an analytic model (with the indices from the HFSS model). As can be seen, the analytic and numeric models agree very well. This agreement helps create consistency in the design process.

Equation 4.13 matches the HFSS model of reflection quite well. A comparison between my analytic code and HFSS is shown in Figure 4.17.

4.6.3 Design

I explored models of low and high birefringence (constrained by achievable birefringence of metamaterial silicon), as well as allowing for silicon between each HWP layer. The optimization drove toward a low-birefringence model. This is because with high birefringence model, there would be larger reflections off the rotated HWP interfaces. For this same reason the optimization drove toward having no solid silicon in between HWP layers. The benefits of having another parameter to tune did not outweigh the cost of the stronger reflection off the HWP interfaces.

The next major challenge was to get the full geometry modeled in HFSS. This posed a problem; with the central layer rotated relative to the outer layers, if the cuts were the same (as they should be for a true Pancharatnam geometry), there is no way to get the cuts to line up properly on the boundary. After trying a few ways of combining several models together, I stumbled upon a simple solution: have a different pitch for the central layer.

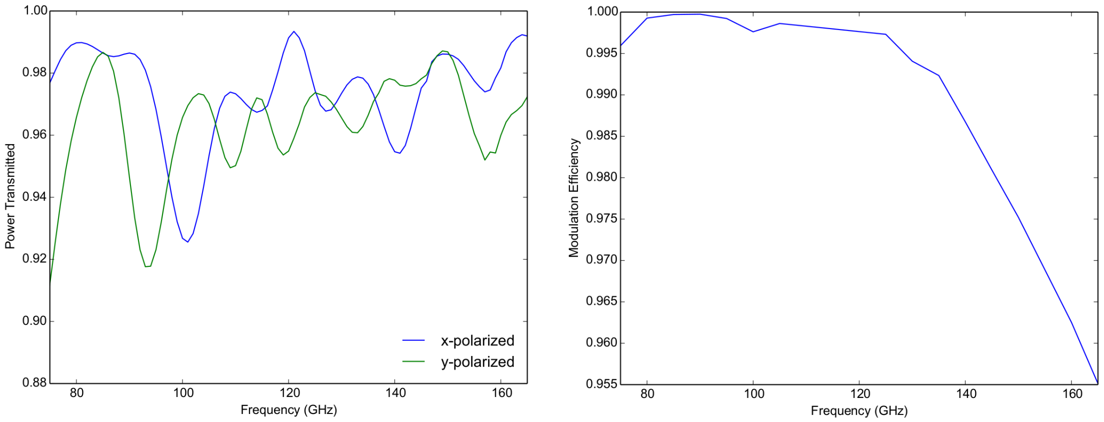

Figure 4.18: Results from my HFSS model for the MF HWP. Left shows the total transmission of the HWP for x and y polarized input, averaging over 96% across the band. Right shows the modulation efficiency as a function of frequency, averaging around 97% across the band.

Since all the HWPs are ideally identical, the width of the cuts would have to be cut down commensurately with the increase in pitch to maintain the same fill fraction.

There is the additional problem that in the model, the central cuts can't be rotated to any arbitrary angle (relative to the outer layers), only ones which allows for the boundaries to line up. Luckily the optimal rotation angle (58°) is near $\arctan(3/2) = 56.3°$. This allowed me to create a 3x2 pillar unit cell with proper boundary conditions. The HFSS model is shown in figure 4.10. This was then optimized using the previous procedure. The results are shown in Figure 4.18.

4.6.4 Fabrication

This fabrication was a significant deviation from the previous work. In order to have a central HWP cut, I had to start with two silicon plates. I would cut the central HWP into the thicker of the two plates, then bond the two together. After that, the cutting would proceed as normal. Several new fabrication steps needed to be implemented in order to fabricate this HWP. The two main new capabilities to work out were rotating the grooves a set angle, and bonding two separate pieces of silicon together.

First, I had to design alignment features into our HWP. The silicon plates each had a small (1mm diameter) notch in them. I had pin holes machined into the vacuum chuck that would use this notch to align the plate at either 0 or 56 degrees. First, the 56 degree setup was used to cut the central HWP layer. After bonding the two plates together, the HWP is remounted on the vacuum chuck in the 0 degree setup.

For bonding the plates, we chose an optical epoxy, Epotek 301-2. This is a long pot life, optically transparent epoxy. It was used by technicians at NASA Goddard for work on mirrors for Astro-H. Mimicking their setup and procedure, I helped design and build a spray coating system. This was two-axis gantry that would spray thinned epoxy horizontally. To thin the epoxy, the prescribed amounts of the two parts were throughly mixed, then a set volume of toluene was added to the epoxy and mixed further. The spraying was done with a standard high-volume low-pressure paint gun.

Before bonding, the silicon needs to be cleaned. A ten percent solution of sodium hydroxide is used to remove any metal residuals from the original machining. Acetone is used to remove any organics, such as fingerprints. Then a plasma cleaner is used to further clean the silicon surface. Additionally, the plasma cleaner makes the surface more hydrophilic, which helps keep the glue layer from beading.

The silicon is mounted horizontally on an aluminum plate. Most of the weight is supported by two pins. The silicon is held to the plate using double stick tape. The two-axis gantry would raster across the uncut silicon plate, laying down a uniform layer of epoxy (the toluene all evaporated in the spray). The plate would be positioned so we would spray into a fume hood. This system is be stable and repeatable, so we can control the thickness of the glue layer to a few microns. A typical thickness of the glue layer was 10 μm. With high loss tangent of $\delta \approx 10^2$, this amounted to about an additional half Kelvin of thermal loading.

After spraying, the aluminum plate is taken off the sprayer with the silicon still mounted, and put on a hot plate. The second piece of silicon is carefully placed on top of the first, using the pins already in place for alignment. Foam is then put on top of the silicon, then a piece of plastic is placed on top of the foam. A weight is then placed on the plastic. This layered system applies the force of the weight uniformly across the silicon. The epoxy is then cured at 80° C for three hours.

4.6.5 Testing and Results

The reflection and modulation efficiency were measured the same as for the previous HWP, except multiple sources were used to account for the broader bandwidth. The reflections are shown in Figures 4.19 and 4.20. Overall the reflections are quite low (averaging around 2-3%). They don't match the modeled performance as well as the AR coatings or single frequency HWP do. The modulation efficiency measurements are shown in Figures 4.21 and 4.22. The modulation efficiency is well matched to the model, and quite high (averaging around 97%).

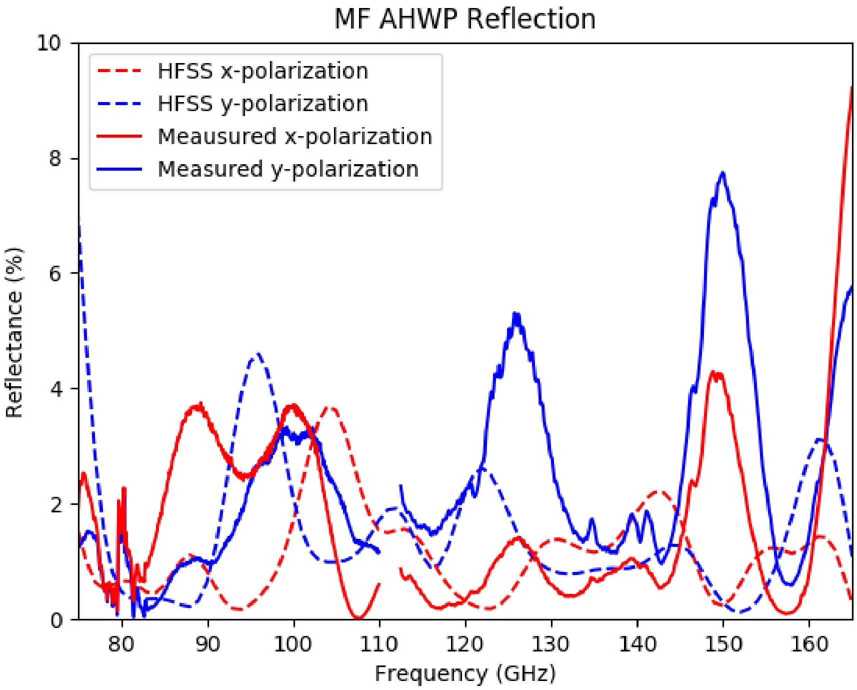

Figure 4.19: Reflection measurement of the MF AHWP. The reflections are not very well matched to the predicted, except that they are on the same sort of scale. I am unsure why there is such a discrepancy.

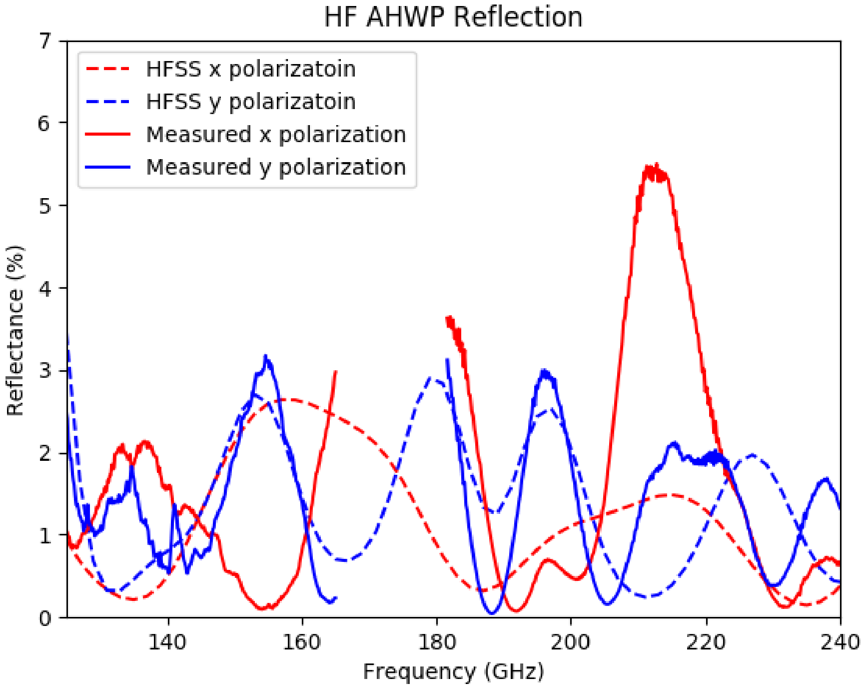

Figure 4.20: Reflection measurement of the HF AHWP. Again, the measured reflections only match the model to within a factor of two or so.

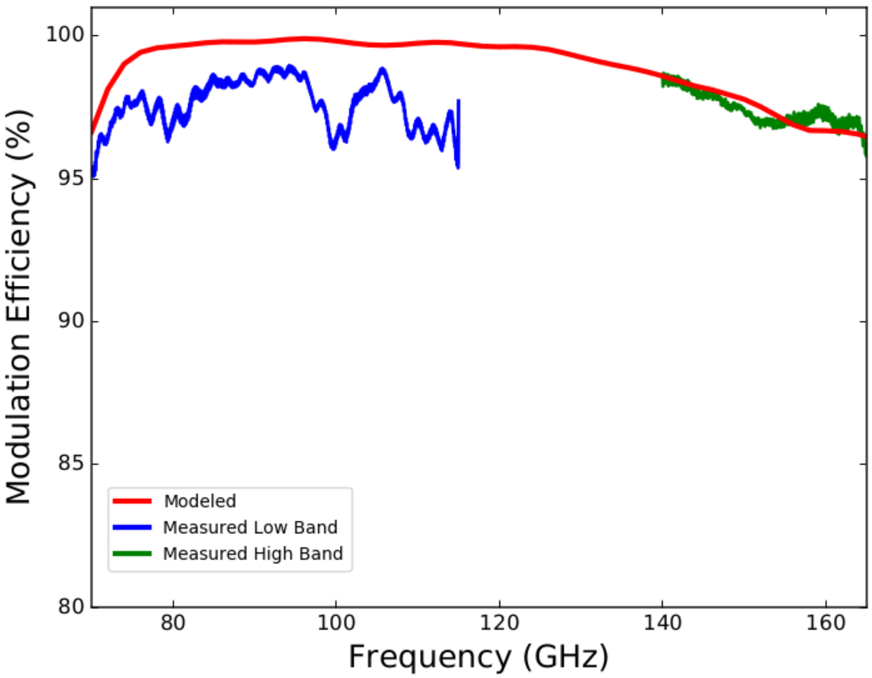

Figure 4.21: Modulation efficiency of one of the MF AHWPs as measured by the Goddard VNA quasioptical setup. The two bands of measured data are from separate VNA extender modules. The high band is well matched with the theoretical predictions, but the low band measurement is lower than expected (still sufficiently good though). This may be due to systematics in the lower band setup that are not fully understood.

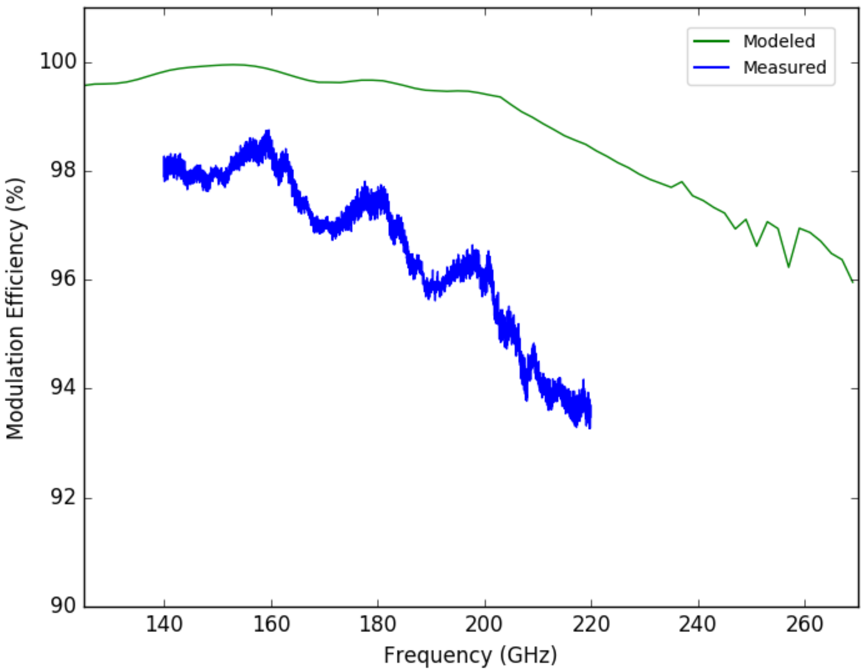

Figure 4.22: Modulation efficiency of one of the HF AHWPs as measured by the Goddard VNA quasioptical setup. There was only one band available to be used for measurement, so I couldn't measure the high end of the frequency range. This AHWPs modulation efficiency is significantly lower than expected at the high end of the band. This could be a systematic in the measurement setup.

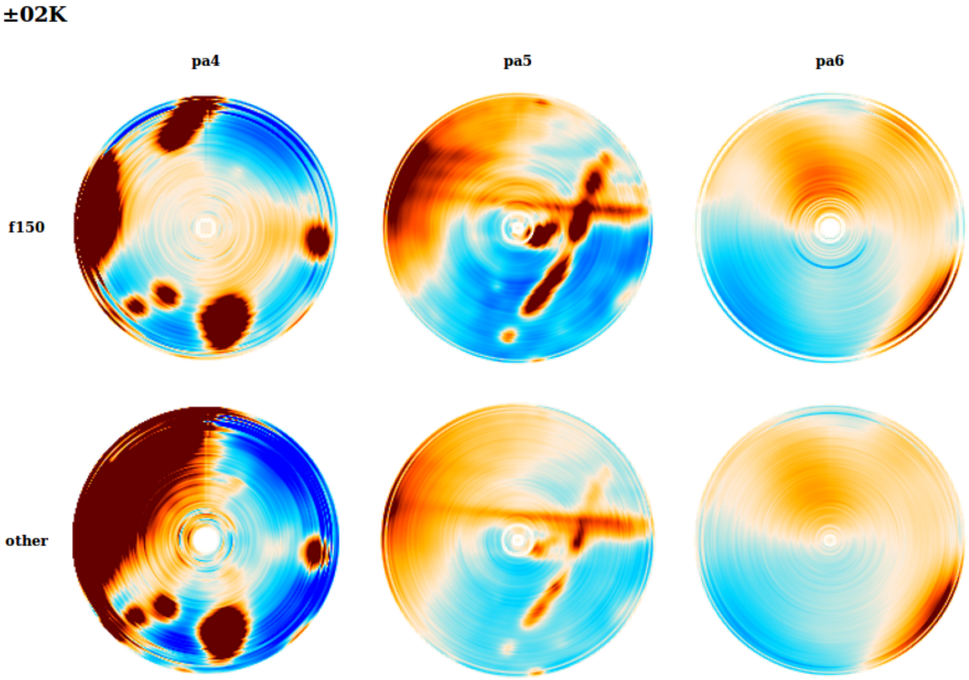

Figure 4.23: Emission intensity maps of the three deployed HWPs in both detector bands. PA4 (the HF HWP) has the most emission. I believe this is due to complications in fabrication.

4.6.6 Deployment

In August, 2017, I took all three HWPs down to the telescope in Chile. There, I worked to get the three of them properly mounted and spinning.

Before the full observation run, data was taken to measure the loading on the telescope. The thermal loading was measured with the HWPs on and off repeatedly to see how much the loading increased with the addition of the HWPs.

The full observing run lasted from October 12 to October 26, 2017. The data taken will allow us to work on our analysis techniques, and determine if the data modulation is worth the increase in noise. So far, we have not come to a solid conclusion.

4.6.7 HWP Readout

In order to properly analyze the telescope data, the HWP angle needs to be recorded with sub-degree precision. This is accomplished with two LEDs and photodiode encoders. The HWP is mounted in a metal ring (rotor), which is then mounted in front of the cryostat window. The rotor also has an outer ring with two sets of holes drilled in it. The outer set of holes are 180 evenly spaced ovals. The inner ring has 11 unevenly spaced holes. The LEDs

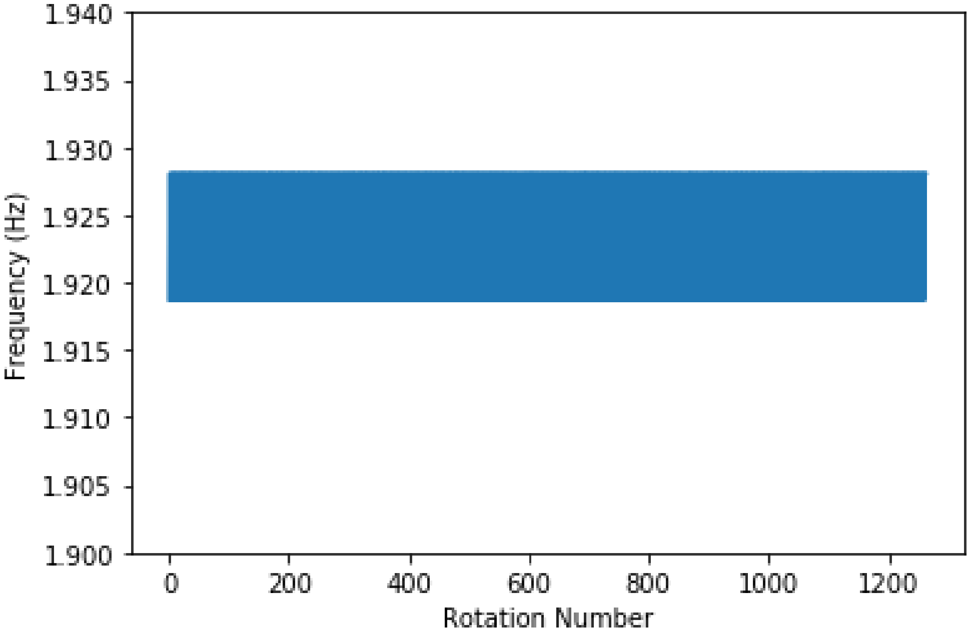

Figure 4.24: Measured HWP rotation frequency over a ten minute period. The rotation frequency is perfectly uniform to within the precision of our readout timing (the frequency bounces between two values set by the discretization of the time from ACT's digital clock). This is sufficiently uniform for our analysis to assume it is constant.

and diodes are mounted on the cryostat so that the ring on the HWP rotor passes between the LEDs and diodes. The voltage from the diode has a square waveform, pulsing each time a hole passes between the LEDs and diodes. The outer holes give precise angle positions, while the inner holes are used to set the absolute HWP angle. This encoder system is synced to our data readout, and the angle data is incorporated into our housekeeping data.

The HWP rotation frequency appears to be quite stable. Shown in Figure 4.24 is the frequency of the rotation over five minutes of data. As can be seen, the rotation varies between about 1.91 and 1.92 Hz. This shows that both the rotation mechanism and the readout system work well.

4.6.8 Timestream Analysis

Adding a HWP to the telescope optics chain dramatically changes how the data is interpreted. Before working the change into the map maker, I worked to understand some of the HWP properties from analysis of the timestream.

My first step is to just look at the data from single detectors. The data (with point glitches removed) for a particular detector in one TOD (see Section 2.7) are shown in Figure

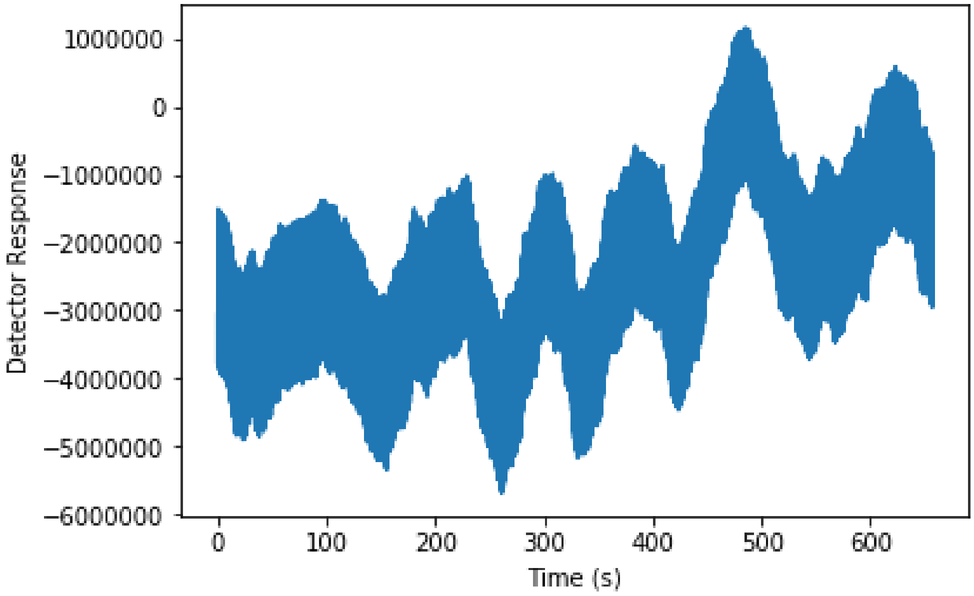

Figure 4.25: Response of a single detector over a single TOD. There is significant long term drift, but it is gradual (i.e. there are no discontinuities).

4.25. As can be seen there is a relatively smooth, if erratic, drift over the course of the TOD in the detector response. This sort of drift was common even without the HWP. To look at the effect of the HWP, you have to look at the data closer.

Figure 4.26 shows that same data, but zoomed in on 100-104 seconds (which is approximately eight HWP rotations). The HWP modulation is clear to see, and is dominated by a signal at the HWP frequency ($1f$ signal). For a sapphire HWP, the signal is dominated by a $2f$ signal due to the high level of symmetry in the crystal structure. While our metamaterials are quite uniform, they don't come close to the uniformity of natural crystal. The inhomogeneities break the two-fold symmetry, leading to a strong HWP-rotation synchronous signal. The inhomogeneities may be caused by unevenness of the glue layer, deformations in the wholly cut silicon wafer, or any solvent or wax left in the cracks from fabrication. These inhomogeneities lead to the peculiar shape of the detector response. This shape will be different for detectors at positions, as they will see different parts of the HWP.

One interesting thing to look at was to try and find two detectors which see nearly the same part of the HWP. I found two such detectors, which are at nearly the same radius, and rotated across the focal plane by the same amount the detectors are rotated. A comparison of these two detectors data is shown in Figure 4.27.

The output data appears to have a general drift of the signal over time, but if each rotation is mean subtracted, the signal is very stable. Shown in Figure 4.28 is all of the

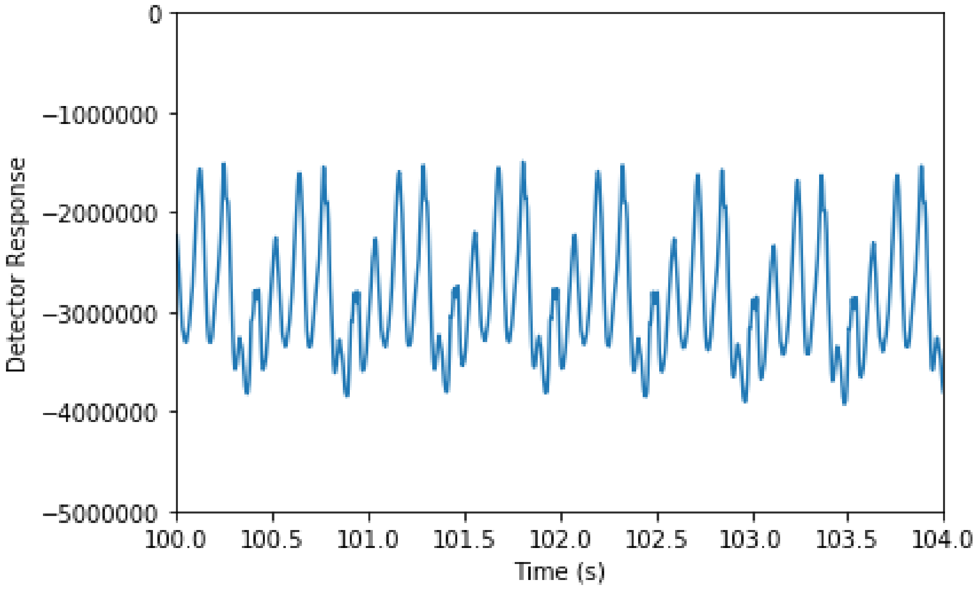

Figure 4.26: Response of a single detector over 4 seconds. The modulation can be seen clearly. The shape of the modulation is distinctly not sinusoidal, showing non-ideality of the HWP

HWP rotations from a single detector for a single TOD. There is no averaging. The plot shows 1263 HWP rotations all stacked.

Taking a Fourier Transform of this single TOD, the HWP peaks initially look very wide. If, however the TOD is cut to only include an integer number of HWP rotations, the peak narrows considerably. Additionally, all of the HWP rotations do not have the same number of samples, varying by one or two samples even for smooth rotations. This data can be resampled down to make a uniform number of samples per rotation. I did this by cubically splineing together the TOD, then sampling down to 200 samples per HWP rotation (down from about 204). Taking the FFT of this uniform sampling only marginally narrows the HWP peaks further, as can be seen in Figure 4.29. As such, I do not think this is a necessary step (for now at least).

Our signal is around the $4f$ peak, so if we can use the 1,2 and $3f$ harmonics to model the $4f$ signal, we can hopefully remove the intrinsic HWP signal (due to differential emission and transmission) from the sky signal. I looked at the correlations between the 1,2 and $3f$ signals and the $4f$. They are all fairly strongly correlated, but the noise is still too high. But there exists a linear combination of the three lower harmonics that is very strongly correlated with the $4f$ signal. Figure 4.30 shows the separate harmonics plotted versus $4f$ as well as the best linear combination to reduce the scatter.

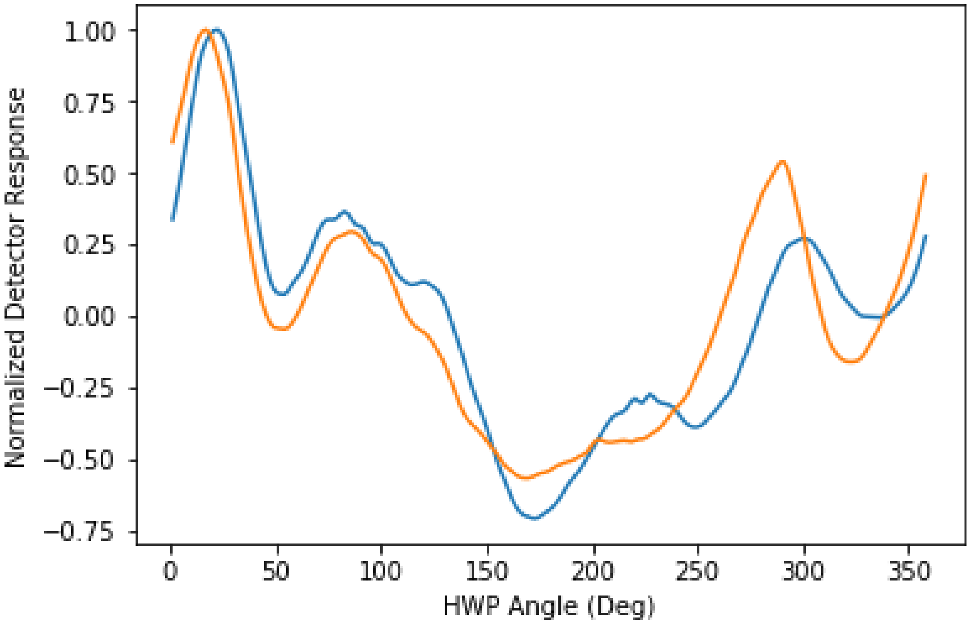

Figure 4.27: Normalized detctor response for two detectors at the same radius of the focal plane, separated by 45 degrees rotated from the center. The detectors are also rotated by 45 degrees, and the blue line is shifted by the same. This shows that most of the shape of the detector response plots are driven by the HWP, as these two detectors see nearly the same part of the same HWP.

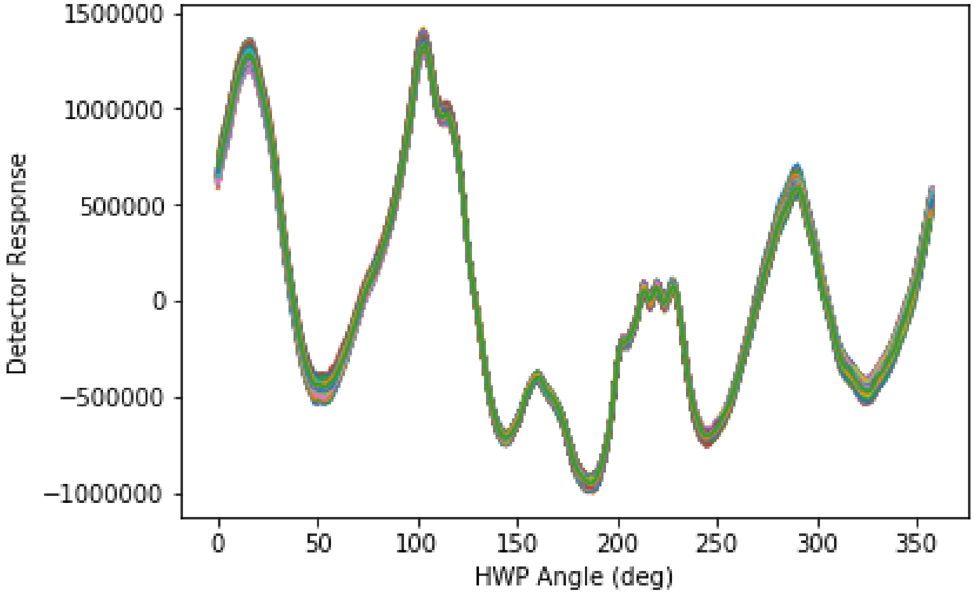

Figure 4.28: Stacked response of a single detector as a function of HWP angle for a single TOD. Each rotation has its mean subtracted to remove long term drifts. Around 1200 curves are plotted here, with minimal variation among them. This shows that the detector response to the HWP is stable, so it may be possible to subtract the HWP synchronous signal ($A(\chi)$) to better isolate the signal from the sky.

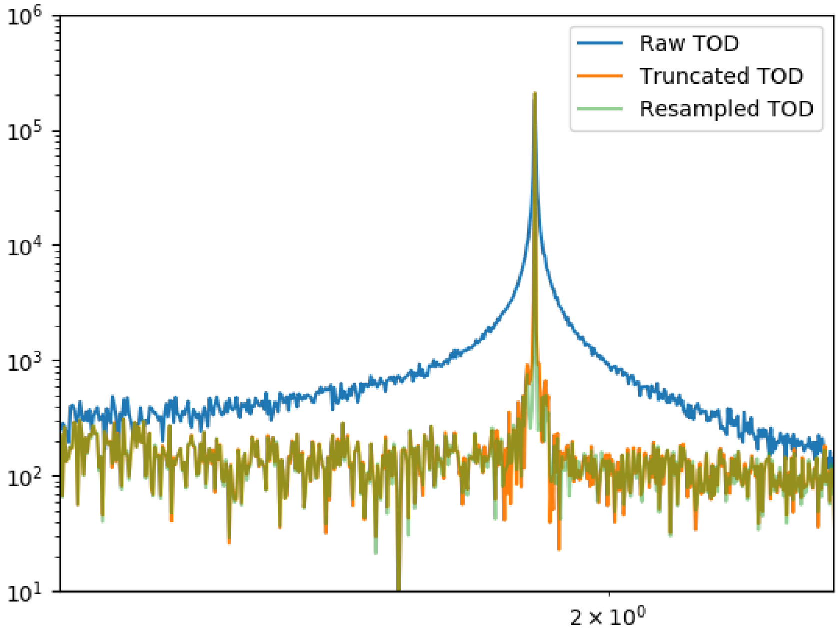

Figure 4.29: The first HWP peak of an FFT of a single detector for a single TOD. The blue line is an FFT of the raw TOD. The orange line is an FFT of the processed TOD where the start and end of the TOD are cut off so there is an integer number of HWP rotations. The green line is an FFT of a resampling of the data to simulate a perfectly uniform HWP rotation. As can be seen, all of the sharpening of the peak comes from TOD truncation. The HWP rotation speed is sufficiently uniform that resampling does not significantly improve the FFT.

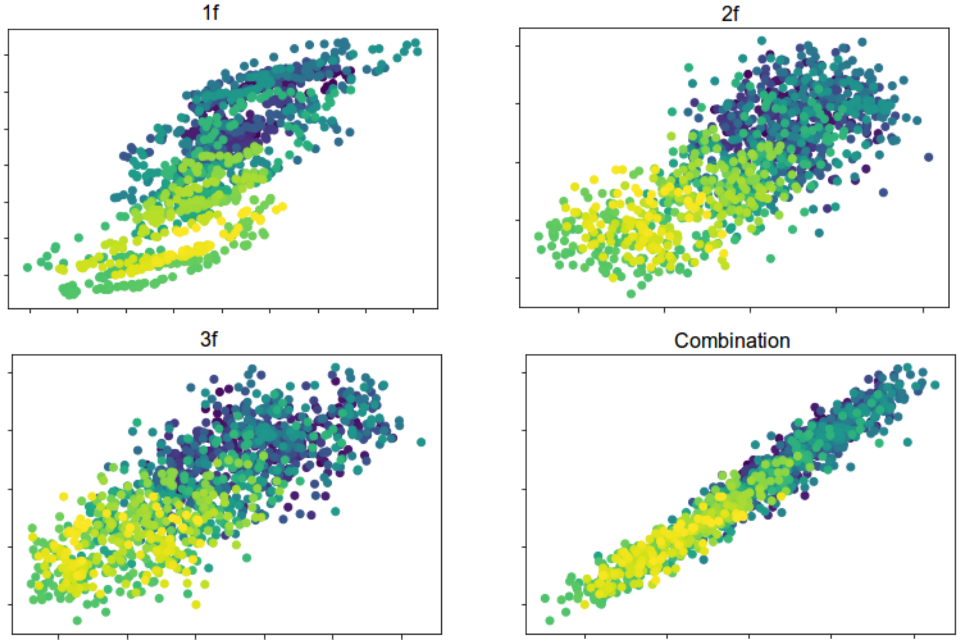

Figure 4.30: Top right, top left, and bottom right show the 1,2, and $3f$ components of the timestream of the HWP plotted against the $4f$ component (in arbitrary units). These components are calculated by taking an FFT of a single detector response. Each point on the plots represents a single HWP rotation. This was done for a single TOD, covering approximately 1200 HWP rotations. The bottom left shows a linear combination of the 1,2 and $3f$ components plotted against the $4f$. As can be seen, the correlation dramatically tightens when all three lower harmonics are used. This implies that the $4f$ component can be well estimated by knowing the 1,2, and $3f$ components. This may allow us to model the full $A(\chi)$ signal from just the first three components, so it can be subtracted from the timestream.

The next step in this will be to check for this linear combination across different detectors, and over different TODs. If this linear combination remains constant for a particular detector over several TODs, then this will be an powerful tool in isolating our singal.

4.6.9 Summary

While the analysis is still ongoing, the in-lab testing suggests that the AHWPs will benefit our data collection. As the analysis progresses, we will begin looking at redeploying them permanently. When one of the MF arrays is replaced with the LF array, the HWP will need to be taken off. It is likely that we will not observe the LF band with a HWP for several reasons, but it is likely it will not be needed. Additionally, there are practical concerns. The LF AHWP would weigh several kilograms, and our current air bearing system was not designed to hold such a heavy plate. The encoder system likewise was not designed for a HWP as thick as the LF would be, as it was optimized for the MF system and the LF AHWP would be several times thicker than the MF.

4.7 HWP Outlook

The metamaterial HWPs presented in this section represent a still nascent but rapidly developing technologies. Further development in the fabrication and cleaning processes might yield higher modulation efficiency, lower reflections and lower emission. The data we have in hand might show that indeed this technology is sufficiently developed to give sapphire a run for its money.

This technology does have one very specific, absolute advantage over standard sapphire HWPs that might lead to a niche. These metamaterials are substantially more birefringent than any natural material. As such, the HWPs are a factor of 2 or 3 thinner than sapphire ones at equivalent frequencies. They are also less dense, as they have about 30% of their mass removed during fabrication. This leads to a nearly order of magnitude reduction in weight. This can become important for balloon- or space-based telescopes, where weight becomes a major concern. Even if no more progress is made in development of this technology, it is already a viable material for such weight constrained experiments. Time will tell whether these HWPs will become the standard technology in all observatories, be forgotten to history, or (most likely) land somewhere in between.

Chapter 5

Conclusion

The goal of the ACT collaboration is to better understand cosmology. This chapter presents an overview of the science prduced with the ACTPol and Advanced ACTPol instrument that was enabled by the optical elements described in this thesis.

5.1 ACTPol Science

5.1.1 Power Spectra

ACT has published two papers on CMB polarization power spectra [54, 55]. In the more recent one, we presented all six possible auto and cross spectra from $200 < \ell < 9000$. This data is only from the first two seasons of ACTPol, with 150 GHz array data, covering 548 square degrees of the sky. The sky coverage map for ACTPol Seasons 1,2 and 3 is shown in Figure 5.1. Six acoustic peaks are significantly detected in the EE spectrum below ℓ of 3000. The TT, TE, and EE power spectra are shown in Figure 5.2. The limits on the BB power spectrum, as well as the data from other recent experiments, are shown in Figure 5.3.

This data is used to fit ΛCDM with WMAP priors on τ and the scalar spectral index. The cosmological parameters derived by ACT are consistent with those derived from Planck [56]. This paper also calculated the polarization spectra with and without masking point sources, and finds no significant contribution to the polarization from point sources. As ACT continues its observations and data analysis work, we will have an order of magnitude more data that we currently do, and will be significantly more constraining on cosmology than Planck is.

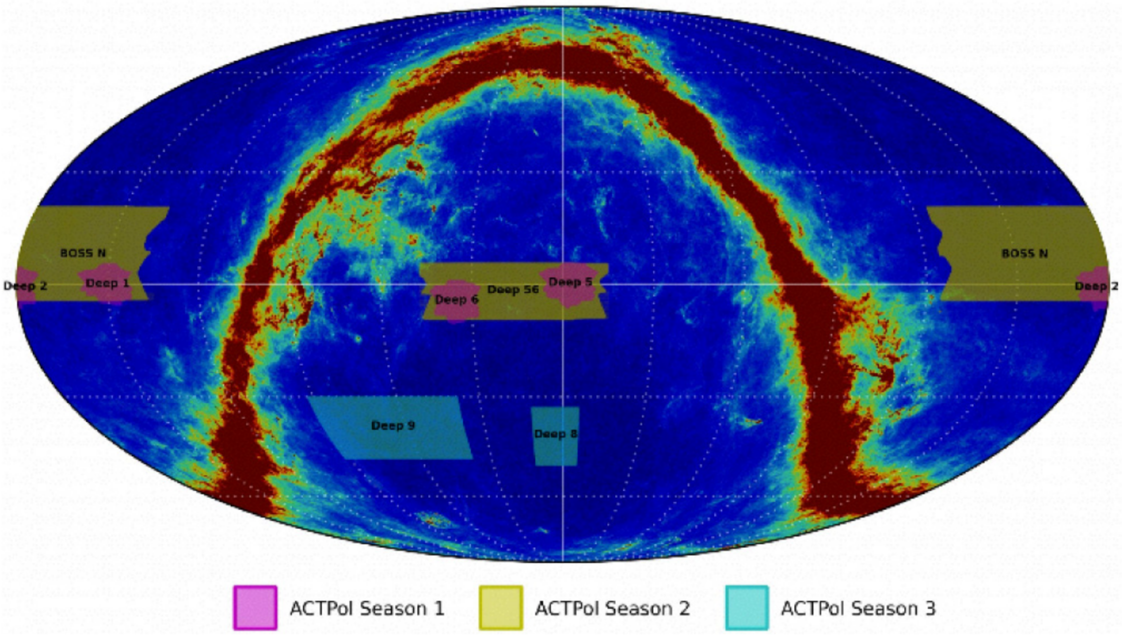

Figure 5.1: Sky coverage for ACTPol seasons 1, 2 and 3. As of writing this thesis, only data from the first two seasons of ACTPol have been published. Figure from the ACTPol Collaboration.

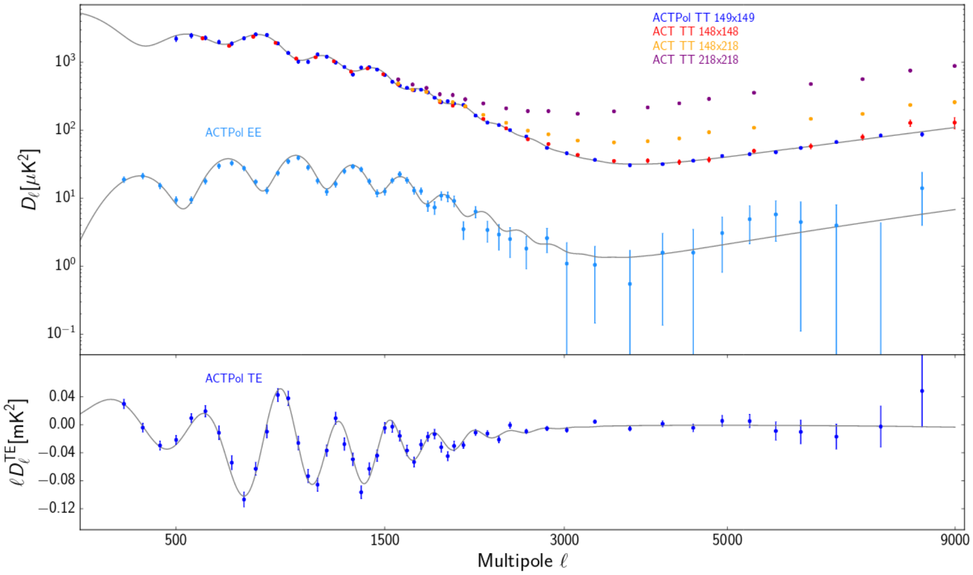

Figure 5.2: TT, EE, and TE power spectra for ACTPol.

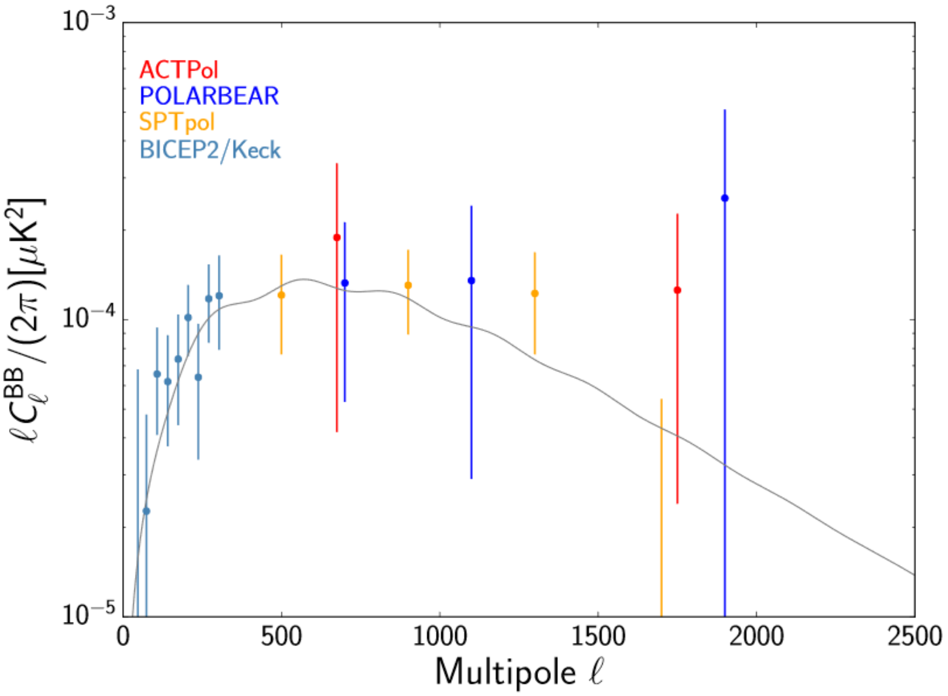

Figure 5.3: BB power spectrum for ACTPol. Other recent experiments are also plotted.

5.1.2 Lensing

As the CMB streams through the Universe, the varying gravitational potential lenses the signal. This signal shows up as correlations between previously uncorrelated modes. ACT has published several papers reporting measurements of this effect. Lensing can be a powerful tool for understanding the projected matter density of the Universe, which can help constrain growth of large scale structure, probing neutrino physics, dark matter, and dark energy.

One lensing paper just uses the CMB data from ACT. Using data from the first two seasons of ACTPol observations, it finds the lensing power spectrum is consistent with the best fit cosmology from other probes. The lensing power spectrum is shown in Figure 5.4.

In van Engelen et al [12], the CMB lensing signal is cross correlated with the Cosmic Infrared Background, as measured by the Planck satellite. The paper finds a CMB lensing signal at 9.1σ significance. Additionally, using an EB cross power estimator, a lensed B-mode signal was found at 3.2σ significance. This was ACT's first measurement of B-mode polarization, found in a similar way to the South Pole Telescope detection [57]. As we get more data, ACT will be able to detect this B-mode signal on its own.

Madhavacheril et al [58] finds CMB lensing by stacking locations of optically selected galaxies. 12000 galaxies from the CMASS catalog were selected where ACT's footprint

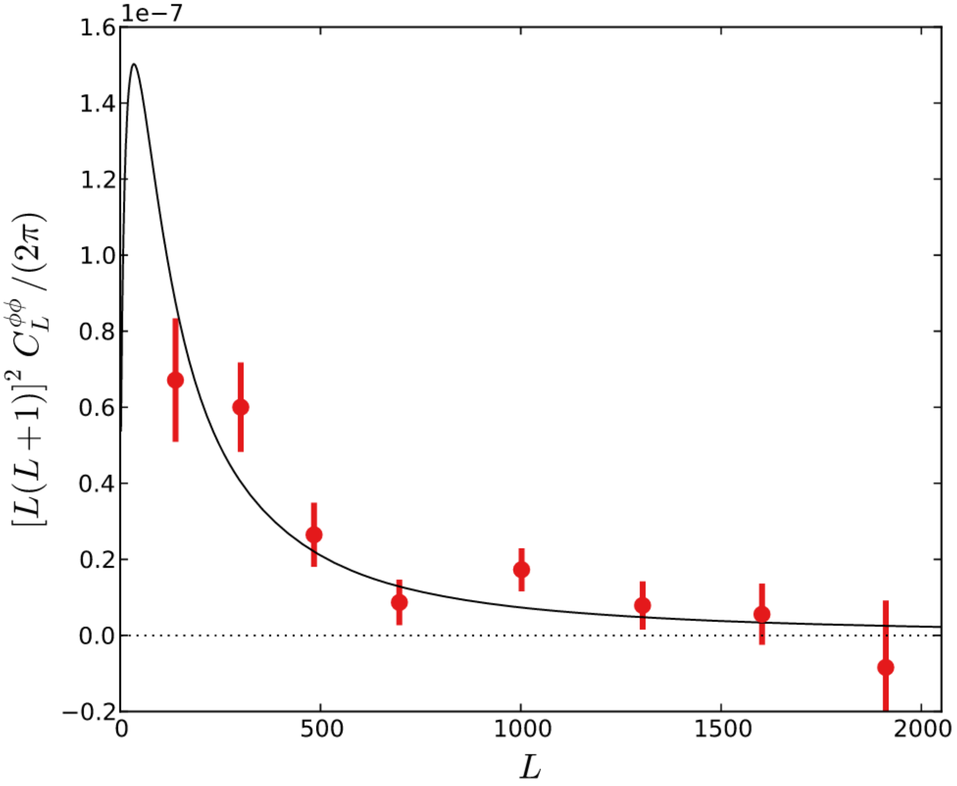

Figure 5.4: Lensing power spectrum coadded from all patches and estimators. The best fit cosmology for the data is consistent with that of Planck. Plot adapted from [12]

overlapped SDSS. The study detected lensing from the galactic halos at 3.2σ significance over null detection, which looked at instead stacking random points on the sky. Fitting the stacked lensing measurements to an NFW profile provided mass estimates that were in line with optical weak lensing mass estimates. This is exciting since it paves the way for CMB lensing to be used as a mass calibrator for clusters. In the CMB-S4 era, this calibration in conjunction with SZ cluster sample can be used to place tight constraints on the neutrino mass sum and dark energy parameters, complimentary to those from weak gravitational lensing.

5.1.3 SZ Effect

As CMB photons move through large galaxy clusters, a fraction of them will scatter off of the hot electrons in the intercluster medium. The high temperature of the electrons serves to upscatter the photons to higher energy, shifting the temperature spectrum slightly. This primary effect from the temperature of the ICM is called the thermal Sunyaev-Zel'dovich (tSZ) effect, and is relatively simple to detect for very large clusters. In ACTPol's bands of 90/150 GHz, these clusters show up as dark point sources in the CMB map.

This tSZ signal can be used to measure the mass of the clusters. In effect, the more massive the cluster, the stronger the signal. An ACT paper [59] on this uses X-ray derived gas profiles of clusters and finds that the mass derived from the tSZ signal is consistent with the dynamical mass measurement from spectroscopic observations.

The bulk flow of galaxy clusters relative to the CMB rest frame also contribute to the scattering. This is referred to as the kinetic SZ (kSZ) effect. For very large galaxy clusters, this effect is more than an order of magnitude weaker than the tSZ [13]. For smaller galaxy clusters, these two effects are comparable, but also comparable to the noise of our maps.

In De Bernardis et al [13] we measured the pairwise momentum of bright galaxies. By making a differential pairwise measurement of a large number of galaxies (50,000), all other effects not proportional to the comoving distance between the galaxies gets canceled out, boosting the signal-to-noise ratio and allowing them to extract a signal nominally weaker than the noise in the CMB maps. The galaxy position, size, and velocity data were taken from the Baryon Oscillation Spectroscopic Survey (BOSS). The CMB temperature for a cluster was determined by the average temperature in a disk ($r = \alpha$) minus the average temperature in the surrounding annulus ($\alpha < r < \sqrt{2}\alpha$). The radius was chosen to maximize signal-to-noise of the sources (for this paper, it was set at 1.8'). The binned estimator is shown in Figure 5.5. This paves the way for the kSZ effect to be used as a complementary probe of structure growth.

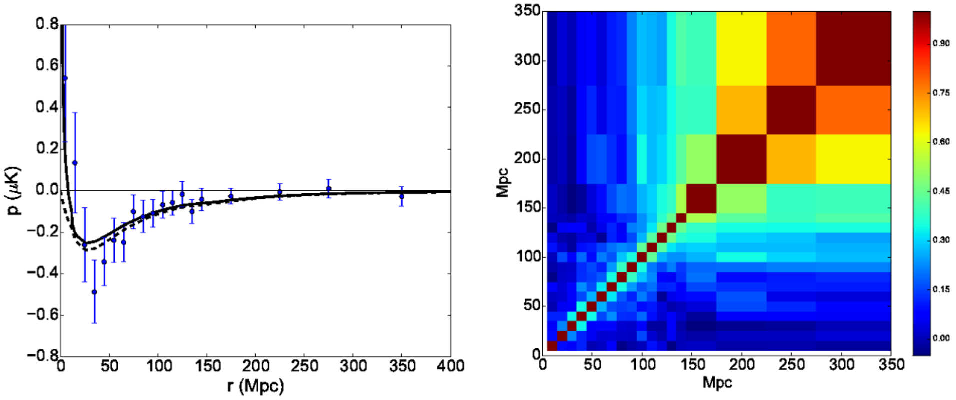

Figure 5.5: Left: Pairwise momentum estimator plotted vs pairwise distance. The dashed line is the best-fit linear model. The solid line is the best-fit nonlinear model, which accounts for redshift space distortions. The data provide kSZ detection at 4.1 σ significance. Right: Correlation matrix for comoving distance bins, estimated from 400 CMB realizations. Adapted from [13]

5.2 Concluding Remarks

The AR coating presented in this thesis will continue to be the best in the world for the foreseeable future. As our collaboration moves toward Simons Observatory, our lab will provide all new lenses. These lenses might be different size, shape, and frequency range than any produced before, and will thus need more work for process development. Additionally, the number of lenses needed for the new telescope will increase an order of magnitude, which means our production schedule will need to be ramped up commensurately.

The HWPs presented in this work do have significant advantages over conventional sapphire plates. It might be possible that any downsides be further mitigated with continued work, however this is not clear. More analysis needs to be done to determine if the benefits of my HWPs outweigh the costs, and if this technology, or the standard sapphire, will be applied for future experiments.

Whatever HWP technology is chosen for Simons Observatory (or possibly none), the metamaterial AR coatings, provided by the McMahon lab, will be used on the silicon reimaging optics. The scale of future ground-based CMB observatories is ambitious, but as others continue development of novel technologies and new analysis techniques, the secrets of the cosmos will steadily be revealed.

Appendix A

AR Modeling Code

```
import numpy as np

###############################################################################################
#This better find_reflectance function uses the matrix transfer method, and is
   much faster
#N_med is the index of outer medium. Arc stands for anti-reflection coating. br
   is birefringent
#cen is center layer. D for distance (thickness) of layer. N for Index

def find_reflectance2(N_ar,D_ar, freq_ar, ang_inc, pol = 'TM'):

   c = 300.       #speed of light in GHz and mms

   layers = len(N_ar)    #number of layers

       #convert arrays to numpy arrays
   N_ar = np.array(N_ar, dtype = complex)
   D_ar = np.array(D_ar)

   rho = (N_ar[:layers-1]-N_ar[1:])/(N_ar[:layers-1]+N_ar[1:])

   tau = 1.+rho

       #initialize reflection, transmission, and phase arrays
   R = np.zeros(len(freq_ar))
   T = np.zeros(len(freq_ar))
```

```
   phase = np.zeros(len(freq_ar))


       #start finding reflction and such as a function of frequency
   for i in range(len(freq_ar)):
     freq = freq_ar[i]

       #initialize the right traveling wave in the last layer as 1 with zero
          phase
     E_out = np.array((1. +0.j, 0.0 + 0.j), dtype = complex)

     TM = get_transfer_matrix_ang_inc(N_ar, D_ar, ang_inc, freq,pol)
     E_p, E_n = np.dot(TM, E_out)

     E_out = (1. +0.j)

       #find reflection, transmission, and phase coefficients at this frequency
     R[i] = ((E_n/E_p)*(np.conjugate(E_n)/np.conjugate(E_p))).real
     T[i] = ((E_out/E_p)*(E_out/np.conjugate(E_p))).real

       #I use the function I just wrote to do this. The negative sign is becasue
          i found the input phase, but i want it to be output
       phase[i] = -find_phase(E_p.real,E_p.imag)

   return R, T, phase

#End of find_reflection function.

###############################################################################################

def get_transfer_matrix_ang_inc(N_ar, D_ar, ang_inc, freq, pol = 'TM'):
   if pol != 'TM' and pol != 'TE':
     print "Invalid Polarization. Please use TE or TM."
     return 0

   layers = len(D_ar)
   c = 300.
   n = N_ar
```

```
#get angles for each layer
ang_inc_ar = []
ang_inc_ar.append(ang_inc)
for i in range(1,layers):
   ang_new = np.arcsin(N_ar[0]/N_ar[i]*np.sin(ang_inc))
   ang_inc_ar.append(ang_new)
ang_inc_ar = np.array(ang_inc_ar)

#Now use this to get the effective thickness for the layers
D_eff = D_ar/np.cos(ang_inc_ar)

#Initialize the transfermatrix as the identity, make sure it holds complex
    numbers
TM = np.identity(2, dtype=complex)

#now run throgh the layers and create the transfer matrix
for i in range(layers-1,0,-1):

   tm = np.ones((2,2), dtype = complex)

   if pol == 'TM':
      tm[0,0] = (n[i]/n[i-1] + np.cos(ang_inc_ar[i])/np.cos(ang_inc_ar[i-1]))
      tm[0,1] = (n[i]/n[i-1] - np.cos(ang_inc_ar[i])/np.cos(ang_inc_ar[i-1]))
      tm[1,0] = (n[i]/n[i-1] - np.cos(ang_inc_ar[i])/np.cos(ang_inc_ar[i-1]))
      tm[1,1] = (n[i]/n[i-1] + np.cos(ang_inc_ar[i])/np.cos(ang_inc_ar[i-1]))

   if pol == 'TE':
      tm[0,0] = (1+n[i]/n[i-1]*np.cos(ang_inc_ar[i])/np.cos(ang_inc_ar[i-1]))
      tm[0,1] = (1-n[i]/n[i-1]*np.cos(ang_inc_ar[i])/np.cos(ang_inc_ar[i-1]))
      tm[1,0] = (1-n[i]/n[i-1]*np.cos(ang_inc_ar[i])/np.cos(ang_inc_ar[i-1]))
      tm[1,1] = (1+n[i]/n[i-1]*np.cos(ang_inc_ar[i])/np.cos(ang_inc_ar[i-1]))

   tm = 0.5*tm

   TM = np.dot(tm,TM)
```

```
        prop = np.identity(2, dtype=complex)

        ptx = 2.*np.pi*D_eff[i-1]*freq*n[i-1]/c

        prop[0,0] = np.exp(1.j*ptx)
        prop[1,1] = np.exp(-1.j*ptx)

        TM = np.dot(prop,TM)

    return TM
```

Appendix B

HWP Modeling Code

```python
import numpy as np

###############################################################################################
#Function for finding the reflection and transmission of geometry with rotated hwps

def find_reflectance_angle(N1, N2,D, freq_ar, angles):

    #Just declaring some initial variables that I will use later
    #R for reflection, T for transmssion, and P for phase

    R = np.zeros((len(freq_ar),4))
    T = np.zeros((len(freq_ar),4))
    P = np.zeros((len(freq_ar),4))

    #These are used to hold the S parameters of the input fields. I can probably streamline this a bit.
    #The first index of these is for the frequency. The second parameter has to do with which field it represents
    #S[i][0] is the rtw in x pol, S[i][1] is the ltw in x pol. 2 and 3 are y pol rtw and ltw respectivley
    S = np.zeros((len(freq_ar),4), dtype = complex)
    S2 = np.zeros((len(freq_ar),4), dtype = complex)
    S3 = np.zeros((len(freq_ar),4), dtype = complex)

    #determine if angles are non-zero
```

```
straight = True
for i in range(len(angles)):
   if angles[i]%90 == 0: continue
   straight = False

############################################################################################
#Start the frequency sweep
for i in range(len(freq_ar)):
   freq = freq_ar[i]

   #Get the transfer matrix for this frequency
   TM = get_transfer_matrix(N1,N2,D,freq,angles)

   #########################################################################################

   #Start off with a zero phase, x polarized output
   output_1 = np.array((1,0,0,0), dtype=complex)

   #Get the input from this output
   S[i] = np.dot(TM,output_1)

   #This section works on adjusting the phase such that one polarization input
       has zero phase, as oppsed to output
   #This is important because in order to cancel out one input polarization
       the two basis vectors need to have equal phase
   #The if statment is necessary to ensure there is mixing betweent the
       layers. This is important to avoid dividing by zero
   if abs(S[i][0]) > 10**-9 and abs(S[i][2]) > 10**-9:

      #I take the conjugate unit vector of the input and use that as the
          output. This sets the input phase to zero
      temp = S[i][2]/(S[i][2]*np.conjugate(S[i][2]))**0.5
      output_1 = np.array((np.conjugate(temp),0,0,0))
      #And I get my new zero phase input, used as one of my basis vectors
      S[i] = np.dot(TM,output_1)

      #Use y polarized output to get other basis vector
      output_2 = np.array((0,0,1,0))
```

```
    #I don't check for zeros here because since x polarized output has mixed input, so will y polarized output
    S2[i] = np.dot(TM,output_2)
    #and I repeat the process for the other basis vector
    temp = S2[i][2]/(S2[i][2]*np.conjugate(S2[i][2]))**0.5
    output_2 = np.array((0,0,np.conjugate(temp),0))

    S2[i] = np.dot(TM,output_2)
    #I get the ratio of the y polarizations of the two basis vectors so I can cancel one
    #I use the real parts because setting phase to zero made the imag part zero
    ratio = S[i][2].real/S2[i][2].real
    #This output of x pol input
    output_3 = np.array((output_1[0],0,-ratio*output_2[2],0))

    #And the final product, x polarized input (may have non-zero phase
    S3[i] = np.dot(TM,output_3)

#This is if there is no mixing. Don't need basis vectors and canceling. The input is arleady polarized.

elif abs(S[i][0]) < 10**-9:
    output_3 = np.array((0,0,np.conjugate(temp),0))
    S3[i] = np.dot(TM,output_3)

elif abs(S[i][2]) < 10**-9:
    output_3 = np.array((1,0,0,0))
    S3[i] = np.dot(TM,output_3)

#This gives the magnitude of the input
Input = (S3[i][0]*np.conjugate(S3[i][0])).real

#These are the x and y componets with an x polarized input.
R[i][0] = (S3[i][1]*np.conjugate(S3[i][1])).real/Input
R[i][1] = (S3[i][3]*np.conjugate(S3[i][3])).real/Input

T[i][0] = (output_3[0]*np.conjugate(output_3[0])).real/Input
```

```
T[i][1] = (output_3[2]*np.conjugate(output_3[2])).real/Input

         #Now I've got to find the phase difference of the input and output
             (they both are likely not zero, but can be)
#How do I do this...
#So S3 has the complex S parameters of the input as S3[0].

phase_in = find_phase(S3[i][0].real,S3[i][0].imag)

#And output_3 has the (possibly) complex values for the output,
#but it is a numpy array and can handle calling imag parts even if they
   don't exist.

phase_out1 = find_phase(output_3[0].real,output_3[0].imag)
phase_out2 = find_phase(output_3[2].real,output_3[2].imag)

         #What I'm actually interested in is the phase shift across the
             structure
P[i][0] = phase_out1-phase_in
P[i][1] = phase_out2-phase_in

###########################################################################################
#Now I go through and do the same thing for y polarized input. Its pretty
   much exactly the same
output_1 = np.array((1,0,0,0))

S[i] = np.dot(TM,output_1)

if abs(S[i][0]) > 10**-9 and abs(S[i][2]) > 10**-9:
   temp = S[i][0]/(S[i][0]*np.conjugate(S[i][0]))**0.5
   output_1 = np.array((np.conjugate(temp),0,0,0))

   S[i] = np.dot(TM,output_1)

   output_2 = np.array((0,0,1,0))

   S2[i] = np.dot(TM,output_2)
```

```
    temp = S2[i][0]/(S2[i][0]*np.conjugate(S2[i][0]))**0.5
    output_2 = np.array((0,0,np.conjugate(temp),0))

    S2[i] = np.dot(TM,output_2)

    ratio = S[i][0].real/S2[i][0].real

    output_3 = np.array((output_1[0],0,-ratio*output_2[2],0))

    S3[i] = np.dot(TM,output_3)

elif abs(S[i][0]) < 10**-9:
    output_3 = np.array((1,0,0,0))
    S3[i] = np.dot(TM,output_3)

elif abs(S[i][2]) < 10**-9:
    output_3 = np.array((0,0,1,0))
    S3[i] = np.dot(TM,output_3)

Input = (S3[i][2]*np.conjugate(S3[i][2])).real

R[i][2] = (S3[i][1]*np.conjugate(S3[i][1])).real/Input
R[i][3] = (S3[i][3]*np.conjugate(S3[i][3])).real/Input

T[i][2] = (output_3[0]*np.conjugate(output_3[0])).real/Input
T[i][3] = (output_3[2]*np.conjugate(output_3[2])).real/Input

#So S3 has the complex S parameters of the input as S3[2] (now y polarized)

phase_in = find_phase(S3[i][2].real,S3[i][2].imag)

#And output_3 has the (possibly) complex values for the output,
#but it is a numpy array and can handle calling imag parts even if they
    don't exist.

phase_out1 = find_phase(output_3[0].real,output_3[0].imag)
phase_out2 = find_phase(output_3[2].real,output_3[2].imag)
```

```
                    #What I’m actually interested in is the phase shift across the
                      structure
        P[i][2] = phase_out1-phase_in
        P[i][3] = phase_out2-phase_in
        #########################################################################################


    T[:,0] = T[:,0]*N1[-1].real/N1[0].real
    T[:,1] = T[:,1]*N1[-1].real/N2[0].real
    T[:,2] = T[:,2]*N2[-1].real/N1[0].real
    T[:,3] = T[:,3]*N2[-1].real/N2[0].real
    return R, T, P


#End of find_reflectance_angle
```

Bibliography

[1] E. Hubble, "A relation between distance and radial velocity among extra-galactic nebulae," *Proceedings of the National Academy of Sciences*, vol. 15, no. 3, pp. 168–173, 1929.

[2] D. J. Fixsen, E. S. Cheng, J. M. Gales, J. C. Mather, R. A. ShaFer, and E. L. Wright, "The cosmic microwave background spectrum from the full cobe firas data set," *The Astrophysical Journal*, vol. 473, no. 2, p. 576, 1996.

[3] W. H. Hu, M. White, and E. Fermi, "A cmb polarization primer," 1997.

[4] R. Datta, *The First Multichroic Receiver and Results from ACTPol*. PhD thesis, University of Michigan, 2016.

[5] W. Hu and S. Dodelson, "Cosmic microwave background anisotropies," *Annual Review of Astronomy and Astrophysics*, vol. 40, no. 1, pp. 171–216, 2002.

[6] Planck Collaboration, Adam, R., Ade, P. A. R., Aghanim, N., Alves, M. I. R., Arnaud, M., Ashdown, M., Aumont, J., Baccigalupi, C., Banday, A. J., Barreiro, R. B., Bartlett, J. G., Bartolo, N., Battaner, E., Benabed, K., Benoît, A., Benoit-Lévy, A., Bernard, J.-P., Bersanelli, M., Bielewicz, P., Bock, J. J., Bonaldi, A., Bonavera, L., Bond, J. R., Borrill, J., Bouchet, F. R., Boulanger, F., Bucher, M., Burigana, C., Butler, R. C., Calabrese, E., Cardoso, J.-F., Catalano, A., Challinor, A., Chamballu, A., Chary, R.-R., Chiang, H. C., Christensen, P. R., Clements, D. L., Colombi, S., Colombo, L. P. L., Combet, C., Couchot, F., Coulais, A., Crill, B. P., Curto, A., Cuttaia, F., Danese, L., Davies, R. D., Davis, R. J., de Bernardis, P., de Rosa, A., de Zotti, G., Delabrouille, J., Désert, F.-X., Dickinson, C., Diego, J. M., Dole, H., Donzelli, S., Doré, O., Douspis, M., Ducout, A., Dupac, X., Efstathiou, G., Elsner, F., Enßlin, T. A., Eriksen, H. K., Falgarone, E., Fergusson, J., Finelli, F., Forni, O., Frailis, M., Fraisse, A. A., Franceschi, E., Frejsel, A., Galeotta, S., Galli, S., Ganga, K., Ghosh, T., Giard, M., Giraud-Héraud, Y., Gjerløw, E., González-Nuevo, J., Górski, K. M., Gratton, S., Gregorio, A., Gruppuso, A., Gudmundsson, J. E., Hansen, F. K., Hanson, D., Harrison, D. L., Helou, G., Henrot-Versillé, S., Hernández-Monteagudo, C., Herranz, D., Hildebrandt, S. R., Hivon, E., Hobson, M., Holmes, W. A., Hornstrup, A., Hovest, W., Huffenberger, K. M., Hurier, G., Jaffe, A. H., Jaffe, T. R., Jones, W. C., Juvela, M., Keihänen, E., Keskitalo, R., Kisner, T. S., Kneissl, R., Knoche, J., Kunz, M., Kurki-Suonio, H., Lagache, G., Lähteenmäki, A., Lamarre, J.-M., Lasenby, A., Lattanzi, M., Lawrence, C. R., Le Jeune, M., Leahy, J. P., Leonardi, R., Lesgourgues, J., Levrier,

F., Liguori, M., Lilje, P. B., Linden-Vørnle, M., López-Caniego, M., Lubin, P. M., Macías-Pérez, J. F., Maggio, G., Maino, D., Mandolesi, N., Mangilli, A., Maris, M., Marshall, D. J., Martin, P. G., Martínez-González, E., Masi, S., Matarrese, S., McGehee, P., Meinhold, P. R., Melchiorri, A., Mendes, L., Mennella, A., Migliaccio, M., Mitra, S., Miville-Deschênes, M.-A., Moneti, A., Montier, L., Morgante, G., Mortlock, D., Moss, A., Munshi, D., Murphy, J. A., Naselsky, P., Nati, F., Natoli, P., Netterfield, C. B., Nørgaard-Nielsen, H. U., Noviello, F., Novikov, D., Novikov, I., Orlando, E., Oxborrow, C. A., Paci, F., Pagano, L., Pajot, F., Paladini, R., Paoletti, D., Partridge, B., Pasian, F., Patanchon, G., Pearson, T. J., Perdereau, O., Perotto, L., Perrotta, F., Pettorino, V., Piacentini, F., Piat, M., Pierpaoli, E., Pietrobon, D., Plaszczynski, S., Pointecouteau, E., Polenta, G., Pratt, G. W., Prézeau, G., Prunet, S., Puget, J.-L., Rachen, J. P., Reach, W. T., Rebolo, R., Reinecke, M., Remazeilles, M., Renault, C., Renzi, A., Ristorcelli, I., Rocha, G., Rosset, C., Rossetti, M., Roudier, G., Rubiño-Martín, J. A., Rusholme, B., Sandri, M., Santos, D., Savelainen, M., Savini, G., Scott, D., Seiffert, M. D., Shellard, E. P. S., Spencer, L. D., Stolyarov, V., Stompor, R., Strong, A. W., Sudiwala, R., Sunyaev, R., Sutton, D., Suur-Uski, A.-S., Sygnet, J.-F., Tauber, J. A., Terenzi, L., Toffolatti, L., Tomasi, M., Tristram, M., Tucci, M., Tuovinen, J., Umana, G., Valenziano, L., Valiviita, J., Van Tent, F., Vielva, P., Villa, F., Wade, L. A., Wandelt, B. D., Wehus, I. K., Wilkinson, A., Yvon, D., Zacchei, A., and Zonca, A., "Planck 2015 results - x. diffuse component separation: Foreground maps," *A&A*, vol. 594, p. A10, 2016.

[7] M. H. Abitbol, Z. Ahmed, D. Barron, R. B. Thakur, A. N. Bender, B. A. Benson, C. A. Bischoff, S. A. Bryan, J. E. Carlstrom, C. L. Chang, D. T. Chuss, K. T. Crowley, A. Cukierman, T. de Haan, M. Dobbs, T. Essinger-Hileman, J. P. Filippini, K. Ganga, J. E. Gudmundsson, N. W. Halverson, S. Hanany, S. W. Henderson, C. A. Hill, S.-P. P. Ho, J. Hubmayr, K. Irwin, O. Jeong, B. R. Johnson, S. A. Kernasovskiy, J. M. Kovac, A. Kusaka, A. T. Lee, S. Maria, P. Mauskopf, J. J. McMahon, L. Moncelsi, A. W. Nadolski, J. M. Nagy, M. D. Niemack, R. C. O'Brient, S. Padin, S. C. Parshley, C. Pryke, N. A. Roe, K. Rostem, J. Ruhl, S. M. Simon, S. T. Staggs, A. Suzuki, E. R. Switzer, O. Tajima, K. L. Thompson, P. Timbie, G. S. Tucker, J. D. Vieira, A. G. Vieregg, B. Westbrook, E. J. Wollack, K. W. Yoon, K. S. Young, and E. Y. Young, "Cmb-s4 technology book, first edition," 2017.

[8] S. Paine, "The am atmospheric model," mar 2018.

[9] R. J. Thornton, P. A. R. Ade, S. Aiola, F. E. Angil, M. Amiri, J. A. Beall, D. T. Becker, H.-M. Cho, S. K. Choi, P. Corlies, K. P. Coughlin, R. Datta, M. J. Devlin, S. R. Dicker, R. Dnner, J. W. Fowler, A. E. Fox, P. A. Gallardo, J. Gao, E. Grace, M. Halpern, M. Hasselfield, S. W. Henderson, G. C. Hilton, A. D. Hincks, S. P. Ho, J. Hubmayr, K. D. Irwin, J. Klein, B. Koopman, D. Li, T. Louis, M. Lungu, L. Maurin, J. McMahon, C. D. Munson, S. Naess, F. Nati, L. Newburgh, J. Nibarger, M. D. Niemack, P. Niraula, M. R. Nolta, L. A. Page, C. G. Pappas, A. Schillaci, B. L. Schmitt, N. Sehgal, J. L. Sievers, S. M. Simon, S. T. Staggs, C. Tucker, M. Uehara, J. van Lanen, J. T. Ward, and E. J. Wollack, "The atacama cosmology telescope: The polarization-sensitive actpol instrument," *The Astrophysical Journal Supplement Series*, vol. 227, no. 2, p. 21, 2016.

[10] S. W. Henderson, R. Allison, J. Austermann, T. Baildon, N. Battaglia, J. A. Beall, D. Becker, F. De Bernardis, J. R. Bond, E. Calabrese, S. K. Choi, K. P. Coughlin, K. T. Crowley, R. Datta, M. J. Devlin, S. M. Duff, J. Dunkley, R. Dünner, A. van Engelen, P. A. Gallardo, E. Grace, M. Hasselfield, F. Hills, G. C. Hilton, A. D. Hincks, R. Hloek, S. P. Ho, J. Hubmayr, K. Huffenberger, J. P. Hughes, K. D. Irwin, B. J. Koopman, A. B. Kosowsky, D. Li, J. McMahon, C. Munson, F. Nati, L. Newburgh, M. D. Niemack, P. Niraula, L. A. Page, C. G. Pappas, M. Salatino, A. Schillaci, B. L. Schmitt, N. Sehgal, B. D. Sherwin, J. L. Sievers, S. M. Simon, D. N. Spergel, S. T. Staggs, J. R. Stevens, R. Thornton, J. Van Lanen, E. M. Vavagiakis, J. T. Ward, and E. J. Wollack, "Advanced actpol cryogenic detector arrays and readout," *Journal of Low Temperature Physics*, vol. 184, pp. 772–779, Aug 2016.

[11] G. Savini, G. Pisano, and P. A. R. Ade, "Achromatic half-wave plate for submillimeter instruments in cosmic microwave background astronomy: modeling and simulation," *Appl. Opt.*, vol. 45, pp. 8907–8915, Dec 2006.

[12] A. van Engelen, B. D. Sherwin, N. Sehgal, G. E. Addison, R. Allison, N. Battaglia, F. de Bernardis, J. R. Bond, E. Calabrese, K. Coughlin, D. Crichton, R. Datta, M. J. Devlin, J. Dunkley, R. Dnner, P. Gallardo, E. Grace, M. Gralla, A. Hajian, M. Hasselfield, S. Henderson, J. C. Hill, M. Hilton, A. D. Hincks, R. Hlozek, K. M. Huffenberger, J. P. Hughes, B. Koopman, A. Kosowsky, T. Louis, M. Lungu, M. Madhavacheril, L. Maurin, J. McMahon, K. Moodley, C. Munson, S. Naess, F. Nati, L. Newburgh, M. D. Niemack, M. R. Nolta, L. A. Page, C. Pappas, B. Partridge, B. L. Schmitt, J. L. Sievers, S. Simon, D. N. Spergel, S. T. Staggs, E. R. Switzer, J. T. Ward, and E. J. Wollack, "The atacama cosmology telescope: Lensing of cmb temperature and polarization derived from cosmic infrared background cross-correlation," *The Astrophysical Journal*, vol. 808, no. 1, p. 7, 2015.

[13] F. D. Bernardis, S. Aiola, E. Vavagiakis, N. Battaglia, M. Niemack, J. Beall, D. Becker, J. Bond, E. Calabrese, H. Cho, K. Coughlin, R. Datta, M. Devlin, J. Dunkley, R. Dunner, S. Ferraro, A. Fox, P. Gallardo, M. Halpern, N. Hand, M. Hasselfield, S. Henderson, J. Hill, G. Hilton, M. Hilton, A. Hincks, R. Hlozek, J. Hubmayr, K. Huffenberger, J. Hughes, K. Irwin, B. Koopman, A. Kosowsky, D. Li, T. Louis, M. Lungu, M. Madhavacheril, L. Maurin, J. McMahon, K. Moodley, S. Naess, F. Nati, L. Newburgh, J. Nibarger, L. Page, B. Partridge, E. Schaan, B. L. Schmitt, N. Sehgal, J. Sievers, S. Simon, D. Spergel, S. Staggs, J. Stevens, R. Thornton, A. van Engelen, J. V. Lanen, and E. Wollack, "Detection of the pairwise kinematic sunyaev-zel'dovich effect with boss dr11 and the atacama cosmology telescope," *Journal of Cosmology and Astroparticle Physics*, vol. 2017, no. 03, p. 008, 2017.

[14] A. Einstein, "Die grundlage der allgemeinen relativittstheorie," *Annalen der Physik*, vol. 49, 1916.

[15] A. Friedman, "ber die krmmung des raumes," *Z. Phys*, vol. 10, no. 1, 1922.

[16] G. Lematre, “A homogeneous universe of constant mass and increasing radius accounting for the radial velocity of extra-galactic nebulae,” *Ann. Soc. Sci. Brux*, vol. 47, p. 10, 1927.

[17] H. Kragh, *Cosmology And Controversy: the Historical Development of Two Theories of the Universe.* Princeton University Press, 1996.

[18] M. Zeilik and S. Gregory, *Introductory Astronomy & Astrophysics.* Saunders golden sunburst series, Saunders College Pub., 1998.

[19] H. S. Leavitt, “1777 variable in the magellanic clouds,” *Annals of the Harvard College Observatory*, 1908.

[20] “Extragalactic nebulae,” *Astrophysical Journal*, vol. 64, 1926.

[21] V. M. Slipher *Proc. Am. Philos. Soc*, vol. 56, 1917.

[22] R. A. Alpher, H. Bethe, and G. Gamow, “The origin of chemical elements,” *Phys. Rev.*, vol. 73, pp. 803–804, Apr 1948.

[23] R. A. ALPHER and R. HERMAN, “Evolution of the universe,” *Nature*, vol. 162, 1948.

[24] A. H. Guth, “Inflationary universe: A possible solution to the horizon and flatness problems,” *Phys. Rev. D*, vol. 23, pp. 347–356, Jan 1981.

[25] R. L. Davis, H. M. Hodges, G. F. Smoot, P. J. Steinhardt, and M. S. Turner, “Cosmic microwave background probes models of inflation,” *Phys. Rev. Lett.*, vol. 69, pp. 1856–1859, Sep 1992.

[26] A. R. Liddle and D. H. Lyth, “Cobe, gravitational waves, inflation and extended inflation,” *Physics Letters B*, vol. 291, no. 4, pp. 391 – 398, 1992.

[27] J. C. Mather, E. S. Cheng, R. E. Eplee, Jr., R. B. Isaacman, S. S. Meyer, R. A. Shafer, R. Weiss, E. L. Wright, C. L. Bennett, N. W. Boggess, E. Dwek, S. Gulkis, M. G. Hauser, M. Janssen, T. Kelsall, P. M. Lubin, S. H. Moseley, Jr., T. L. Murdock, R. F. Silverberg, G. F. Smoot, and D. T. Wilkinson, “A preliminary measurement of the cosmic microwave background spectrum by the cosmic background explorer (cobe) satellite,” *The Astrophysical Journal Letters*, vol. 354, pp. L37–L40, May 1990.

[28] G. F. Smoot, C. L. Bennett, A. Kogut, E. L. Wright, J. Aymon, N. W. Boggess, E. S. Cheng, G. de Amici, S. Gulkis, M. G. Hauser, G. Hinshaw, P. D. Jackson, M. Janssen, E. Kaita, T. Kelsall, P. Keegstra, C. Lineweaver, K. Loewenstein, P. Lubin, J. Mather, S. S. Meyer, S. H. Moseley, T. Murdock, L. Rokke, R. F. Silverberg, L. Tenorio, R. Weiss, and D. T. Wilkinson, “Structure in the cobe differential microwave radiometer first-year maps,” *The Astrophysical Journal Letters*, vol. 396, pp. L1–L5, Sept. 1992.

[29] A. D. Miller, R. Caldwell, M. J. Devlin, W. B. Dorwart, T. Herbig, M. R. Nolta, L. A. Page, J. Puchalla, E. Torbet, and H. T. Tran, “A measurement of the angular power spectrum of the cosmic microwave background from l = 100 to 400,” *The Astrophysical Journal Letters*, vol. 524, no. 1, p. L1, 1999.

[30] P. de Bernardis, P. A. R. Ade, J. J. Bock, J. R. Bond, J. Borrill, A. Boscaleri, K. Coble, B. P. Crill, G. De Gasperis, P. C. Farese, P. G. Ferreira, K. Ganga, M. Giacometti, E. Hivon, V. V. Hristov, A. Iacoangeli, A. H. Jaffe, A. E. Lange, L. Martinis, S. Masi, P. V. Mason, P. D. Mauskopf, A. Melchiorri, L. Miglio, T. Montroy, C. B. Netterfield, E. Pascale, F. Piacentini, D. Pogosyan, S. Prunet, S. Rao, G. Romeo, J. E. Ruhl, F. Scaramuzzi, D. Sforna, and N. Vittorio, “A flat universe from high-resolution maps of the cosmic microwave background radiation,” *Nature*, vol. 404, pp. 955 EP –, Apr 2000.

[31] S. Hanany, P. Ade, A. Balbi, J. Bock, J. Borrill, A. Boscaleri, P. de Bernardis, P. G. Ferreira, V. V. Hristov, A. H. Jaffe, A. E. Lange, A. T. Lee, P. D. Mauskopf, C. B. Netterfield, S. Oh, E. Pascale, B. Rabii, P. L. Richards, G. F. Smoot, R. Stompor, C. D. Winant, and J. H. P. Wu, “Maxima-1: A measurement of the cosmic microwave background anisotropy on angular scales of 10’-5,” *The Astrophysical Journal Letters*, vol. 545, no. 1, p. L5, 2000.

[32] C. L. Bennett, D. Larson, J. L. Weiland, N. Jarosik, G. Hinshaw, N. Odegard, K. M. Smith, R. S. Hill, B. Gold, M. Halpern, E. Komatsu, M. R. Nolta, L. Page, D. N. Spergel, E. Wollack, J. Dunkley, A. Kogut, M. Limon, S. S. Meyer, G. S. Tucker, and E. L. Wright, “Nine-year wilkinson microwave anisotropy probe (wmap) observations: Final maps and results,” *The Astrophysical Journal Supplement Series*, vol. 208, no. 2, p. 20, 2013.

[33] J. W. Fowler, V. Acquaviva, P. A. R. Ade, P. Aguirre, M. Amiri, J. W. Appel, L. F. Barrientos, E. S. Battistelli, J. R. Bond, B. Brown, B. Burger, J. Chervenak, S. Das, M. J. Devlin, S. R. Dicker, W. B. Doriese, J. Dunkley, R. Dnner, T. Essinger-Hileman, R. P. Fisher, A. Hajian, M. Halpern, M. Hasselfield, C. Hernndez-Monteagudo, G. C. Hilton, M. Hilton, A. D. Hincks, R. Hlozek, K. M. Huffenberger, D. H. Hughes, J. P. Hughes, L. Infante, K. D. Irwin, R. Jimenez, J. B. Juin, M. Kaul, J. Klein, A. Kosowsky, J. M. Lau, M. Limon, Y.-T. Lin, R. H. Lupton, T. A. Marriage, D. Marsden, K. Martocci, P. Mauskopf, F. Menanteau, K. Moodley, H. Moseley, C. B. Netterfield, M. D. Niemack, M. R. Nolta, L. A. Page, L. Parker, B. Partridge, H. Quintana, B. Reid, N. Sehgal, J. Sievers, D. N. Spergel, S. T. Staggs, D. S. Swetz, E. R. Switzer, R. Thornton, H. Trac, C. Tucker, L. Verde, R. Warne, G. Wilson, E. Wollack, and Y. Zhao, “The atacama cosmology telescope: A measurement of the 600 ¡ ¡ 8000 cosmic microwave background power spectrum at 148 ghz,” *The Astrophysical Journal*, vol. 722, no. 2, p. 1148, 2010.

[34] Z. Hou, C. L. Reichardt, K. T. Story, B. Follin, R. Keisler, K. A. Aird, B. A. Benson, L. E. Bleem, J. E. Carlstrom, C. L. Chang, H.-M. Cho, T. M. Crawford, A. T. Crites, T. de Haan, R. de Putter, M. A. Dobbs, S. Dodelson, J. Dudley, E. M. George, N. W. Halverson, G. P. Holder, W. L. Holzapfel, S. Hoover, J. D. Hrubes, M. Joy, L. Knox, A. T. Lee, E. M. Leitch, M. Lueker, D. Luong-Van, J. J. McMahon, J. Mehl, S. S. Meyer, M. Millea, J. J. Mohr, T. E. Montroy, S. Padin, T. Plagge, C. Pryke, J. E. Ruhl, J. T. Sayre, K. K. Schaffer, L. Shaw, E. Shirokoff, H. G. Spieler, Z. Staniszewski, A. A. Stark, A. van Engelen, K. Vanderlinde, J. D. Vieira, R. Williamson, and O. Zahn,

“Constraints on cosmology from the cosmic microwave background power spectrum of the 2500deg2 spt-sz survey,” *The Astrophysical Journal*, vol. 782, no. 2, p. 74, 2014.

[35] Planck Collaboration, Adam, R., Ade, P. A. R., Aghanim, N., Akrami, Y., Alves, M. I. R., Argeso, F., Arnaud, M., Arroja, F., Ashdown, M., Aumont, J., Baccigalupi, C., Ballardini, M., Banday, A. J., Barreiro, R. B., Bartlett, J. G., Bartolo, N., Basak, S., Battaglia, P., Battaner, E., Battye, R., Benabed, K., Benot, A., Benoit-Lvy, A., Bernard, J.-P., Bersanelli, M., Bertincourt, B., Bielewicz, P., Bikmaev, I., Bock, J. J., Bhringer, H., Bonaldi, A., Bonavera, L., Bond, J. R., Borrill, J., Bouchet, F. R., Boulanger, F., Bucher, M., Burenin, R., Burigana, C., Butler, R. C., Calabrese, E., Cardoso, J.-F., Carvalho, P., Casaponsa, B., Castex, G., Catalano, A., Challinor, A., Chamballu, A., Chary, R.-R., Chiang, H. C., Chluba, J., Chon, G., Christensen, P. R., Church, S., Clemens, M., Clements, D. L., Colombi, S., Colombo, L. P. L., Combet, C., Comis, B., Contreras, D., Couchot, F., Coulais, A., Crill, B. P., Cruz, M., Curto, A., Cuttaia, F., Danese, L., Davies, R. D., Davis, R. J., de Bernardis, P., de Rosa, A., de Zotti, G., Delabrouille, J., Delouis, J.-M., Dsert, F.-X., Di Valentino, E., Dickinson, C., Diego, J. M., Dolag, K., Dole, H., Donzelli, S., Dor, O., Douspis, M., Ducout, A., Dunkley, J., Dupac, X., Efstathiou, G., Eisenhardt, P. R. M., Elsner, F., Enlin, T. A., Eriksen, H. K., Falgarone, E., Fantaye, Y., Farhang, M., Feeney, S., Fergusson, J., Fernandez-Cobos, R., Feroz, F., Finelli, F., Florido, E., Forni, O., Frailis, M., Fraisse, A. A., Franceschet, C., Franceschi, E., Frejsel, A., Frolov, A., Galeotta, S., Galli, S., Ganga, K., Gauthier, C., Gnova-Santos, R. T., Gerbino, M., Ghosh, T., Giard, M., Giraud-Hraud, Y., Giusarma, E., Gjerlw, E., Gonzlez-Nuevo, J., Grski, K. M., Grainge, K. J. B., Gratton, S., Gregorio, A., Gruppuso, A., Gudmundsson, J. E., Hamann, J., Handley, W., Hansen, F. K., Hanson, D., Harrison, D. L., Heavens, A., Helou, G., Henrot-Versill, S., Hernndez-Monteagudo, C., Herranz, D., Hildebrandt, S. R., Hivon, E., Hobson, M., Holmes, W. A., Hornstrup, A., Hovest, W., Huang, Z., Huffenberger, K. M., Hurier, G., Ili, S., Jaffe, A. H., Jaffe, T. R., Jin, T., Jones, W. C., Juvela, M., Karakci, A., Keihnen, E., Keskitalo, R., Khamitov, I., Kiiveri, K., Kim, J., Kisner, T. S., Kneissl, R., Knoche, J., Knox, L., Krachmalnicoff, N., Kunz, M., Kurki-Suonio, H., Lacasa, F., Lagache, G., Lhteenmki, A., Lamarre, J.-M., Langer, M., Lasenby, A., Lattanzi, M., Lawrence, C. R., Le Jeune, M., Leahy, J. P., Lellouch, E., Leonardi, R., Len-Tavares, J., Lesgourgues, J., Levrier, F., Lewis, A., Liguori, M., Lilje, P. B., Lilley, M., Linden-Vrnle, M., Lindholm, V., Liu, H., Lpez-Caniego, M., Lubin, P. M., Ma, Y.-Z., Macas-Prez, J. F., Maggio, G., Maino, D., Mak, D. S. Y., Mandolesi, N., Mangilli, A., Marchini, A., Marcos-Caballero, A., Marinucci, D., Maris, M., Marshall, D. J., Martin, P. G., Martinelli, M., Martnez-Gonzlez, E., Masi, S., Matarrese, S., Mazzotta, P., McEwen, J. D., McGehee, P., Mei, S., Meinhold, P. R., Melchiorri, A., Melin, J.-B., Mendes, L., Mennella, A., Migliaccio, M., Mikkelsen, K., Millea, M., Mitra, S., Miville-Deschnes, M.-A., Molinari, D., Moneti, A., Montier, L., Moreno, R., Morgante, G., Mortlock, D., Moss, A., Mottet, S., Mnchmeyer, M., Munshi, D., Murphy, J. A., Narimani, A., Naselsky, P., Nastasi, A., Nati, F., Natoli, P., Negrello, M., Netterfield, C. B., Nrgaard-Nielsen, H. U., Noviello, F., Novikov, D., Novikov, I., Olamaie, M., Oppermann, N., Orlando, E., Oxborrow, C. A., Paci, F., Pagano, L., Pajot, F., Paladini, R., Pandolfi, S., Paoletti, D., Partridge, B., Pasian, F., Patanchon,

G., Pearson, T. J., Peel, M., Peiris, H. V., Pelkonen, V.-M., Perdereau, O., Perotto, L., Perrott, Y. C., Perrotta, F., Pettorino, V., Piacentini, F., Piat, M., Pierpaoli, E., Pietrobon, D., Plaszczynski, S., Pogosyan, D., Pointecouteau, E., Polenta, G., Popa, L., Pratt, G. W., Przeau, G., Prunet, S., Puget, J.-L., Rachen, J. P., Racine, B., Reach, W. T., Rebolo, R., Reinecke, M., Remazeilles, M., Renault, C., Renzi, A., Ristorcelli, I., Rocha, G., Roman, M., Romelli, E., Rosset, C., Rossetti, M., Rotti, A., Roudier, G., Rouill dOrfeuil, B., Rowan-Robinson, M., Rubio-Martn, J. A., Ruiz-Granados, B., Rumsey, C., Rusholme, B., Said, N., Salvatelli, V., Salvati, L., Sandri, M., Sanghera, H. S., Santos, D., Saunders, R. D. E., Sauv, A., Savelainen, M., Savini, G., Schaefer, B. M., Schammel, M. P., Scott, D., Seiffert, M. D., Serra, P., Shellard, E. P. S., Shimwell, T. W., Shiraishi, M., Smith, K., Souradeep, T., Spencer, L. D., Spinelli, M., Stanford, S. A., Stern, D., Stolyarov, V., Stompor, R., Strong, A. W., Sudiwala, R., Sunyaev, R., Sutter, P., Sutton, D., Suur-Uski, A.-S., Sygnet, J.-F., Tauber, J. A., Tavagnacco, D., Terenzi, L., Texier, D., Toffolatti, L., Tomasi, M., Tornikoski, M., Tramonte, D., Tristram, M., Troja, A., Trombetti, T., Tucci, M., Tuovinen, J., Trler, M., Umana, G., Valenziano, L., Valiviita, J., Van Tent, F., Vassallo, T., Vibert, L., Vidal, M., Viel, M., Vielva, P., Villa, F., Wade, L. A., Walter, B., Wandelt, B. D., Watson, R., Wehus, I. K., Welikala, N., Weller, J., White, M., White, S. D. M., Wilkinson, A., Yvon, D., Zacchei, A., Zibin, J. P., and Zonca, A., "Planck 2015 results - i. overview of products and scientific results," *Astronomy and Astrophysics*, vol. 594, p. A1, 2016.

[36] Planck Collaboration, Ade, P. A. R., Aghanim, N., Arnaud, M., Ashdown, M., Aumont, J., Baccigalupi, C., Banday, A. J., Barreiro, R. B., Bartlett, J. G., Bartolo, N., Battaner, E., Battye, R., Benabed, K., Benot, A., Benoit-Lvy, A., Bernard, J.-P., Bersanelli, M., Bielewicz, P., Bock, J. J., Bonaldi, A., Bonavera, L., Bond, J. R., Borrill, J., Bouchet, F. R., Boulanger, F., Bucher, M., Burigana, C., Butler, R. C., Calabrese, E., Cardoso, J.-F., Catalano, A., Challinor, A., Chamballu, A., Chary, R.-R., Chiang, H. C., Chluba, J., Christensen, P. R., Church, S., Clements, D. L., Colombi, S., Colombo, L. P. L., Combet, C., Coulais, A., Crill, B. P., Curto, A., Cuttaia, F., Danese, L., Davies, R. D., Davis, R. J., de Bernardis, P., de Rosa, A., de Zotti, G., Delabrouille, J., Dsert, F.-X., Di Valentino, E., Dickinson, C., Diego, J. M., Dolag, K., Dole, H., Donzelli, S., Dor, O., Douspis, M., Ducout, A., Dunkley, J., Dupac, X., Efstathiou, G., Elsner, F., Enlin, T. A., Eriksen, H. K., Farhang, M., Fergusson, J., Finelli, F., Forni, O., Frailis, M., Fraisse, A. A., Franceschi, E., Frejsel, A., Galeotta, S., Galli, S., Ganga, K., Gauthier, C., Gerbino, M., Ghosh, T., Giard, M., Giraud-Hraud, Y., Giusarma, E., Gjerlw, E., Gonzlez-Nuevo, J., Grski, K. M., Gratton, S., Gregorio, A., Gruppuso, A., Gudmundsson, J. E., Hamann, J., Hansen, F. K., Hanson, D., Harrison, D. L., Helou, G., Henrot-Versill, S., Hernndez-Monteagudo, C., Herranz, D., Hildebrandt, S. R., Hivon, E., Hobson, M., Holmes, W. A., Hornstrup, A., Hovest, W., Huang, Z., Huffenberger, K. M., Hurier, G., Jaffe, A. H., Jaffe, T. R., Jones, W. C., Juvela, M., Keihnen, E., Keskitalo, R., Kisner, T. S., Kneissl, R., Knoche, J., Knox, L., Kunz, M., Kurki-Suonio, H., Lagache, G., Lhteenmki, A., Lamarre, J.-M., Lasenby, A., Lattanzi, M., Lawrence, C. R., Leahy, J. P., Leonardi, R., Lesgourgues, J., Levrier, F., Lewis, A., Liguori, M., Lilje, P. B., Linden-Vrnle, M., Lpez-Caniego, M., Lubin, P. M., Macas-Prez, J. F., Maggio, G., Maino, D., Mandolesi, N., Mangilli, A., Marchini, A., Maris, M.,

Martin, P. G., Martinelli, M., Martnez-Gonzlez, E., Masi, S., Matarrese, S., McGehee, P., Meinhold, P. R., Melchiorri, A., Melin, J.-B., Mendes, L., Mennella, A., Migliaccio, M., Millea, M., Mitra, S., Miville-Deschnes, M.-A., Moneti, A., Montier, L., Morgante, G., Mortlock, D., Moss, A., Munshi, D., Murphy, J. A., Naselsky, P., Nati, F., Natoli, P., Netterfield, C. B., Nrgaard-Nielsen, H. U., Noviello, F., Novikov, D., Novikov, I., Oxborrow, C. A., Paci, F., Pagano, L., Pajot, F., Paladini, R., Paoletti, D., Partridge, B., Pasian, F., Patanchon, G., Pearson, T. J., Perdereau, O., Perotto, L., Perrotta, F., Pettorino, V., Piacentini, F., Piat, M., Pierpaoli, E., Pietrobon, D., Plaszczynski, S., Pointecouteau, E., Polenta, G., Popa, L., Pratt, G. W., Przeau, G., Prunet, S., Puget, J.-L., Rachen, J. P., Reach, W. T., Rebolo, R., Reinecke, M., Remazeilles, M., Renault, C., Renzi, A., Ristorcelli, I., Rocha, G., Rosset, C., Rossetti, M., Roudier, G., Rouill dOrfeuil, B., Rowan-Robinson, M., Rubio-Martn, J. A., Rusholme, B., Said, N., Salvatelli, V., Salvati, L., Sandri, M., Santos, D., Savelainen, M., Savini, G., Scott, D., Seiffert, M. D., Serra, P., Shellard, E. P. S., Spencer, L. D., Spinelli, M., Stolyarov, V., Stompor, R., Sudiwala, R., Sunyaev, R., Sutton, D., Suur-Uski, A.-S., Sygnet, J.-F., Tauber, J. A., Terenzi, L., Toffolatti, L., Tomasi, M., Tristram, M., Trombetti, T., Tucci, M., Tuovinen, J., Trler, M., Umana, G., Valenziano, L., Valiviita, J., Van Tent, F., Vielva, P., Villa, F., Wade, L. A., Wandelt, B. D., Wehus, I. K., White, M., White, S. D. M., Wilkinson, A., Yvon, D., Zacchei, A., and Zonca, A., "Planck 2015 results - xiii. cosmological parameters," *Astronomy and Astrophysics*, vol. 594, p. A13, 2016.

[37] M. Zaldarriaga, "Polarization of the microwave background in reionized models," *Phys. Rev. D*, vol. 55, pp. 1822–1829, Feb 1997.

[38] M. Zaldarriaga and U. c. v. Seljak, "All-sky analysis of polarization in the microwave background," *Phys. Rev. D*, vol. 55, pp. 1830–1840, Feb 1997.

[39] M. Kamionkowski, A. Kosowsky, and A. Stebbins, "Statistics of cosmic microwave background polarization," *Phys. Rev. D*, vol. 55, pp. 7368–7388, Jun 1997.

[40] R. Namba, M. Peloso, M. Shiraishi, L. Sorbo, and C. Unal, "Scale-dependent gravitational waves from a rolling axion," *Journal of Cosmology and Astroparticle Physics*, vol. 2016, no. 01, p. 041, 2016.

[41] S. Saito, K. Ichiki, and A. Taruya, "Probing polarization states of primordial gravitational waves with cosmic microwave background anisotropies," *Journal of Cosmology and Astroparticle Physics*, vol. 2007, no. 09, p. 002, 2007.

[42] A. Kusaka, T. Essinger-Hileman, J. W. Appel, P. Gallardo, K. D. Irwin, N. Jarosik, M. R. Nolta, L. A. Page, L. P. Parker, S. Raghunathan, J. L. Sievers, S. M. Simon, S. T. Staggs, and K. Visnjic, "Modulation of cosmic microwave background polarization with a warm rapidly rotating half-wave plate on the atacama b-mode search instrument," *Review of Scientific Instruments*, vol. 85, no. 2, p. 024501, 2014.

[43] D. S. Swetz, P. A. R. Ade, M. Amiri, J. W. Appel, E. S. Battistelli, B. Burger, J. Chervenak, M. J. Devlin, S. R. Dicker, W. B. Doriese, R. Dnner, T. Essinger-Hileman, R. P. Fisher, J. W. Fowler, M. Halpern, M. Hasselfield, G. C. Hilton, A. D. Hincks, K. D.

Irwin, N. Jarosik, M. Kaul, J. Klein, J. M. Lau, M. Limon, T. A. Marriage, D. Marsden, K. Martocci, P. Mauskopf, H. Moseley, C. B. Netterfield, M. D. Niemack, M. R. Nolta, L. A. Page, L. Parker, S. T. Staggs, O. Stryzak, E. R. Switzer, R. Thornton, C. Tucker, E. Wollack, and Y. Zhao, "Overview of the atacama cosmology telescope: Receiver, instrumentation, and telescope systems," *The Astrophysical Journal Supplement Series*, vol. 194, no. 2, p. 41, 2011.

[44] R. Datta, C. D. Munson, M. D. Niemack, J. J. McMahon, J. Britton, E. J. Wollack, J. Beall, M. J. Devlin, J. Fowler, P. Gallardo, J. Hubmayr, K. Irwin, L. Newburgh, J. P. Nibarger, L. Page, M. A. Quijada, B. L. Schmitt, S. T. Staggs, R. Thornton, and L. Zhang, "Large-aperture wide-bandwidth antireflection-coated silicon lenses for millimeter wavelengths," *Appl. Opt.*, vol. 52, pp. 8747–8758, Dec 2013.

[45] C. Munson, *Technology Development for Cosmic Microwave Background Cosmology.* PhD thesis, University of Michigan, 2016.

[46] J. D. Jackson, *Classical electrodynamics.* New York, NY: Wiley, 3rd ed. ed., 1999.

[47] C. M. Posada, P. A. R. Ade, Z. Ahmed, K. Arnold, J. E. Austermann, A. N. Bender, L. E. Bleem, B. A. Benson, K. Byrum, J. E. Carlstrom, C. L. Chang, H. M. Cho, S. T. Ciocys, J. F. Cliche, T. M. Crawford, A. Cukierman, D. Czaplewski, J. Ding, R. Divan, T. de Haan, M. A. Dobbs, D. Dutcher, W. Everett, A. Gilbert, N. W. Halverson, N. L. Harrington, K. Hattori, J. W. Henning, G. C. Hilton, W. L. Holzapfel, J. Hubmayr, K. D. Irwin, O. Jeong, R. Keisler, D. Kubik, C. L. Kuo, A. T. Lee, E. M. Leitch, S. Lendinez, S. S. Meyer, C. S. Miller, J. Montgomery, M. Myers, A. Nadolski, T. Natoli, H. Nguyen, V. Novosad, S. Padin, Z. Pan, J. Pearson, J. E. Ruhl, B. R. Saliwanchik, G. Smecher, J. T. Sayre, E. Shirokoff, L. Stan, A. A. Stark, J. Sobrin, K. Story, A. Suzuki, K. L. Thompson, C. Tucker, K. Vanderlinde, J. D. Vieira, G. Wang, N. Whitehorn, V. Yefremenko, K. W. Yoon, and K. E. Ziegler, "Fabrication of large dual-polarized multichroic tes bolometer arrays for cmb measurements with the spt-3g camera," *Superconductor Science and Technology*, vol. 28, no. 9, p. 094002, 2015.

[48] A. Cukierman, A. T. Lee, C. Raum, A. Suzuki, and B. Westbrook, "Hierarchical sinuous phased array for increased mapping speed of multichroic focal planes," 2017.

[49] T. Matsumura, S. Hanany, P. Ade, B. R. Johnson, T. J. Jones, P. Jonnalagadda, and G. Savini, "Performance of three- and five-stack achromatic half-wave plates at millimeter wavelengths," *Appl. Opt.*, vol. 48, pp. 3614–3625, Jul 2009.

[50] P. Oxley, P. A. Ade, C. Baccigalupi, P. deBernardis, H.-M. Cho, M. J. Devlin, S. Hanany, B. R. Johnson, T. Jones, A. T. Lee, T. Matsumura, A. D. Miller, M. Milligan, T. Renbarger, H. G. Spieler, R. Stompor, G. S. Tucker, and M. Zaldarriaga, "The ebex experiment," 2004.

[51] T. Matsumura., Y. Akiba, J. Borrill, Y. Chinone, M. Dobbs, H. Fuke, A. Ghribi, A. Hasegawa, K. Hattori, M. Hattori, M. Hazumi, W. Holzapfel, Y. Inoue, K. Ishidoshiro, H. Ishino, H. Ishitsuka, K. Karatsu, N. Katayama, I. Kawano, A. Kibayashi,

Y. Kibe, K. Kimura, N. Kimura, K. Koga, M. Kozu, E. Komatsu, A. Lee, H. Matsuhara, S. Mima, K. Mitsuda, K. Mizukami, H. Morii, T. Morishima, S. Murayama, M. Nagai, R. Nagata, S. Nakamura, M. Naruse, K. Natsume, T. Nishibori, H. Nishino, A. Noda, T. Noguchi, H. Ogawa, S. Oguri, I. Ohta, C. Otani, P. Richards, S. Sakai, N. Sato, S. Y, Y. Sekimoto, A. Shimizu, K. Shinozaki, H. Sugita, T. Suzuki, A. Suzuki, O. Tajima, S. Takada, S. Takakura, Y. Takei, T. Tomaru, T. Uzawa, T. Wada, H. Watanabe, M. Yoshida, N. Yamasaki, T. Yoshida, and K. Yotsumoto, "Mission design of litebird," *Journal of Low Temperature Physics*, vol. 176, pp. 733–740, Sep 2014.

[52] Y. Inoue, P. Ade, Y. Akiba, C. Aleman, K. Arnold, C. Baccigalupi, B. Barch, D. Barron, A. Bender, D. Boettger, J. Borrill, S. Chapman, Y. Chinone, A. Cukierman, T. de Haan, M. A. Dobbs, A. Ducout, R. Dnner, T. Elleflot, J. Errard, G. Fabbian, S. Feeney, C. Feng, G. Fuller, A. J. Gilbert, N. Goeckner-Wald, J. Groh, G. Hall, N. Halverson, T. Hamada, M. Hasegawa, K. Hattori, M. Hazumi, C. Hill, W. L. Holzapfel, Y. Hori, L. Howe, F. Irie, G. Jaehnig, A. Jaffe, O. Jeong, N. Katayama, J. P. Kaufman, K. Kazemzadeh, B. G. Keating, Z. Kermish, R. Keskitalo, T. S. Kisner, A. Kusaka, M. L. Jeune, A. T. Lee, D. Leon, E. V. Linder, L. Lowry, F. Matsuda, T. Matsumura, N. Miller, K. Mizukami, J. Montgomery, M. Navaroli, H. Nishino, H. Paar, J. Peloton, D. Poletti, G. Puglisi, C. R. Raum, G. M. Rebeiz, C. L. Reichardt, P. L. Richards, C. Ross, K. M. Rotermund, Y. Segawa, B. D. Sherwin, I. Shirley, P. Siritanasak, N. Stebor, R. Stompor, J. Suzuki, A. Suzuki, O. Tajima, S. Takada, S. Takatori, G. P. Teply, A. Tikhomirov, T. Tomaru, N. Whitehorn, A. Zahn, and O. Zahn, "Polarbear-2: an instrument for cmb polarization measurements," 2016.

[53] J. Pavlin, N. Vaupoti, and M. epi, "Direction dependence of the extraordinary refraction index in uniaxial nematic liquid crystals," *European Journal of Physics*, vol. 34, no. 2, p. 331, 2013.

[54] S. Naess, M. Hasselfield, J. McMahon, M. D. Niemack, G. E. Addison, P. A. R. Ade, R. Allison, M. Amiri, N. Battaglia, J. A. Beall, F. de Bernardis, J. R. Bond, J. Britton, E. Calabrese, H. mei Cho, K. Coughlin, D. Crichton, S. Das, R. Datta, M. J. Devlin, S. R. Dicker, J. Dunkley, R. Dnner, J. W. Fowler, A. E. Fox, P. Gallardo, E. Grace, M. Gralla, A. Hajian, M. Halpern, S. Henderson, J. C. Hill, G. C. Hilton, M. Hilton, A. D. Hincks, R. Hlozek, P. Ho, J. Hubmayr, K. M. Huffenberger, J. P. Hughes, L. Infante, K. Irwin, R. Jackson, S. M. Kasanda, J. Klein, B. Koopman, A. Kosowsky, D. Li, T. Louis, M. Lungu, M. Madhavacheril, T. A. Marriage, L. Maurin, F. Menanteau, K. Moodley, C. Munson, L. Newburgh, J. Nibarger, M. R. Nolta, L. A. Page, C. Pappas, B. Partridge, F. Rojas, B. L. Schmitt, N. Sehgal, B. D. Sherwin, J. Sievers, S. Simon, D. N. Spergel, S. T. Staggs, E. R. Switzer, R. Thornton, H. Trac, C. Tucker, M. Uehara, A. V. Engelen, J. T. Ward, and E. J. Wollack, "The atacama cosmology telescope: Cmb polarization at 200¡¡9000," *Journal of Cosmology and Astroparticle Physics*, vol. 2014, no. 10, p. 007, 2014.

[55] T. Louis, E. Grace, M. Hasselfield, M. Lungu, L. Maurin, G. E. Addison, P. A. R. Ade, S. Aiola, R. Allison, M. Amiri, E. Angile, N. Battaglia, J. A. Beall, F. de Bernardis, J. R. Bond, J. Britton, E. Calabrese, H. mei Cho, S. K. Choi, K. Coughlin, D. Crichton,

K. Crowley, R. Datta, M. J. Devlin, S. R. Dicker, J. Dunkley, R. Dnner, S. Ferraro, A. E. Fox, P. Gallardo, M. Gralla, M. Halpern, S. Henderson, J. C. Hill, G. C. Hilton, M. Hilton, A. D. Hincks, R. Hlozek, S. P. Ho, Z. Huang, J. Hubmayr, K. M. Huffenberger, J. P. Hughes, L. Infante, K. Irwin, S. M. Kasanda, J. Klein, B. Koopman, A. Kosowsky, D. Li, M. Madhavacheril, T. A. Marriage, J. McMahon, F. Menanteau, K. Moodley, C. Munson, S. Naess, F. Nati, L. Newburgh, J. Nibarger, M. D. Niemack, M. R. Nolta, C. Nuez, L. A. Page, C. Pappas, B. Partridge, F. Rojas, E. Schaan, B. L. Schmitt, N. Sehgal, B. D. Sherwin, J. Sievers, S. Simon, D. N. Spergel, S. T. Staggs, E. R. Switzer, R. Thornton, H. Trac, J. Treu, C. Tucker, A. V. Engelen, J. T. Ward, and E. J. Wollack, "The atacama cosmology telescope: two-season actpol spectra and parameters," *Journal of Cosmology and Astroparticle Physics*, vol. 2017, no. 06, p. 031, 2017.

[56] Planck Collaboration, Aghanim, N., Akrami, Y., Ashdown, M., Aumont, J., Baccigalupi, C., Ballardini, M., Banday, A. J., Barreiro, R. B., Bartolo, N., Basak, S., Benabed, K., Bersanelli, M., Bielewicz, P., Bonaldi, A., Bonavera, L., Bond, J. R., Borrill, J., Bouchet, F. R., Burigana, C., Calabrese, E., Cardoso, J.-F., Challinor, A., Chiang, H. C., Colombo, L. P. L., Combet, C., Crill, B. P., Curto, A., Cuttaia, F., de Bernardis, P., de Rosa, A., de Zotti, G., Delabrouille, J., Di Valentino, E., Dickinson, C., Diego, J. M., Doré, O., Ducout, A., Dupac, X., Dusini, S., Efstathiou, G., Elsner, F., Enßlin, T. A., Eriksen, H. K., Fantaye, Y., Finelli, F., Forastieri, F., Frailis, M., Franceschi, E., Frolov, A., Galeotta, S., Galli, S., Ganga, K., Génova-Santos, R. T., Gerbino, M., González-Nuevo, J., Górski, K. M., Gratton, S., Gruppuso, A., Gudmundsson, J. E., Herranz, D., Hivon, E., Huang, Z., Jaffe, A. H., Jones, W. C., Keihänen, E., Keskitalo, R., Kiiveri, K., Kim, J., Kisner, T. S., Knox, L., Krachmalnicoff, N., Kunz, M., Kurki-Suonio, H., Lagache, G., Lamarre, J.-M., Lasenby, A., Lattanzi, M., Lawrence, C. R., Le Jeune, M., Levrier, F., Lewis, A., Liguori, M., Lilje, P. B., Lilley, M., Lindholm, V., López-Caniego, M., Lubin, P. M., Ma, Y.-Z., Macías-Pérez, J. F., Maggio, G., Maino, D., Mandolesi, N., Mangilli, A., Maris, M., Martin, P. G., Martínez-González, E., Matarrese, S., Mauri, N., McEwen, J. D., Meinhold, P. R., Mennella, A., Migliaccio, M., Millea, M., Miville-Deschênes, M.-A., Molinari, D., Moneti, A., Montier, L., Morgante, G., Moss, A., Narimani, A., Natoli, P., Oxborrow, C. A., Pagano, L., Paoletti, D., Partridge, B., Patanchon, G., Patrizii, L., Pettorino, V., Piacentini, F., Polastri, L., Polenta, G., Puget, J.-L., Rachen, J. P., Racine, B., Reinecke, M., Remazeilles, M., Renzi, A., Rocha, G., Rossetti, M., Roudier, G., Rubiño-Martín, J. A., Ruiz-Granados, B., Salvati, L., Sandri, M., Savelainen, M., Scott, D., Sirignano, C., Sirri, G., Stanco, L., Suur-Uski, A.-S., Tauber, J. A., Tavagnacco, D., Tenti, M., Toffolatti, L., Tomasi, M., Tristram, M., Trombetti, T., Valiviita, J., Van Tent, F., Vielva, P., Villa, F., Vittorio, N., Wandelt, B. D., Wehus, I. K., White, M., Zacchei, A., and Zonca, A., "Planck intermediate results - li. features in the cosmic microwave background temperature power spectrum and shifts in cosmological parameters," *A&A*, vol. 607, p. A95, 2017.

[57] D. Hanson, S. Hoover, A. Crites, P. A. R. Ade, K. A. Aird, J. E. Austermann, J. A. Beall, A. N. Bender, B. A. Benson, L. E. Bleem, J. J. Bock, J. E. Carlstrom, C. L. Chang, H. C. Chiang, H.-M. Cho, A. Conley, T. M. Crawford, T. de Haan, M. A. Dobbs,

W. Everett, J. Gallicchio, J. Gao, E. M. George, N. W. Halverson, N. Harrington, J. W. Henning, G. C. Hilton, G. P. Holder, W. L. Holzapfel, J. D. Hrubes, N. Huang, J. Hubmayr, K. D. Irwin, R. Keisler, L. Knox, A. T. Lee, E. Leitch, D. Li, C. Liang, D. Luong-Van, G. Marsden, J. J. McMahon, J. Mehl, S. S. Meyer, L. Mocanu, T. E. Montroy, T. Natoli, J. P. Nibarger, V. Novosad, S. Padin, C. Pryke, C. L. Reichardt, J. E. Ruhl, B. R. Saliwanchik, J. T. Sayre, K. K. Schaffer, B. Schulz, G. Smecher, A. A. Stark, K. T. Story, C. Tucker, K. Vanderlinde, J. D. Vieira, M. P. Viero, G. Wang, V. Yefremenko, O. Zahn, and M. Zemcov, "Detection of b-mode polarization in the cosmic microwave background with data from the south pole telescope," *Phys. Rev. Lett.*, vol. 111, p. 141301, Sep 2013.

[58] M. Madhavacheril, N. Sehgal, R. Allison, N. Battaglia, J. R. Bond, E. Calabrese, J. Caligiuri, K. Coughlin, D. Crichton, R. Datta, M. J. Devlin, J. Dunkley, R. Dünner, K. Fogarty, E. Grace, A. Hajian, M. Hasselfield, J. C. Hill, M. Hilton, A. D. Hincks, R. Hlozek, J. P. Hughes, A. Kosowsky, T. Louis, M. Lungu, J. McMahon, K. Moodley, C. Munson, S. Naess, F. Nati, L. Newburgh, M. D. Niemack, L. A. Page, B. Partridge, B. Schmitt, B. D. Sherwin, J. Sievers, D. N. Spergel, S. T. Staggs, R. Thornton, A. Van Engelen, J. T. Ward, and E. J. Wollack, "Evidence of lensing of the cosmic microwave background by dark matter halos," *Phys. Rev. Lett.*, vol. 114, p. 151302, Apr 2015.

[59] C. Sifn, N. Battaglia, M. Hasselfield, F. Menanteau, L. F. Barrientos, J. R. Bond, D. Crichton, M. J. Devlin, R. Dnner, M. Hilton, A. D. Hincks, R. Hlozek, K. M. Huffenberger, J. P. Hughes, L. Infante, A. Kosowsky, D. Marsden, T. A. Marriage, K. Moodley, M. D. Niemack, L. A. Page, D. N. Spergel, S. T. Staggs, H. Trac, and E. J. Wollack, "The atacama cosmology telescope: dynamical masses for 44 sz-selected galaxy clusters over 755 square degrees," *Monthly Notices of the Royal Astronomical Society*, vol. 461, no. 1, pp. 248–270, 2016.